

HIGH ENERGY, ULTRAVIOLET PULSE
GENERATION IN HOLLOW WAVEGUIDES

**ARTHUR LAKES LIBRARY
COLORADO SCHOOL OF MINES
GOLDEN, CO 80401**

by

Jeffrey Wojtkiewicz

ProQuest Number: 10797078

All rights reserved

INFORMATION TO ALL USERS

The quality of this reproduction is dependent upon the quality of the copy submitted.

In the unlikely event that the author did not send a complete manuscript and there are missing pages, these will be noted. Also, if material had to be removed, a note will indicate the deletion.



ProQuest 10797078

Published by ProQuest LLC (2019). Copyright of the Dissertation is held by the Author.

All rights reserved.

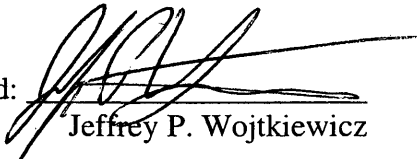
This work is protected against unauthorized copying under Title 17, United States Code
Microform Edition © ProQuest LLC.

ProQuest LLC.
789 East Eisenhower Parkway
P.O. Box 1346
Ann Arbor, MI 48106 – 1346

A thesis submitted to the Faculty and Board of Trustees of the Colorado School of Mines in partial fulfillment of the requirements for the degree of Doctor of Philosophy (Applied Physics).

Golden, Colorado

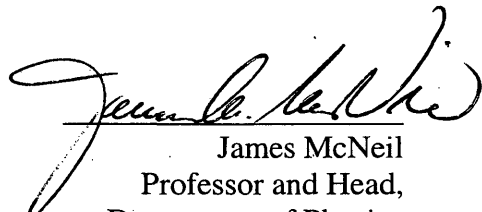
Date 1/21/05

Signed: 
Jeffrey P. Wojtkiewicz

Approved: 
Charles G. Durfee, III

Golden, Colorado

Date 1/25/05


James McNeil
Professor and Head,
Department of Physics

ABSTRACT

High power, ultrafast Ti:sapphire based laser systems in the near infrared are now well established technologies. However, for some applications it is desirable to have a shorter wavelength source. Recent work has demonstrated intense ultraviolet generation by the use of frequency mixing in gas-filled hollow capillaries. In this process, fundamental 800-nm light is mixed with its second harmonic, 400-nm light to generate ultraviolet light at 266 nm. In previous experiments the energy available required short pulses to be at the proper intensity to initiate the process. This thesis presents a new method for using chirped pulses to generate the ultraviolet light. The method is similar to chirped pulse amplification, which is widely used in ultrashort laser systems. This method uses longer duration pulses to maintain the proper intensity for the mixing process with even higher pulse energies. The process has been shown to generate 62 μJ ultraviolet pulses at near transform-limited 82 fs duration. The process can be also be used with other input wavelengths to generate light at even shorter wavelengths.

This thesis also presents a new multipass amplifier design is also developed to create the highest energy pulses generated in a single stage Ti:sapphire based amplifier. The amplifier uses a focused beam in the first set of passes, then the

beam is extracted from the cavity. A saturable absorber is used to improve the intensity contrast. Then the beam is reinjected into the same amplifier with a collimated beam to efficiently extract the stored pump energy. The amplifier has an intensity contrast of 10^9 on a nanosecond timescale with a total energy per pulse of more than 10 mJ.

To explore some of the applications of a high-energy ultraviolet source, an x-ray cell is constructed with special consideration for maintaining a stable target. This is important for moderate energy pulses, which must use short focal length optics to reach the required intensity for x-ray generation. Frequency doubled infrared light from the amplifier system was used to generate x-rays from a copper wire target to estimate the energy requirements for generating x-rays with ultraviolet pulses. While the ultraviolet energy from the mixing process was not enough to generate x-rays, the cell will be useful to others needing a stable target to generate x-rays with the smallest possible source size.

TABLE OF CONTENTS

ABSTRACT	iii
TABLE OF CONTENTS	v
LIST OF FIGURES.....	x
LIST OF TABLES	xiii
ACKNOWLEDGEMENTS	xiv
CHAPTER 1 INTRODUCTION	1
1.1 High Power Ultrafast Lasers	1
1.2 Ultrashort Energetic Ultraviolet Generation	3
1.3 Towards X-Ray Generation With Ultraviolet Pulses	5
1.4 Objectives.....	7
1.4.1 Develop a Compact UV-OPCPA System	7
1.4.2 Develop a Single-Stage, High-Energy, Ultrashort Pulse System....	8
1.4.3 Towards X-Ray Generation With Ultraviolet Light	9
CHAPTER 2 HIGH-POWER ULTRAFAST LASER REVIEW	11
2.1 Introduction	11
2.2 Chirped Pulse Amplification Review.....	11
2.3 Sources of Dispersion.....	13

2.3.1 Material Dispersion	15
2.3.2 Grating Pairs.....	16
2.3.3 Prism Pairs.....	17
2.4 Initial High Power Ultrafast Laser System	18
2.4.1 Ultrashort Pulse Laser Oscillator	19
2.4.2 Multipass Amplifier	20
2.5 Summary	24
CHAPTER 3 HIGH-ENERGY, DOUBLE-CONFOCAL MULTIPASS AMPLIFIER.....	25
3.1 Introduction	25
3.2 High Energy Multipass Design	26
3.3 Aberration Corrections.....	29
3.4 Amplifier Intensity Contrast.....	33
3.5 Amplifier Performance and Characterization	35
3.5.1 Energy Extraction.....	36
3.5.2 Intensity Contrast	37
3.5.3 Pulse Duration	38
3.5.4 Beam Quality.....	40
3.6 Applications to Other Systems.....	41
3.7 Summary	43

CHAPTER 4 ULTRAVIOLET OPTICAL PARAMETRIC CHIRPED PULSE AMPLIFICATION.....	45
4.1 Introduction.....	45
4.2 Other Methods of Ultrafast Ultraviolet Generation	46
4.3 Phase Matching in Hollow Core Waveguides	47
4.4 Optical Parametric Amplification Process	48
4.5 Propagation Phase for Gas Filled Waveguides	50
4.6 Phase Matched Ultraviolet Pulse Generation.....	54
4.7 Optical Parametric Chirped Pulse Amplification.....	56
4.8 Simulations.....	57
4.8.1 High Energy Chirped Pulse.....	58
4.8.2 Optimum Seed Duration.....	60
4.8.3 Ultraviolet Pulse Compression.....	62
4.9 Summary	65
CHAPTER 5 INITIAL UV-OPCPA EXPERIMENTS	67
5.1 Introduction.....	67
5.2 Producing Pump Light	68
5.3 Preliminary UV-OPCPA Results	70
5.4 Scalable UV-OPCA Experiment.....	75
5.5 Summary	79

CHAPTER 6 HIGH-POWER ULTRAVIOLET OP-CPA	81
6.1 Introduction	81
6.2 System Layout.....	83
6.3 High Energy Ultraviolet Generation	87
6.4 Ultraviolet Beam Quality	92
6.4.1 Lowest Order Mode	93
6.4.2 Second Order Mode	94
6.5 Spectral and Temporal Characteristics.....	97
6.6 Improving Spectral Width.....	99
6.7 Summary	101
 CHAPTER 7 ULTRAVIOLET X-RAY GENERATION	 103
7.1 Introduction.....	103
7.2 X-Ray Cell Design Considerations	106
7.2.1 Focusing Considerations	107
7.2.2 Debris Control	109
7.2.3 Alignment Issues	111
7.2.4 Target Stability.....	112
7.3 Results	114
7.4 Summary	117

CHAPTER 8 SUMMARY AND CONCLUSIONS	119
8.1 High Energy, Double Confocal Multipass Amplifier	119
8.2 Ultraviolet Parametric Mixing in Hollow Fibers	120
8.2.1 Low Energy Ultraviolet Generation.....	120
8.2.2 High Energy Ultraviolet Generation	121
8.3 X-ray Cell Construction	122
8.4 Directions for Future Exploration	123
8.4.1 Double Confocal, Multipass Amplifier.....	123
8.4.2 Hollow Fiber, Chirped Pulse Optical Parametric Mixing.....	125
8.4.3 Towards X-Ray Generation with Ultraviolet Light	126
APPENDIX A LASER SYSTEM ALIGNMENT	127
REFERENCES.....	131

LIST OF FIGURES

Figure 2.1	Block diagram of typical CPA system.....	12
Figure 2.2	a) Grating compressor. b) All-reflective grating stretcher.....	17
Figure 2.3	a) Prism pair for dispersion control. b) Group delay curve for prism pair.....	18
Figure 2.4	Kerr-lens modelocked laser.....	19
Figure 2.5	Basic three-mirror multipass amplifier design.....	21
Figure 3.1	Double-confocal, multipass amplifier design.....	28
Figure 3.2	Complete double-confocal amplifier layout with correction optics...	30
Figure 3.3	Evolution of the beam diameter (a) and the beam divergence (b) in the amplifier.....	32
Figure 3.4	a) Lineout of an image of the fluorescence from the crystal. b) Diode traces of the output ASE background.....	37
Figure 3.5	a) Retrieved FROG trace. b) Unamplified spectrum (dashed) and...	39
Figure 3.6	Beam radius as a function of distance from the focus.....	41
Figure 3.7	a) Image of amplified, uncompressed beam. b) Lineout from center of the image with best Gaussian fit. c) Lineout of best focus with Gaussian fit.....	41

Figure 4.1	a) Schematic of different waves in OPA process. b) Photon view of the OPA process.....	49
Figure 4.2	First three (EH_{11} , EH_{12} , EH_{13}) hollow-core waveguide modes.....	51
Figure 4.3	Transmission efficiencies through a 150- μm capillary for the first three guided modes for 266 (top), 400, (mid) and 800 nm (bottom). ..	52
Figure 4.4	Normalized ultraviolet output versus capillary length and gas pressure.	59
Figure 4.5	Energy transfer from pump (thin) to seed (dashed) and ultraviolet (dashed).....	59
Figure 4.6	Temporal profile of output pulses from capillary.	60
Figure 4.7	Depleted pump profiles for different seed durations.	61
Figure 4.8	a) Comparison of output UV spectrum with different IR seed durations. b) Optimal input pump (solid) and seed (dashed) pulse durations for wide ultraviolet bandwidth.	62
Figure 4.9	Generated ultraviolet pulse compressed with prism pair (thick dashed) compared to Fourier transform limit (thin).....	64
Figure 5.1	a) Dispersion-free self-diffraction FROG. b) Reconstructed blue pulse.	69
Figure 5.2	Initial OP-CPA setup.	71
Figure 5.3	UV output versus IR pulse duration.....	73

Figure 5.4	Setup for scalable blue production.....	76
Figure 5.5	Experimental setup for final OP-CPA experiment.	79
Figure 6.1	Simulated ultraviolet output versus pump energy for three different pump durations.....	82
Figure 6.2	High energy OP-CPA mixing setup.....	84
Figure 6.3	Plot of energies versus pressure.	85
Figure 6.4	Output ultraviolet energy for different pump input energies.	89
Figure 6.5	Coupling efficiency for different pump durations.	90
Figure 6.6	Ultraviolet and blue measured versus pressure at the exit of the cell.	92
Figure 6.7	Lowest ultraviolet propagation mode and lineout with best fit.	94
Figure 6.8	Relative group delay for pulses in the mixing process.	95
Figure 6.9	First and second order radial capillary modes.	96
Figure 6.10	Higher capillary mode image and lineout with best fit.....	97
Figure 6.11	Spectra of seed (a), pump (b), and produced ultraviolet (c) with simulated spectra (dashed).	98
Figure 6.12	a) Simulated output seed (dashed), pump (thin) and signal (thick) pulses. b) Retrieved PG-FROG trace for shortest output pulse. c) Compressed ultraviolet output (dashed) and simulated transform- limited pulse (solid).	98

Figure 6.13 a) Mixing with same (positively) chirped pulses. b) Mixing with oppositely chirped pulses.	101
Figure 7.1 X-ray cell schematic.....	107
Figure 7.2 Focus quality for a plano-convex lens and a spherical mirror at different angles of incidence.	108
Figure 7.3 X-ray wire target guide design.....	113
Figure 7.4 Initial x-ray spectra generated with blue light.	115

LIST OF TABLES

Table 2.1 Sign of different orders of dispersion for some common optical elements.	15
---	----

ACKNOWLEDGEMENTS

I would like to thank many people whose support and contributions made this work possible and enjoyable.

First and foremost, I would also like to thank my advisor, Chip Durfee, for his endless support throughout this research. Without his guidance and direction this thesis would never have materialized as a cohesive unit. I would also like to thank all of the other students who have worked in the laser lab over the course of this research, especially Michael Gaffield and Aaron Oakley.

There were monetary and equipment contributions without which this work could not have been completed. The bulk of the research was supported by a grant from the National Science Foundation and also a Colorado School of Mines startup grant. The Ti:sapphire oscillator was donated by KM Labs. Much of the equipment for the x-ray cell was provided by Jeff Squier.

It is impossible to list all of the support my wife Shelley provided, but I will always be thankful for it. I am very grateful to my parents, who have been tremendously supportive throughout my entire education. I would also like to thank Jon Barnes and Yuki Yoshida for their friendship during this time, and of course Roxy and Echo, my little four-legged stress relievers.

CHAPTER 1 INTRODUCTION

1.1 High Power Ultrafast Lasers

The development of chirped pulse amplification (CPA) [1] has enabled efficient generation of femtosecond, laser pulses in solid-state materials such as TiAl_2O_3 [2]. The past decade has seen numerous developments in compact ultrafast laser systems with peak powers in the terawatt and even petawatt range [3]. These intensities are achieved with single or multiple-stages of amplification producing gains of up to 10^7 . The size of a laser system typically dictates the energy level of the pulse; higher intensities with modest sized laser systems are typically achieved by shortening the ultimate duration of the amplified pulse. Typical systems routinely produce amplified pulse durations of <30 fs duration. Focusing these pulses results in peak intensities on the order of 10^{20} W/cm²—an intensity greater than the entire solar flux incident on the Earth focused onto a pinhead [3].

There are essentially two fields in which ultrashort pulse lasers excel: monitoring chemical or physical processes on extremely short timescales (~ 30 fs) via pump probe experiments and achieving ultrahigh intensities (10^{16} - 10^{20} W/cm²) in small volumes due to the ultrashort pulse durations. Ultrashort pulses at moderate to low energy are able to

take “snapshots” of physical processes such as charge-carrier dynamics in semiconductors, and the formation and breaking of chemical bonds [4-8].

Some high intensity applications of ultrafast lasers include micromachining [9], studying laser-plasma interactions [10], x-ray generation [11, 12], and at intensities reaching relativistic levels, wakefield plasma-waves and electron beam generation. For pulse energies greater than 1-2 mJ per pulse, multistage amplifiers are used [13]. This requires multiple Ti:sapphire crystals, optics and pump lasers. Synchronizing multiple pump lasers requires expensive timing electronics, and typically the complete energy of the first pump laser is not fully utilized. This lowers the overall efficiency and raises the overall cost of the system. A single stage amplifier would greatly simplify the construction of such laser systems; a portion of this thesis will describe the construction of a single-stage high-energy, multipass amplifier. Another field of interest is the development of ultrashort pulse systems at shorter wavelengths by the frequency upconversion of the infrared light produced by the now well established Ti:sapphire systems. This frequency conversion can be direct harmonic conversion in crystals or other media, or three or four wave mixing processes in gases or other nonlinear media [14-16].

1.2 Ultrashort Energetic Ultraviolet Generation

The development of ultrashort pulse light sources in the ultraviolet region of the spectrum has important implications for time-domain studies in atomic/molecular physics [17], physical chemistry [18-21], solid state physics [22], and processes of biological interest [23, 24]. Ultraviolet light is typically used in chemistry applications because many molecules have absorption bands at these wavelengths and can be studied through pump probe experiments.

Much of the ultrashort pulse source development effort in the ultraviolet region of the spectrum relies on frequency upconversion of ultrashort pulses at longer wavelengths in the visible or near infrared, where generation and amplification techniques are now well established. Efficient direct frequency conversion of these pulses into the ultraviolet by the use of nonlinear crystals is generally difficult because of severe group-velocity walk-off and phase-matching bandwidth limitations, especially when pulses <130 fs are desired [16]. Optical parametric amplification in nonlinear crystals has been used to amplify pulses down to 300-400 nm [25, 26]. However, it is difficult to efficiently scale this method much below 300 nm because of two photon absorption in the doubling crystals [14].

Ultraviolet free-electron lasers in this wavelength range have been demonstrated [27], but a system based on a ultrashort Ti:sapphire is much more compact and can fit on a single optical table. Also, the duration of the generated ultraviolet pulses is on the same

scale or shorter than the input seed pulse (~ 30 fs). These excimer lasers typically produce pulses with picosecond pulse durations.

Recent work has demonstrated phase-matched harmonic and parametric ultraviolet generation in gas-filled, hollow waveguides, through the $3\omega = 2 \times (2\omega) - \omega$ process [28, 29]. Most low-pressure gases are transparent well into the vacuum ultraviolet region of the spectrum, and shorter wavelengths in the extreme ultraviolet range can propagate with moderate losses through low-pressure gases. Because the index of refraction of gases is much lower than that of solid media, the problems with group velocity walkoff are greatly reduced, making it possible to generate pulses in the 10 fs range. Mixing through a parametric process allows a tunable output in the ultraviolet, with the ultraviolet light generated in the lowest order mode of the capillary. This results in a very high spatial quality of the output ultraviolet beam. However, the energies presented so far have been modest ($< 10 \mu\text{J}$). The input pulse durations in these experiments were not carefully controlled. The previous experiments did not report the input pulse durations, and it is possible that even in these initial experiments slightly chirped pulses were used. The work presented in this thesis explores using chirped pulses in the parametric mixing process to maintain the proper intensity in the capillary while making use of all the energy available from the laser system.

Higher energy ultraviolet pulses would make possible studying some of the same processes studied with moderate energy infrared, ultrashort pulses, such as micromachining, higher harmonic generation, ionization, and even laser x-ray generation.

By studying these processes with shorter wavelengths, the ultimate feature or source size would be smaller. While micromachining does not necessarily require more than a few microjoules of energy, a high-energy ultraviolet source could be used to machine multiple sites at once. The hollow-fiber mixing process used here is very inexpensive, easily constructed, and would allow easy integration into existing Ti:sapphire based laser systems.

1.3 Towards X-Ray Generation With Ultraviolet Pulses

A high-temperature plasma is created when a very intense ($\sim 10^{17}$ W/cm²) laser pulse is focused onto the surface of a solid. These laser-produced plasmas are good radiators of both visible and x-ray photons due to line transitions, radiative recombination, and bremsstrahlung radiation. The main motivation for studying the interactions of intense, short laser pulses with solid targets has been the possibility of studying high density and temperature laboratory plasmas, and their application as a source of intense, ultrashort x-ray pulses [30]. These laboratory plasmas offer numerous advantages to conventional x-ray sources (e.g. synchotrons) such as: small size, easier access, lower cost, higher intensity contrast, shorter pulse duration, and a smaller source size. Much of the study of laser-plasma interactions has been done with ultrashort pulses in the near infrared. Here the goal is to move towards using the energetic short pulse ultraviolet light generated by the parametric process to study x-ray generation at shorter wavelengths.

Perhaps the most compelling reason to study the generation of x-rays by using ultraviolet light is that shorter wavelength light focuses to a smaller spot than longer wavelengths. This will result in a smaller source size for the generated x-rays, which will correspond to greater resolution when using the x-rays for imaging applications. This, coupled with new developments in microscopic liquid droplet targets [10], would lead to very small source size x-ray sources. Another benefit is that because the ultraviolet light is generated by a third order parametric process, the contrast between the main pulse and any prepulses is increased by the third power (e.g. from 10^7 to 10^{21}). Recently, more importance has been placed on high temporal contrast in the pulse used for x-ray generation. Although the x-ray yield can be increased with a prepulse on the target, it has been shown that the generated x-rays will be produced on a picosecond time scale. With an intensity contrast ratio of 10^8 or more, the x-rays are generated on the same time scale as the laser pulse [12, 31]. These “purer” pulses will also be beneficial in studying the underlying process of laser solid absorption in the ultraviolet. The recently proposed fast-igniter (FI) scheme for inertial confinement fusion (ICF), has introduced another reason to study the absorption of a short pulse laser in high-density plasmas. This is still a new idea in this area, and there is a demand for a large number of ultraviolet absorption experiments with carefully controlled parameters [32], which the UV-OPCPA technique would make available.

1.4 Objectives

The overall goal of this thesis is to study the effect of using chirped pulses in the hollow fiber parametric mixing process to scale the output ultraviolet to the hundred microjoule level. A high energy amplifier is needed to demonstrate the benefit of lengthening the pulse durations in the process. The following sections outline the main points presented in this thesis.

1.4.1 Develop a Compact UV-OPCPA System

The main objective of this thesis is to develop a tabletop energetic ultrashort pulse system in the ultraviolet region of the spectrum. The method used extends on the method of generating tuneable ultraviolet pulses through the use of optical parametric amplification in gas filled capillary waveguides [15, 28, 29]. A method similar to chirped pulse amplification was used to increase the duration of the pulses while maintaining the optimal intensity for the nonlinear process and using higher energies to increase the ultraviolet energy output. This method required recompression of generated ultraviolet pulses to achieve the shortest pulse durations. This method is scaleable to higher pulse energies by using a longer stretch factor on the input pulses. Tuneable ultraviolet wavelengths can be produced in the same way as in the previous work [28].

1.4.2 Develop a Single-Stage, High-Energy, Ultrashort Pulse System

Producing an energetic short pulse ultraviolet laser system from a Ti:sapphire based ultrashort chirped pulse amplification system requires high pulse energies in the infrared. For example, in the three wave mixing process studied here, two blue photons at 400 nm and a single 800 nm photon are used in the process to produce ultraviolet light at 266 nm, and all the light is produced from the fundamental infrared light generated from the chirped pulse amplification system. In contrast to longer pulses that can be frequency-doubled with efficiencies of 80% or more, femtosecond pulses are typically doubled with efficiencies of at best in the 35-45% range. These losses are compounded by the 15-25% conversion efficiencies from the 400 nm pump light into the ultraviolet wavelengths.

For the setup presented in this thesis to be attractive to others needing an energetic short pulse ultraviolet source, the system should be as compact and economical as possible. Currently available Ti:sapphire based laser systems with a single stage of amplification are limited to only 2-4 mJ of energy per pulse. To increase the per pulse energy output of a system, currently the only option is to add a second stage of amplification to the system. This requires a second pump laser, crystal, optics, and space on the optical table.

The main limitation of any amplifier system is the stored energy density of the gain medium. For Ti:sapphire this value is 1 J/cm². Only by increasing the beam size in the gain medium can the output energy be increased. Nearly all amplifiers currently used

in ultrafast chirped pulse amplification systems direct a focused beam to the crystal. The small size of the focus limits the energy output of the amplifier. Current designs are not easily converted to allow the use of a collimated beam in the crystal. This thesis will present a new single-stage, multipass amplifier design, which allows the use of either a focused or collimated beam to the crystal.

1.4.3 Towards X-Ray Generation With Ultraviolet Light

A final objective of this work is to move towards x-ray generation with ultrashort, ultraviolet pulses generated with a tabletop ultraviolet source. Excimer lasers have been used to study the x-ray generation process at these ultraviolet wavelengths, but the pulse durations achievable with the ultraviolet OP-CPA process will be shorter than those produced by the excimer ultraviolet lasers currently in use. This will be the first time x-ray generation can be considered with a tabletop ultraviolet, ultrashort pulse source. Special care will be taken to create a stable target, thus maintaining the advantages from using ultraviolet light. Because each pulse must interact with fresh target material, the metal target has to be cycled in some way. Since moderate energy beams must be focused with very short focal length optics to create the intensities needed for x-ray generation ($>10^{16}$ W/cm²), the Rayleigh range in the focus is very short (<10 μ m). The target must be stable on the order of that distance. A design for an x-ray cell will be presented and characterized with special considerations for its application to moderate energy

ultraviolet pulses. While as of yet the ultraviolet energy is not high enough to produce x-rays, the x-ray cell was used to generate x-rays with blue light from the frequency double fundamental Ti:sapphire light. This allowed for characterization of factors such as the target stability and the minimum energy requirements for x-ray generation.

CHAPTER 2 HIGH-POWER ULTRAFAST LASER

REVIEW

2.1 Introduction

This chapter provides an introduction to concepts that are important in understanding chirped pulse amplification and its application to multipass amplifier design. The same dispersion considerations that are needed to stretch and recompress pulses in conventional amplifiers are also important in the hollow fiber, chirped pulse mixing that is presented later in this thesis. This chapter also describes the initial laser system used to demonstrate the benefits of using chirped pulses at moderate energies in the hollow fiber mixing process. Current trends in Ti:sapphire amplifier design are also explored to illustrate the motivation for implementing the amplifier design presented in the next chapter.

2.2 Chirped Pulse Amplification Review

Nearly all millijoule level ultrafast lasers use chirped pulse amplification (CPA) [33], a technique originally developed for use in microwave radar, to achieve high energies in short pulses. The basic concept is to reversibly disperse (chirp) a pulse in time to avoid

destructive peak powers during amplification. The first application of CPA to short pulse lasers was presented in reference [1]. Chirped pulse amplification is a necessity for Ti:sapphire based amplifiers, which have a relatively large stored energy density of 1 J/cm^2 . With a longer pulse in time the pulse can extract more of the stored energy at a lower intensity, preventing damage to the crystal and optics. Figure 2.1 illustrates a block diagram of a typical Ti:sapphire CPA system.

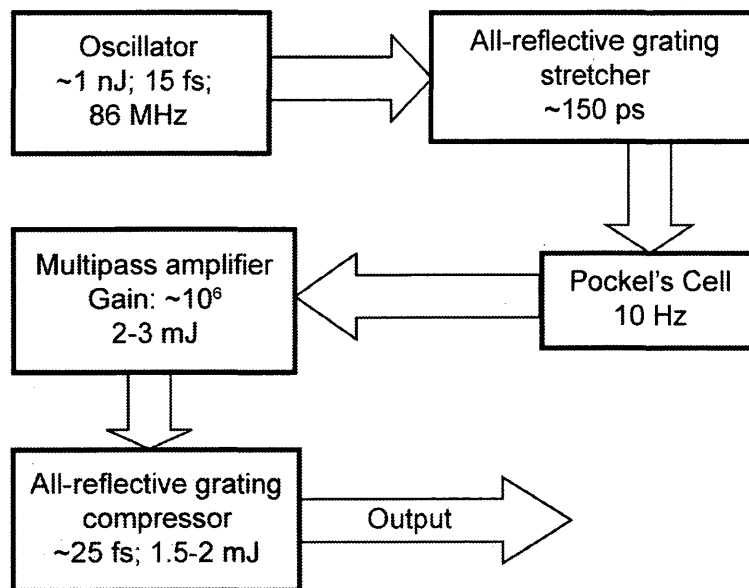


Figure 2.1 Block diagram of typical CPA system.

The system starts with an oscillator that generates low energy ($\sim 1 \text{ nJ}$), wide bandwidth ($\sim 90 \text{ nm}$) pulses at a high repetition rate ($\sim 86 \text{ MHz}$). With proper correction these pulses can achieve durations of less than 10 fs . The pulses are then stretched in time

using a diffraction grating arrangement to ~ 150 ps or more. A single pulse is then selected with a Pockels cell and then amplified to the millijoule level with either a multipass or regenerative amplifier. More than one stage of amplification can be used to achieve higher pulse energies. Following the amplifier, the pulse is recompressed with a second grating pair, set to compensate for the stretcher dispersion and any other optical material in the system.

2.3 Sources of Dispersion

The effects of optical elements on pulse duration are best understood in the spectral domain. The speed of light in all materials is wavelength-dependent; each spectral component of the pulse has a different transit time through each optical element. After propagation through an element, the spectral components of a pulse will be spread over a time range depending on the dispersion of the material; thus the pulse is longer than before. However, all the wavelengths are still present; by reversing the dispersive effect of the element, the pulse can be recompressed.

The effects of optical elements on pulse duration can be calculated by taking the Fourier transform of a pulse in the time domain, adding in the phase effects of the optical elements, and then taking the inverse Fourier transform to revert back to the time domain. Nearly all optical elements of interest have well-behaved Taylor expansions around the

central wavelength of the laser, in the sense that each successive term is much less than the preceding term. This allows us to write the phase, ϕ , of an optical element as

$$\begin{aligned} \phi(\omega) = \phi(\omega_0) + \left. \frac{\partial \phi}{\partial \omega} \right|_{\omega_0} (\omega - \omega_0) + \frac{1}{2!} \left. \frac{\partial^2 \phi}{\partial \omega^2} \right|_{\omega_0} (\omega - \omega_0)^2 \\ + \frac{1}{3!} \left. \frac{\partial^3 \phi}{\partial \omega^3} \right|_{\omega_0} (\omega - \omega_0)^3 + O(\omega^4) \end{aligned} \quad (2.1)$$

where ω is the frequency and ω_0 is the center frequency of the expansion. In this expression the first term is a constant and the second term is the transit time of the center wavelength through the element, so both terms can be neglected. The remaining terms characterize the phase distortions on the pulse. The second order term is called the group velocity dispersion (or the group delay) and represents the relative arrival time of the different wavelengths in the pulse. The higher order terms in the Taylor expansion, third and fourth order dispersion (TOD and FOD) are often much less than the group delay term, but they must be considered to achieve the shortest pulses. Using this Taylor expansion method, the total dispersion for an optical system can be more easily estimated.

The effects of a few common optical elements will be considered in the following sections. A more thorough review of the role of dispersion in ultrashort pulse systems can be found in the references [3, 34, 35]. For reference, Table 2.1 gives the sign of the various orders of dispersion for some common optical elements in ultrafast laser systems.

Table 2.1 Sign of different orders of dispersion for some common optical elements.

Optical Material	GVD $d^2\phi / d\omega^2$ (fs ²)	TOD $d^3\phi / d\omega^3$ (fs ³)	FOD $d^4\phi / d\omega^4$ (fs ⁴)
Glass (fused silica, BK7, etc.)	+	+	-
Prism pair (negative dispersion)	-	-	-
Prism pair (positive dispersion)	+	-	-
Grating stretcher	+	-	+
Grating compressor	-	+	-

2.3.1 Material Dispersion

Nearly all materials are normally dispersive around 800 nm, so the dispersion is straightforward to calculate. The expression for the phase due to propagation through material is given by

$$\phi_m = \frac{l\omega}{c} n(\omega) \quad (2.2)$$

where l is the length of material, c is the speed of light in vacuum, ω is the frequency, and $n(\omega)$ is the index of refraction versus frequency for the material. Empirical formulas for $n(\omega)$ are given by the Sellmeier equations and are tabulated in common optical

references [36]. By taking derivatives of Equation (2.2), the different orders of dispersion can be calculated.

2.3.2 Grating Pairs

The grating stretcher and compressor are used to achieve large, reversible dispersions or pulse stretch factors in small spaces. This is important for chirped pulse amplification where the pulse from the oscillator is temporally stretched by a factor of 10^4 or more. It is more instructive to look at the compressor first to illustrate the mechanism of geometrical dispersion. Figure 2.2a illustrates a typical layout for a double pass grating arrangement used to provide negative dispersion. The gratings, (G_1 and G_2), are parallel, and it is clear from the illustration that the wavelengths travel different distances. The retro-reflector, labeled RR, vertically offsets the beam and sends it directly back. This double pass design is an extension of the single pass, four grating, design first proposed by Martinez [37].

Martinez also discovered that by inserting a telescope in the compressor, the grating pair operates in the positive dispersion regime [33]. To reduce aberrations and the expense of large aperture lenses, they can be replaced by two spherical mirrors. This results in an all-reflective arrangement [38]. Figure 2.2b illustrates the all-reflective stretcher arrangement using only one grating positioned at near Littrow angle and one spherical mirror [39]. This setup has the advantage of only using one grating, which

ensures the gratings are effectively parallel; this helps to eliminate spatial chirp and other aberrations in the stretcher.

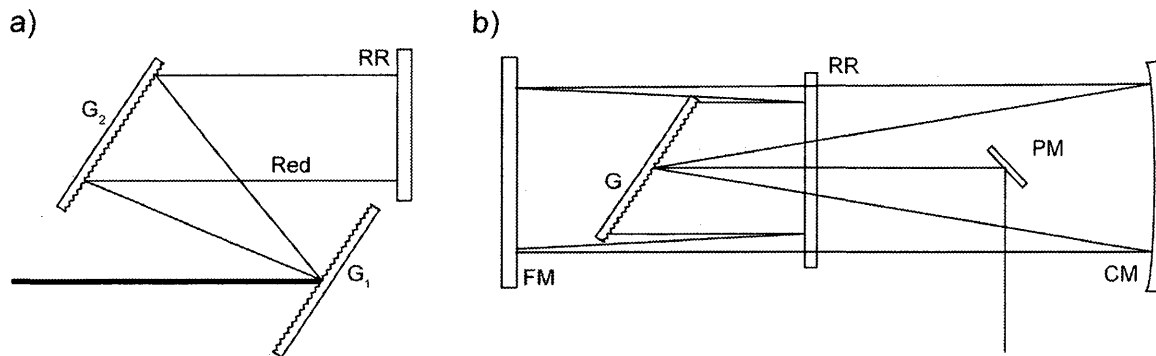


Figure 2.2 a) Grating compressor. b) All-reflective grating stretcher.

Fig.

2.3.3 Prism Pairs

Fork et al developed a prism arrangement that can be operated in both the negative and positive dispersion regime [40]. The basic design is illustrated in Figure 2.3a. The setup consists of a pair of prisms and a mirror, HR, to reflect the beam directly back on itself. The dispersion is controlled by the prism separation and the prism insertion. An advantage to the prism pair is that the dispersion has a smooth transition from negative to positive dispersion, and it can be easily adjusted to provide either negative or positive dispersion.

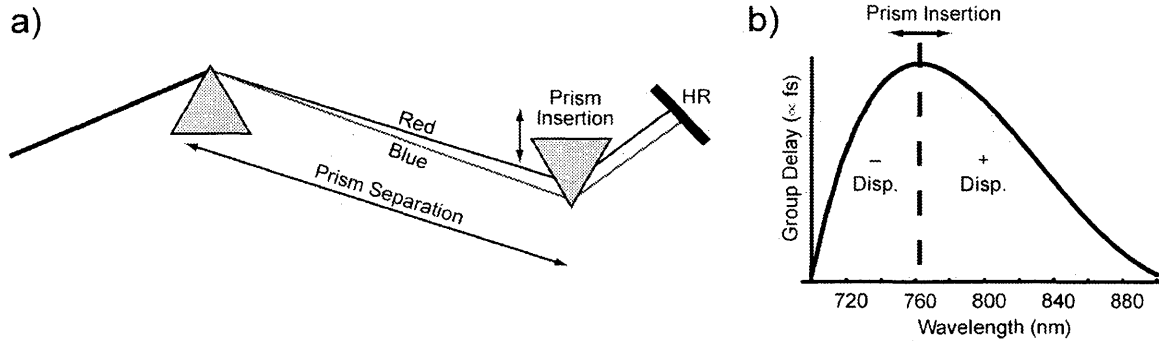


Figure 2.3 a) Prism pair for dispersion control. b) Group delay curve for prism pair.

Figure 2.3b shows the group delay curve for a prism pair with a tip-to-tip prism separation of 65 cm. The sign of the derivative of the group delay curve gives the sign of the dispersion. Changing the insertion of the second prism acts to move the peak of the curve to different wavelengths. A common way to characterize the depth of insertion is to quote the wavelength that just misses the tip of the second prism. This wavelength is not necessarily present in the system and is known as the reference wavelength. In Figure 2.3b the reference wavelength is 525 nm.

2.4 Initial High Power Ultrafast Laser System

This section describes the initial laser amplifier system used in the first experiments. The amplifier system was replaced by a higher energy version described in Chapter 3, but the laser oscillator and stretcher/compressor remained the same throughout the experiments.

2.4.1 Ultrashort Pulse Laser Oscillator

The seed pulses for all experiments presented in this thesis were generated from a self-modelocked Ti:sapphire laser illustrated in Figure 2.4 (KMLabs) [41]. The oscillator consists of two spherical 10-cm focal length spherical mirrors that focus the beam into the Brewster cut crystal and a flat output coupler (95% transmission), flat high reflector, and a fold mirror between the 2 prisms. The intracavity prism pair provides dispersion control and allows generation of pulses ~ 15 fs in duration. The oscillator is capable of producing up to 90 nm of bandwidth centered at ~ 800 nm. The laser is passively modelocked by the Kerr effect, which effectively adds an extra lens to the cavity in the presence of the short pulse, high intensity mode of operation. By aligning the static cavity around this Kerr lens, the laser is more efficient operating in the modelocked regime.

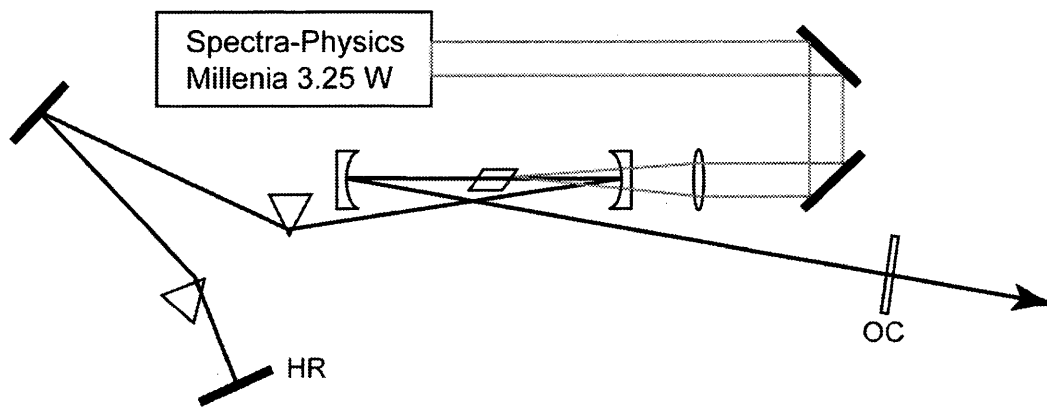


Figure 2.4 Kerr-lens modelocked laser.

The oscillator is pumped with 3.5 W of power from a Spectra-Physics Millennia laser. The 1-nJ, 15-fs pulses are then stretched to ~150 ps by an all-reflective pulse stretcher described in detail in the references [39, 42]. The pulse then travels through a Pockels cell (KMLABS PCD) between crossed calcite polarizers. This permits transmission of a single pulse during a 10-ns window that is timed to the laser oscillator by a frequency divider (Quantum Technology). The pulse divider receives an 86-MHz signal from a high speed photodiode placed in the oscillator and divides the 86 MHz pulse train down to 10 Hz. The pulse is then ready for amplification.

2.4.2 Multipass Amplifier

One of the first amplifier designs used in CPA systems was the regenerative amplifier design [2]. A regenerative amplifier is similar to a laser cavity, in that it uses a stable resonator design to confine a beam for amplification. A beam is injected into the cavity using a Pockels cell and polarizer arrangement. The beam takes ~20 passes through the gain medium and is switched out with the same Pockels cell. The stable cavity configuration results in high levels of amplified spontaneous emission; the cavity can lase on its own. The combination of the Pockels cell, the intracavity polarizers, and many passes in the cavity results in large amounts of material in the system. This amount of material can limit the recompression of the pulse without very careful correction.

The multipass amplifier design was developed to eliminate some of the problems associated with regenerative amplifiers. The multipass amplifier uses an unstable resonator configuration, so the Pockels cell and intracavity polarizer used for injecting and extracting the beam in a regenerative amplifier are not necessary. The three-mirror multipass amplifier used in the initial laser system is illustrated in Figure 2.5, and is based on the design first presented by Backus et al [43]. The only material in the amplifier is the Ti:sapphire crystal. This minimal amount of material greatly simplifies the recompression of the pulse.

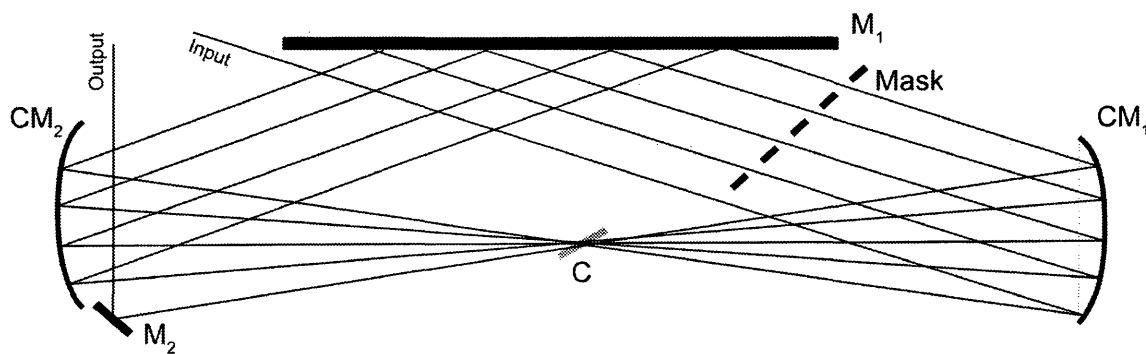


Figure 2.5 Basic three-mirror multipass amplifier design.

The multipass amplifier consists of a flat silver mirror (M_1) and two, 2" diameter, focusing mirrors of 1000-mm radius (CM_1 and CM_2). The two curved mirrors are separated by the sum of their focal lengths, at 100 cm. The flat mirror is positioned perpendicular to the other mirrors and approximately 15 cm from the line intersecting the

two curved mirrors. A collimated beam is injected into the ring towards the crystal (C) by the spherical mirror CM_1 . The beam is recollimated and directed towards the flat mirror, M_1 , by the curved mirror, CM_2 . The flat mirror directs the beam to a point offset slightly from the first pass on CM_1 . CM_1 focuses the beam in the crystal and directs the beam to a spot near the previous pass on CM_2 . With this configuration it is possible for a laser beam to make 1 to 12 passes (only four passes shown in Figure 2.5 for clarity) around the triangular loop, while on each pass reflecting from different points on the mirrors. This unstable cavity is different from a regenerative amplifier in that it does not use any additional switching optics in the cavity to inject and extract the beam. An additional flat mirror (M_2) extracts the beam after the desired number of round trips in the amplifier. The unstable design makes multipass amplifiers slightly less efficient than regenerative designs, because the beam takes a different path through the gain profile on successive passes.

A mask with a series of separate 2-mm holes is inserted into the amplifier near the flat mirror. This mask reduces amplified spontaneous emission (ASE) buildup in the cavity, because without it the ASE can take any path through the system. Because there is a mechanism in the multipass design to control ASE, unlike regenerative amplifiers, multipass amplifiers can run at higher gains (~ 9) than regenerative amplifiers. This results in fewer passes in the crystal. The fewer passes and no extra optical material in the design makes dispersion compensation easier compared to regenerative designs.

Because the spatial gain profile in the crystal is not perfectly flat, the center of the seed beam sees a higher gain than the edges. This results in shrinking the beam in the crystal, an effect known as spatial gain narrowing. Without correction the beam becomes larger on the curved mirrors, and the larger beams can make it difficult to cleanly extract the beam from the ring. The mask also helps control spatial gain narrowing, by limiting the beam size at the curved mirrors.

This amplifier design is capable of producing up to 2 mJ pulses at a kHz repetition rate. At higher repetition rates (>10 Hz) the crystal housing is typically cooled, to help counteract thermal effects in the crystal. The minimal amount of material in the system allows pulse compression down to ~ 20 fs without extensive spectral shaping [43].

After amplification, the pulses are compressed by a double pass on a grating pair (Section 2.3.1). Both the stretcher and the compressor gratings have 1200 grooves/mm, and the compressor has a throughput efficiency of $\sim 65\%$. The system used for the initial experiments presented here produced ~ 1.5 mJ pulses with durations of ~ 25 fs.

This is approaching the limit of what is currently achievable with a single stage of amplification using the three-mirror multipass design. To reach even higher energies, a second stage of amplification is typically used. For the second stage of amplification, a multipass configuration is used to take a moderate number ($\sim 4-5$) of passes at moderate gain ($\sim 4-5$) through the gain medium. Since the energy in the pulse is high, the energy can be efficiently extracted from the crystal at these low gains. The same three-mirror

multipass system described in Section 2.4.2 can be used for extra stages of amplification [3, 13].

2.5 Summary

This chapter provided a background in ultrafast design considerations. The dispersion of optical materials plays an important role in all ultrafast experiments. With careful control of the dispersion, ultrashort pulses can be expanded in time by factors of 10^4 or more and recompressed to nearly the same duration. As peak intensities of pulses become higher, new applications of chirped pulse amplification may be useful to control the intensities in laser interactions. A technique similar to this will be presented in Chapter 4 as a way to increase the energy yield in an optical parametric mixing process.

This three-mirror multipass amplifier design was used for the initial experiments presented in later chapters. It provided ~ 1.5 -mJ, 25-fs pulses at 10 Hz. These levels were close to the limits of a single stage of amplification with this amplifier design. For higher energy operation another stage of amplification or a redesign of the system would be needed.

CHAPTER 3 HIGH-ENERGY, DOUBLE- CONFOCAL MULTIPASS AMPLIFIER

3.1 Introduction

Current applications of high peak-power systems, for example, x-ray generation [44], laser-ion-beam acceleration [45], and hollow-fiber frequency conversion [15, 28, 29], demand a high-energy amplifier with high intensity contrast and good spatial beam quality. Currently, systems requiring more than a 1-2 millijoules per pulse typically rely on multistage amplifiers. The first stage uses a focused-beam geometry to efficiently amplify a seed beam to the millijoule level. A second stage uses a larger beam size in the gain medium with a lower gain to increase the energy. However, a multistage approach requires an extra Ti:sapphire crystal, pump laser, and amplifier cavity.

Beyond energy requirements, two important characteristics in current amplifier designs are beam quality and intensity contrast. Ideally, an amplifier does not adversely affect the ideal TEM_{00} beam profile from the oscillator. Without care, factors such as optical aberrations, hard apertures, and gain aperturing can degrade the ultimate output beam quality. Ultimately, poor beam quality inhibits the laser system's achievable focus size and intensity. This has adverse effects for micromachining and applications that require precise mode-matching. Since later experiments covered in this thesis depend on

efficient coupling of the laser light into a hollow fiber waveguide, high beam quality is vitally important for this system.

A second trend in ultrafast, laser system design is the intensity contrast between the main pulse and any prepulse or prelasing. Without correction the intensity of the prepulses can be high enough to distort or destroy an experiment before the main pulse arrives. The intensity contrast of a laser system is defined as the intensity any prepulses compared to the intensity of the main pulse. For example, current research in ultrafast x-ray generation has shown that the intensity contrast should be more than $1:10^8$ to generate x-rays with pulse durations in the tens of femtoseconds [12, 31]. While high intensity contrast is not required for the following parametric mixing processes described in the remainder of this thesis, it makes the system more appealing for other applications.

This chapter presents a new multipass amplifier design based on the 3-mirror architecture illustrated in Section 2.4.2. The final Ti:sapphire amplifier system produces over 10 mJ per pulse in a single stage, with high intensity contrast (10^9), and excellent spatial beam quality ($M^2=1.15$). This multipass design is scalable to higher energy and repetition rates [46].

3.2 High Energy Multipass Design

The central issue in high-energy amplification is the efficient extraction of the stored energy without adverse optical effects such as self-focusing or damage. The two main

sources of damage are the dielectric mirror coatings and the Ti:sapphire crystal surface. The mirror coatings have a lower damage threshold than the uncoated crystal surface, because the crystal is uncoated and at Brewster's angle. Self-focusing is typically not an issue in multipass amplifiers because of the minimal amount of material in the system. The Ti^{3+} saturation fluence of 0.9 J/cm^2 sets a *rough* scale for the final beam diameter for a desired energy (e.g. 1.4 mm diameter for 15 mJ output) [47]. However, given a desired level of energy extraction efficiency, the *actual* output fluence is a fixed fraction of the absorbed pump fluence, which in turn determines the small signal gain. For low-energy ($\sim 1 \text{ mJ}$) Ti:sapphire amplifiers, the beam in the crystal can be focused so that the amplified pulse has a reduced fluence on the mirrors. As the energy and the beam size increase, a collimated beam must be used to keep the amplifier within reasonable dimensions. At high gains the energy in the output beam can be greater than the saturation fluence of the Ti:sapphire crystal, which is greater than the damage threshold of nearly all current optical coatings. In the design presented here, a collimated beam can take many passes through the gain: this permits high extraction at a reduced gain that is compatible with the mirror damage threshold. With the use of a collimated beam, the output energy may be scaled up by increasing the beam sizes, provided the small-signal gain is held constant.

Figure 3.1 illustrates the optical layout of the new double-confocal design. A beam entering near CM_1 passes through the crystal and is directed by CM_2 to mirrors CM_3 and CM_4 . The equal tilt angle of the mirrors is adjusted such that the beam enters the crystal

at an incremented angle on each pass. The confocal placement of the mirrors ensures overlap in the crystal for all passes. The design presented here is similar to a three-mirror configuration by Backus et al, which produced amplified pulse energies of up to 1-3 mJ (section 2.4.2 and reference [43]).

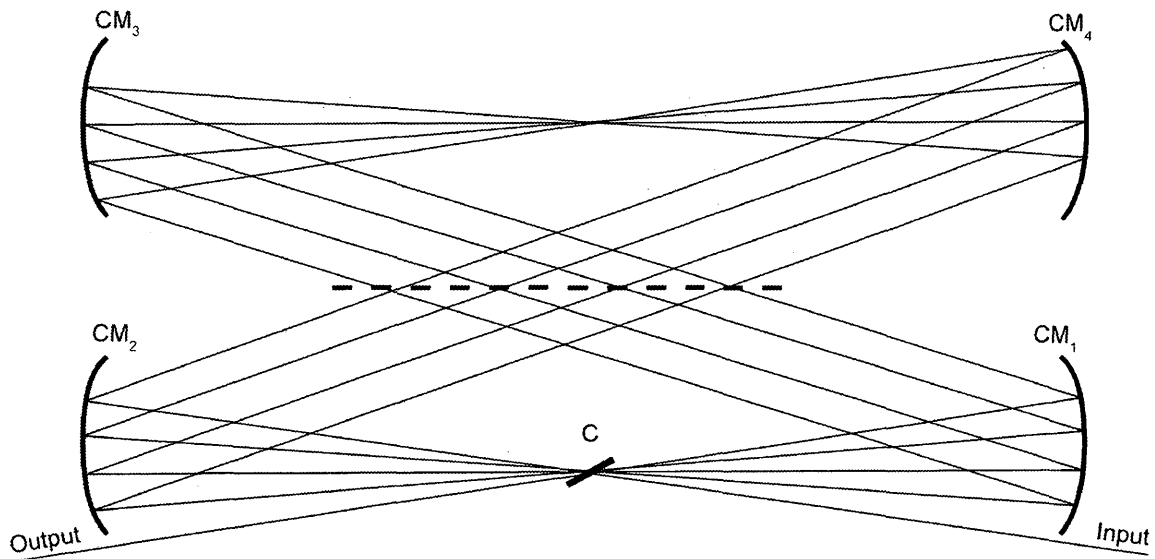


Figure 3.1 Double-confocal, multipass amplifier design.

The four-mirror system is an optically unfolded version of the three-mirror design, which allows a greater number of passes to be taken without the restriction of the length of the central mirror (at the location of the dashed line in Figure 3.1). The unfolded design also gives the option of directing to the crystal either a *focused* beam (as in the original three-mirror design) or a *collimated* beam (which focuses along the diagonal

between mirrors CM_2 and CM_3). In this way, a larger mode size for higher energy extraction can be employed. This is not possible in the three-mirror design, because the beam would be focused on the flat mirror and would quickly reach an intensity above the damage threshold of the mirror. It is possible to inject a beam with a divergence that places the focus in front of the crystal. However, this produces a smaller beam on the previous curved mirror. Only in the case of very high gain is this advantageous over using a collimated beam.

In the amplifier presented in this chapter, the curved spherical mirrors (CM_1 - CM_4) are $f = 250$ mm, 2" diameter, and the Ti:sapphire crystal (C) is Brewster-cut 6-mm thick, 10-mm diameter doped to absorb 95% of the incident 532-nm pump light. As many as 12 passes fit on 2" diameter mirrors; however only four passes are shown in Figure 3.1 for clarity. It is important to note that this system is half the length of the initial multipass amplifier presented in section 2.4.2 and reference [43].

3.3 Aberration Corrections

Since the cavity is shorter than the three-mirror design used initially, the angle of incidence on the spherical mirrors is larger. Because the cavity is unfolded and there is only one crystal, the beam takes twice as many reflections off the angled spherical mirrors. Figure 3.2 shows additional optics required for additional round-trips and to correct for aberrations. Multiple sets of passes can be taken with this design, multiplexed

by vertical offset on the curved mirrors. Between the two sets of 9 passes for the amplifier presented here, the μJ -level beam is focused through a saturable absorber, (SA), to improve the intensity contrast. Spherical lenses, L_1 and L_2 , were added to optimize the output beam quality by compensating for aberrations associated with the use of a collimated beam in the crystal and a relatively short cavity length.

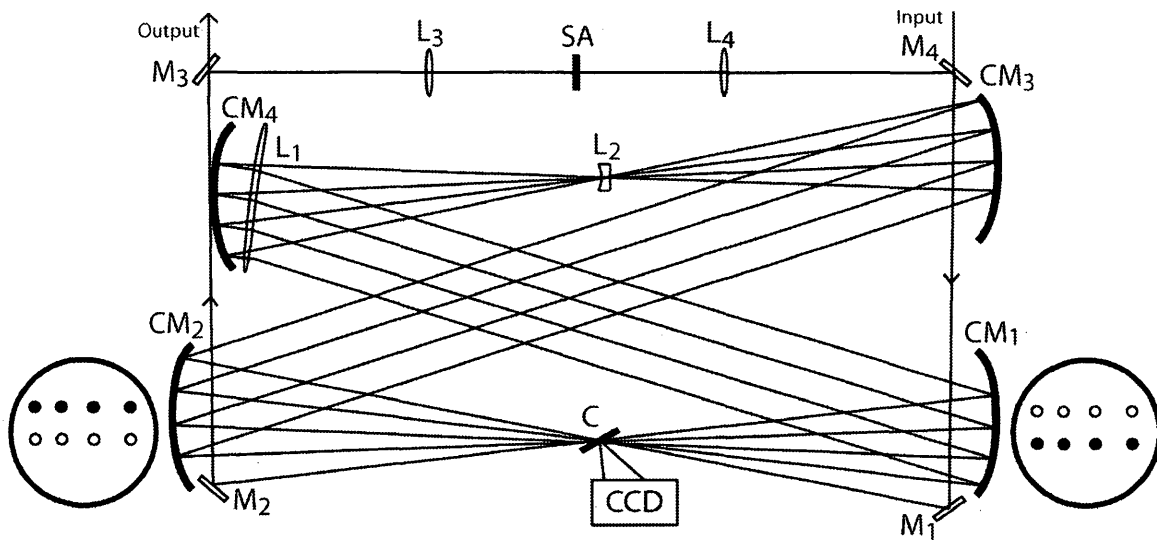


Figure 3.2 Complete double-confocal amplifier layout with correction optics.

Although the pump light is relayed to the crystal, the pump profile is not completely flat and the high gain results in substantial spatial gain narrowing. The resulting reduction in the beam size in the crystal causes saturation to occur earlier and at lower energy. This effect is illustrated in Figure 3.3a (thin line), which shows the results of a model of the spatially dependent saturated amplification experienced by an input pulse with a

Gaussian profile amplified in a medium pumped with a laser with a super-Gaussian profile $I(r) \propto \exp[-2r^6 / w_p^6]$. Without correction, the beam diameter initially shrinks; then after saturation is reached in the center, the mode begins to widen. The expansion of the mode to fill in the pumped area is gradual: during this process, the output energy is limited and the fluence in the center portion of the beam is near the damage threshold of the mirrors. In the three-mirror multipass design the spatial gain narrowing is still present. However, with a focused beam in the crystal, the beam becomes *larger* on the mirrors. The mask in the system fixes the beam size on the mirrors and serves to cancel the effect of spatial gain narrowing, but the hard aperture can degrade the output beam quality. To compensate for this effect in the double-confocal design, the focal length of one of the spherical mirrors was slightly shortened with the addition of a spherical lens $L_1, f = 3.5$ m, diameter = 2", so that the beam increased in size by 6% per pass (see Figure 3.3a, thick line). The mirror/lens combination was moved in to preserve the crossing point. The short leg also decreases the beam spacing per pass, though this was found to be manageable for 9 passes.

Astigmatism and divergence control were found to be important in this short cavity configuration. Geometrically, the automatic beam overlap in the crystal derives from the $2-f$ spacing between the curved mirrors. The diagonal distance is necessarily slightly longer, resulting in a gradual focusing of the collimated beam from pass to pass. This focusing is much stronger than the natural divergence of the Gaussian beam. A negative

correction spherical lens (L_2 , $f = -3$ m, diameter = 0.5") was placed at the second crossing point to correct for this.

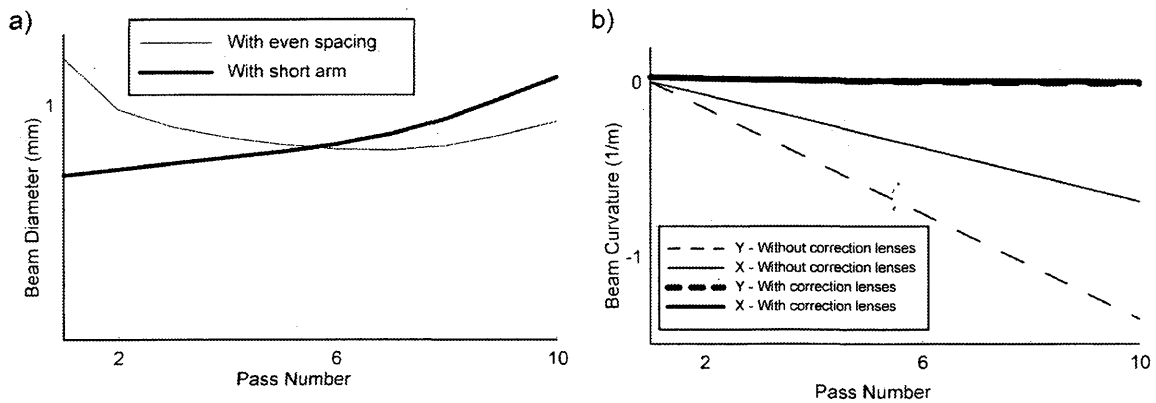


Figure 3.3 Evolution of the beam diameter (a) and the beam divergence (b) in the amplifier.

The mirror focus was optimized for horizontal beam overlap in the crystal by imaging the crossing point at the crystal face to a CCD camera. The sensitivity of the crossing point to the mirror separation was ~ 1 mm. The astigmatism resulting from the longer vertical focal length of the tilted spherical mirrors not only changed the beam shape, but also affected the vertical crossing of the second pass. A tilt around the horizontal axis of lens L_1 provided the required degree of freedom to reset the astigmatism on each round trip. The final output beam was slightly elliptical, but the residual astigmatism was within range to be corrected by the output beam expander. Figure 3.3b displays the evolution of the horizontal (solid line) and vertical (dashed line) beam divergence in the amplifier at

the crystal, calculated with the ABCD Gaussian beam propagation technique. The two pairs of lines (thin lines without correction lenses, thick lines with correction lenses) show that lenses L_1 and L_2 correct for both the divergence (shown in Figure 3.3b as the inverse of wavefront radius) and astigmatism of the beam.

These correction lenses make the compact configuration of the amplifier possible. With an additional factor of two in system length, making the length the same as the design presented in Section 2.4.2, the corrections are not required, because astigmatism varies as the square of the mirror tilt angle.

3.4 Amplifier Intensity Contrast

As amplifiers use higher single pass gains and become more efficient, the amplified spontaneous emission (ASE) in the cavity can reach high energy levels. The level of ASE preceding the pulse can reach intensities high enough to damage an experiment before the short pulse arrives. The multipass architecture is favorable for high contrast: the intracavity polarizer in a regenerative amplifier provides a surface for prepulses to be reflected in the output direction, and the cavity design allows the buildup and temporal concentration of ASE preceding the pulse. Also, the switching optics in regenerative amplifiers are not perfect and can allow light from the previous pass to leak out in the output direction. Even in the multipass design, ASE must still be suppressed by some means. In the three-mirror design, a mask with a series of holes is often placed in the

collimated section near the flat mirror to counteract both ASE buildup and spatial gain narrowing [43]. In addition to the energy loss, this technique introduces a hard edge on the beam that decreases the amplified spatial beam quality.

Another technique for ASE control is to use a saturable absorber that blocks low intensity light, but passes higher intensity light. For example, a standard Schott glass color filter can be used to block the low intensity ASE. When the short pulse is present the atomic absorption sites in the filter are quickly saturated, and the filter becomes transparent to the remainder of the pulse [48]. In the approach used here, the pulse is amplified to the microjoule level in 9 passes, extracted from the ring, and then focused through a saturable absorber (2-mm Schott RG850 color filter, see Figure 3.2). The filter passes 75% of the high energy seed pulse without any noticeable spectral change of the output pulse. The contrast before the stretched pulse is improved by the ratio of the linear to nonlinear transmission: $\sim 10^2$. In principle, placing a pinhole at the focus near the location of the saturable absorber may further improve the contrast. The beam is recollimated with a second lens and directed back to the crystal. The lens sequence approximates the relay imaging internal to the ring, maintaining the pointing stability. Maintaining rather than reversing the direction for the second set further reduces the ASE in the output direction, because if the beam is reversed all the ASE is directed towards the output. The returning beam enters the ring lower than the seed (M_1), and the output emerges above the seed beam on M_2 . The circles on the head-on view of the spherical mirrors in Figure 3.2 show the layout of the passes of the first (filled) and second (open)

set on the curved mirrors. Note that as long as the beam from M_4 to M_1 is collinear with the input to the first set, no additional alignment of the ring is required for the second set. For maximum gain the beams in the first set are focused in the crystal to be at the peak of the pumped region, and collimated in the second set to extract as much of the pump region as possible for maximum energy extraction.

3.5 Amplifier Performance and Characterization

The seed pulses used in the system originate from a Kerr-lens mode-locked Ti:sapphire oscillator (KMLabs) [41] (see Section 2.4.1). The oscillator was pumped with 3.5 W from a Spectra Physics Millennia laser. The 1-nJ, 15-fs pulses are stretched to ~ 150 ps by an all-reflective pulse stretcher [39, 42] (see Section 2.3.1) with a 1200 grooves/mm grating. The pulse is divided down to 10 Hz by a Pockels cell pulse selector before being injected into the amplifier. The amplifier was pumped at 10 Hz by a frequency-doubled Nd:YAG laser (Continuum Model 681C-10), which provided up to 100 mJ per pulse at 10 Hz. The pump beam was split equally by a 50% beamsplitter to pump both sides of the crystal. This prevents any hotspots in the beam from exceeding the damage threshold of the Ti:sapphire crystal. The pump spot in the crystal was relay-imaged from the oscillator in the Nd:YAG pump laser to achieve as flat a gain profile as possible. The pump beams are focused through the dielectric mirrors CM_1 and CM_2 to a point approximately 9 mm in front of the crystal, giving a pump spot size of

~1.3 mm in the crystal. The crystal, a 6-mm thick, uncoated and Brewster cut, was doped to absorb 95% of the incident pump light. The passive losses per round trip were measured to be approximately 5%. All the reflective optics were coated with a high power, broadband high reflective coating (CVI TLM1). L_1 and L_3 have a standard near infrared antireflective coating and L_2 was uncoated.

3.5.1 Energy Extraction

As described above, the seed beam was focused in the crystal for the first set of 9 passes. The input beam diameter for the second set of passes in the crystal was ~600 μm , which, without gain, expanded to 1.4 mm by the final pass. With 46 mJ of pump energy absorbed by the crystal, the measured peak single pass gain in the Brewster crystal was 3.8, and the output energy from the amplifier was typically 10 mJ, corresponding to a conversion efficiency of 19%. Figure 3.4a shows an image of the fluorescence from the crystal as viewed through mirror CM_4 using an interference filter at 680 nm (width 10 nm). The dashed line is a lineout through the center of the image with no seed present, and the solid line shows the reduction in fluorescence with the seed present indicating the amplification is in saturation. The lineout shows saturation of the pump energy, as well as the location of the residual energy.

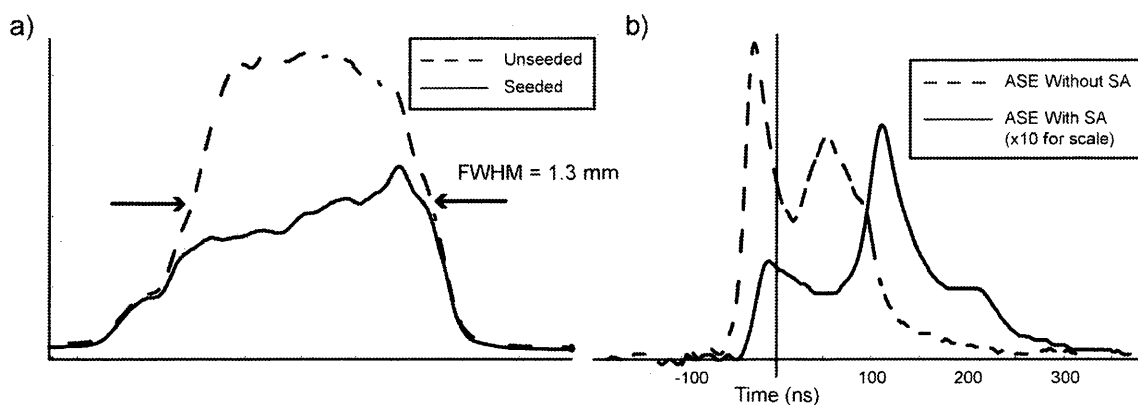


Figure 3.4 a) Lineout of an image of the fluorescence from the crystal. b) Diode traces of the output ASE background.

The output energy is currently limited by the relay design for the pump. With the focus in front of the crystal, there is air breakdown at higher pump energy (~ 45 mJ per side). A different relay design for the pump should allow for a larger pump spot and increased output energy. The CCD camera imaging the beams in the crystal serves as a monitor for the day-to-day alignment of the seed direction and pump position. The ring mirrors rarely need to be adjusted.

3.5.2 Intensity Contrast

With the output pulse energy at 8.6 mJ the seed pulse was blocked and the output energy decreased to 80 μ J. The majority of this ASE emerges *after* the output pulse. A high-speed photodiode was used to record the time-dependence of the ASE. Figure 3.4b shows diode traces of the unseeded amplifier with the origin of the time axis set to the

time that the amplified short pulse exits the amplifier. The time dependent power of the ASE was calculated by normalizing the integral of the diode signal without a seed to the measured ASE energy under the same conditions. The energy preceding the output pulse could then be estimated by integration of the diode signal up to the output pulse arrival time. The majority of the ASE was within 25-ns before the main pulse, containing $\sim 0.8 \mu\text{J}$, yielding an intensity contrast of $\sim 10^9$. The dashed line in Figure 3.4b shows the trace without the saturable absorber. In this case the total ASE energy was 3.5 mJ and the contrast was reduced to 10^7 . Note that inserting the saturable absorber reduces both the amplitude and duration of the ASE before the pulse because it extinguishes the ASE buildup from the first few passes. While this method can only detect the light preceding the pulse on the nanosecond scale, it does show a reduction of most of the extra ASE. Since the saturable absorber is used with the stretched pulse, it does not affect prepulse within $\sim 150 \text{ ps}$ of the main pulse. To characterize the prepulses on the picosecond level, a FROG with high dynamic range and a $\sim 150 \text{ ps}$ duration would be needed.

3.5.3 Pulse Duration

The multipass architecture allows the phase compensation to be characterized with frequency-resolved optical gating (FROG) using the unamplified oscillator beam. A zero-order waveplate was inserted to pass the beam through the Pockels cell. A standard multishot second harmonic generation (SHG) FROG setup was used for the following

pulse duration measurements[49]. Figure 3.5 shows the results of these SHG-FROG measurements. Figure 3.5a shows the retrieved frog trace of the compressed, amplified pulse. The trace is shown as a filled contour plot with contour lines at 1, 2, 4, 6, 10, 20, 40, 60, and 80% of the peak value. With 55 nm of unamplified bandwidth passing through the system, the pulse can be compressed to 35 fs with fourth-order-limited phase. The gain-narrowed amplified spectrum is also shown in Figure 3.5b, with a FWHM of 38 nm. The residual phase across the bandwidth is shown by the thin line. The compressed, amplified output pulse (Figure 3.5c) was found to be 35 fs in duration. Preshaping the input spectrum or adding an intracavity filter [50] will allow the bandwidth to be increased. The additional material in the ring (now 18 mm of BK7) can be reduced to 6 mm with a thinner lens L_1 and shaping the crystal to eliminate L_2 , or to zero by eliminating L_1 and using a longer cavity and a shorter-radius CM_4 . Phase calculations indicate that the addition of a prism pair to allow compensation of a portion of the fourth-order phase will allow compression down to 22 fs [13].

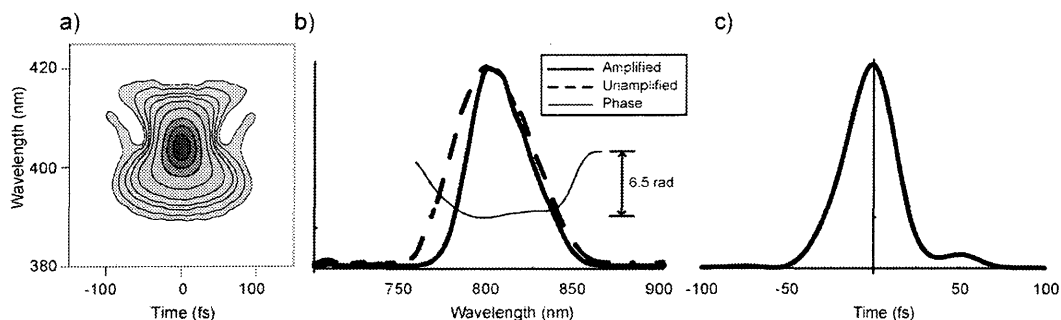


Figure 3.5 a) Retrieved FROG trace. b) Unamplified spectrum (dashed) and

amplified spectrum (solid), and the phase across the bandwidth (thin). c) Retrieved pulse shape.

3.5.4 Beam Quality

After focusing the compressed output beam with an $f \sim 1250$ mm concave spherical mirror, an image of the spot was recorded with a CCD camera at 13 longitudinal positions. At each datapoint 2-4 images were taken. These images were imported into *Mathematica* and ~ 10 lines around the center of the beam were averaged, then fit to a Gaussian function in order to extract an e^{-2} radius. The extracted beam radii were fit to the form expected for an aberrated beam [51],

$$W(z) = W_0 \sqrt{1 + (z - z_0)^2 / z_R^2} \quad (3.1)$$

with z_R , the Rayleigh range given by

$$z_r = \frac{\pi W_0^2}{M^2 \lambda}. \quad (3.2)$$

Using these relations, the measured M^2 was found to be 1.15. The solid line shows a fit to the data yielding an $M^2 = 1.15$. The dashed line represents the ideal ($M^2 = 1$) divergence from the measured focal spot. The ratio of the horizontal and vertical diameters of the beam at the lens was 1:1.1. Both the horizontal and vertical foci were in the same location, indicating that the astigmatism is well corrected. An image of the compressed amplified beam with lineouts and best Gaussian fits is shown in Figure 3.6.

The high quality of the amplified beam can be attributed to the lack of any aperture in the system and to the aberration corrections in the ring.

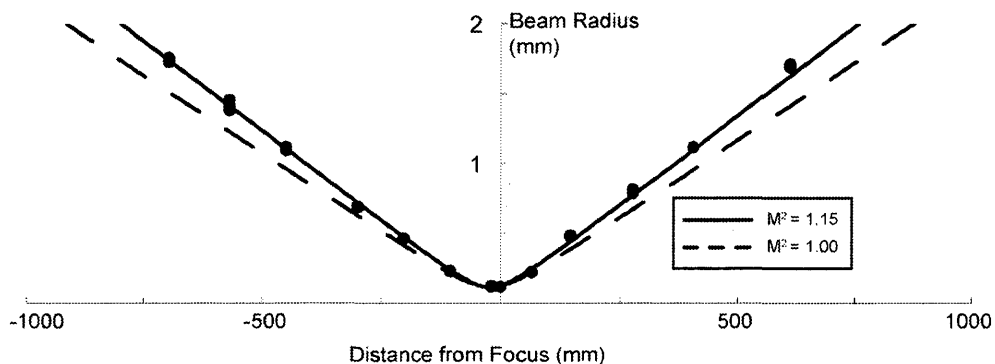


Figure 3.6 Beam radius as a function of distance from the focus.



Figure 3.7 a) Image of amplified, uncompressed beam. b) Lineout from center of the image with best Gaussian fit. c) Lineout of best focus with Gaussian fit.

3.6 Applications to Other Systems

A kilohertz repetition rate version of the amplifier was used briefly in another system with 500-mm focal length mirrors, and the correction optics were not necessary. With a

different arrangement for relay imaging the pump to the crystal, which allows for a larger pump volume without the intermediate focus, still higher energy can be obtained from this amplifier. Since this design allows for multipass operation with reduced small signal gain, it should be useful for multipass amplification in gain media with higher saturation fluence.

To illustrate the ultimate energies this multipass amplifier is capable of supporting, a simple model based on the B-integral can be used. The overall limit on the energy is the saturation fluence of 0.9 J/cm^2 . For, example a 3-mm diameter beam in the crystal gives a saturation energy of $\sim 64 \text{ mJ}$. Using this value for the beam diameter, and a four-mirror cavity based on 500-mm focal length spherical mirrors. The duration is assumed to be 150 ps, as in the current system. There are two main sources of nonlinear phase buildup in the system. The first is the 10-mm long Ti:sapphire crystal, and second, the air in the region of the focus on the diagonal path between the mirrors. The model computes the B-integral for the last five passes assuming energies of 100, 50, 20, 6, and 1 mJ. To compute the phase buildup in the focal region the energy and cross sectional area is assumed to be constant over the confocal parameter. The B-integral for the crystal is only 0.05 radians, while the air contributes 0.66 radians to the nonlinear phase. The typical goal for systems is to limit the B-integral to 1 radian or less. To achieve pulse energies above 100 mJ, longer pulse stretch factors can be used to further reduce the intensity in the amplifier.

3.7 Summary

This chapter has presented the development of a simple, single-stage, compact Ti:sapphire based amplifier capable of generating pulses of 10 mJ energy at 10 Hz (compressed to 7 mJ). The amplifier has a unique four mirror multipass design with good contrast, beam quality, and stability. This design should be directly applicable to higher repetition rate systems. The high temporal contrast makes this amplifier system directly useful for x-ray generation and other applications requiring temporally clean pulses. The excellent beam quality is ideally suited for coupling to the hollow waveguides used in the other experiment presented in this work. B-integral scaling predicts the amplifier design is capable of supporting pulse energies on the 100 mJ level.

CHAPTER 4 ULTRAVIOLET OPTICAL PARAMETRIC CHIRPED PULSE AMPLIFICATION

4.1 Introduction

Frequency conversion by use of gaseous nonlinear optical media can eliminate the pulse-width limitations in the ultraviolet that are inherent in techniques that use crystalline media. Previous work has used a simple focused-beam geometry, to frequency-triple 1-mJ, 22-fs pulses at 800 nm to produce generated 16-fs, 1- μ J ultraviolet pulses [52]. More recent work has demonstrated very efficient generation of ultraviolet light through optical parametric amplification of pulses confined in gas-filled capillary waveguides [15]. Phase matching is possible by tuning the gas pressure to achieve a balance between the gas dispersion and the modal dispersion of the waveguide. The difference-frequency mixing ($3\omega = 2 \times 2\omega - \omega$) allows the generated ultraviolet light to be in the lowest-order spatial mode. Conversion efficiencies to the ultraviolet of 20% of the guided pump beam (2ω) have been reported. Through cross-phase modulation, the bandwidth of the ultraviolet pulses has been increased to ~ 16 nm and compressed to transform-limited 8-fs pulses at 270 nm [28].

However, in the previous work the energies directly available from the chirped pulse amplification system was modest (~ 1 -2 mJ), thus only by using all of the available

energy in the shortest pulses could the proper intensities be reached in the capillary. With more energy available, either by using the amplifier system presented in Chapter 3 or by adding a second stage of amplification, it is necessary to stretch the pump (2ω) and seed (ω) beams in time to maintain the proper intensity in the capillary. Thus, more energy can be transferred to the ultraviolet. It is possible to compress the generated ultraviolet light with simple material or a prism pair set for positive dispersion as illustrated in Section 2.3.3, to durations similar to that of the input seed beam. The following is a survey of the processes that control ultraviolet pulse generation in the optical parametric chirped pulse amplification process.

4.2 Other Methods of Ultrafast Ultraviolet Generation

Direct and sum-frequency mixing has been used to generate microjoule levels of ultraviolet down to wavelengths of 200 nm or less. However, because of the group velocity walkoff in the nonlinear crystals, the ultimate pulse durations are limited to ~ 130 fs [16]. This group velocity walkoff is a result of the different indices of refraction for the different wavelengths in the process causing the beams to propagate at different speeds through the crystal. Thus, it is not possible to use longer crystals to increase the conversion efficiency. These techniques are not tunable because they are based on the harmonics of a Ti:sapphire laser.

Optical parametric amplifiers (OPA) have been shown to produce pulses with wavelengths down to 300-400 nm [14, 25, 26]. However, finding a nonlinear medium that is transparent at ultraviolet wavelengths is a major problem for crystal-based OPAs. Even with materials that are transparent in the deep ultraviolet region, the overall efficiency will be reduced because of two-photon absorption in the crystal, because nonlinear crystals are typically only transparent down to ~ 210 nm. Because of this it is not even possible to consider producing pulses below 200 nm. Optical parametric amplification in hollow waveguides is still the most accepted technique for generating tunable deep ultraviolet light through a parametric mixing process [14].

4.3 Phase Matching in Hollow Core Waveguides

Many nonlinear optical effects are best studied in a guided wave geometry to lengthen the interaction length and thus the overall efficiency of the process [53]. Solid fibers are not often used for pulses shorter than ~ 1 ps because the high peak intensities of short pulses is above the damage threshold of most fibers. The material dispersion will cause the pulses to quickly broaden in time.

Hollow core fibers use a different guiding mechanism than conventional optical fibers. In solid fibers the pulse is guided by total internal reflection, which requires that the middle of the fiber have a higher refractive index than the outer layers of the fiber. The transmission of the pulse is low loss; the loss depends primarily on the absorption of

the beam by the fiber material. However, hollow core waveguides guide the beam through Fresnel reflections at the capillary walls. The guiding mechanism has been comprehensively studied [54, 55]. Because the electric field of the guided pulse goes to zero at the walls of the capillary, problems with damage to the capillary material and strong dispersion are almost nonexistent in hollow core waveguides. In this way beams with peak intensities of $\sim 10^{15}$ can be guided without damage to the capillary [29]. Another advantage is that the modal dispersion of capillary waveguides provides an adjustable phase parameter that can be used to phase match the pulses in harmonic generation and frequency mixing of ultrafast pulses. However, the losses due to Fresnel reflections that guide the wave through the capillary attenuate the beam much more than conventional solid fibers.

4.4 Optical Parametric Amplification Process

Two electromagnetic waves with different frequencies propagating in a nonlinear crystal will generate a traveling polarization wave at the difference frequency. If the polarization wave travels at the same velocity as the freely propagating electromagnetic wave, amplification will occur. The two incident waves are called the “pump” and “signal” waves and the resulting wave is called the “idler.” Under the right conditions the idler wave can mix with the pump beam to produce a traveling polarization wave at the signal frequency, resulting in growth of the signal wave. The process continues with the

signal and idler wave both growing and the pump beam decaying as a function of distance in the crystal. Figure 4.1a shows a simple schematic of the process, illustrating how the beams are labeled, and Figure 4.1b shows a photon view of the OPA process.

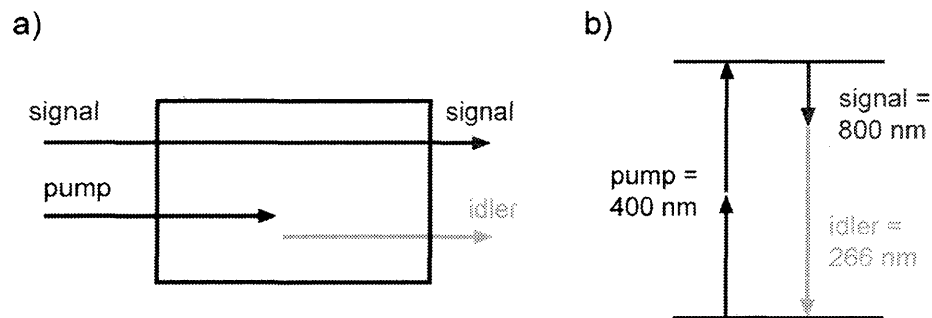


Figure 4.1 a) Schematic of different waves in OPA process. b) Photon view of the OPA process.

Since each pump photon has energy $h\nu_p$ and creates a single photon at the signal and idler frequency ($h\nu_s$ and $h\nu_i$) energy conservation requires that

$$\frac{1}{\lambda_p} = \frac{1}{\lambda_s} + \frac{1}{\lambda_i}. \quad (4.1)$$

To achieve amplification, it is required that at each of the three frequencies the generated polarization waves travel at the same velocity as the freely propagating electromagnetic wave. This will be the case if the k -vectors satisfy the momentum matching condition,

$k_p = k_s + k_i$. For collinearly propagating waves this may be written as

$$\frac{n_p}{\lambda_p} - \frac{n_s}{\lambda_s} - \frac{n_i}{\lambda_i} = 0 \quad (4.2)$$

where, n_i , n_p , and n_s are the refractive indices for each wave.

Since the three indices of refraction depend on wavelength, the direction of propagation in the crystal, and on the polarization of the waves, it is generally possible to use birefringence and dispersion to find conditions under which the phase matching condition (equation (4.2)) is satisfied.

A characteristic of all parametric devices is tunability. With the pump providing input at the fixed wavelength, λ_p , small changes in the signal wavelength and the phase matching condition will result in a change in the idler wavelength. Tuning is typically achieved by using the angular dependence of the birefringence of an anisotropic crystal [47].

4.5 Propagation Phase for Gas Filled Waveguides

In general, the propagation modes in a hollow waveguide are the Bessel functions with the boundary conditions requiring the field go to zero at the capillary walls. The lowest order mode profile in a hollow waveguide given by the linearly polarized EH_{11} hybrid mode with $E(r) \approx E(0)J_0(k_r r)$ and a transverse wave number $k_t = \mu_{11}/a$, where μ_{11} is the first zero of the Bessel function, J_0 and, a , is the inner radius of the capillary waveguide.

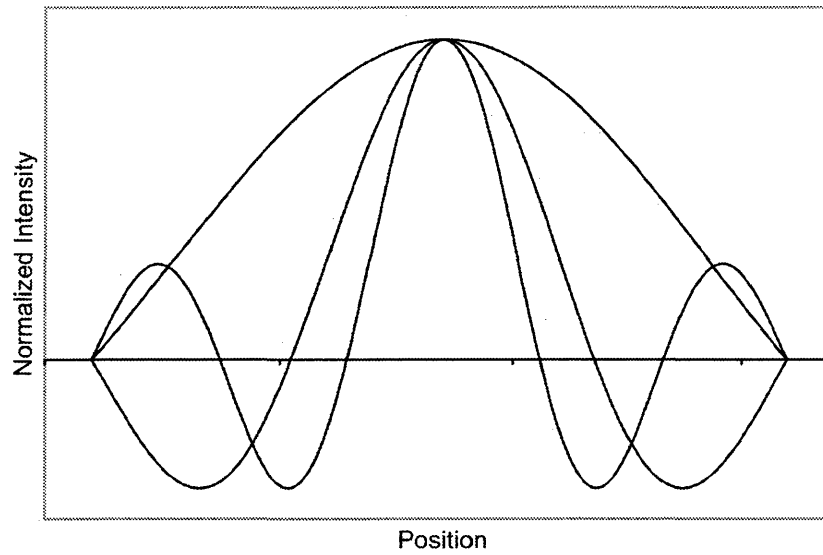


Figure 4.2 First three (EH_{11} , EH_{12} , EH_{13}) hollow-core waveguide modes.

The loss per meter in hollow-core waveguides is given by the relation

$$\alpha = \left(\frac{\mu_{nm}}{2\pi} \right)^2 \frac{\lambda^2}{a^3} \operatorname{Re}(v_{EH}^2) \quad (4.3)$$

with

$$v_{EH} = \frac{v^2 + 1}{2\sqrt{v^2 - 1}} \quad (4.4)$$

and $v = n_{\text{cap}}/n_{\text{gas}}$. μ_{nm} is the modal constant for the azimuthal (m) and radial (n) modes [54]. The wavelengths of interest in these experiments are 800, 400, and 266 nm, and the transmission per meter in a 150- μm diameter bore capillary are 52%, 88%, and 92% respectively. Figure 4.3 graphically illustrates the loss through a 2-m, 150- μm

bore diameter capillary for the first three guided modes for 800, 400, and 266 nm light. For all modes the shorter wavelengths experience lower loss. This illustrates the mode filtering properties of the hollow-fiber guiding process, which helps to produce output in the lowest order capillary mode.

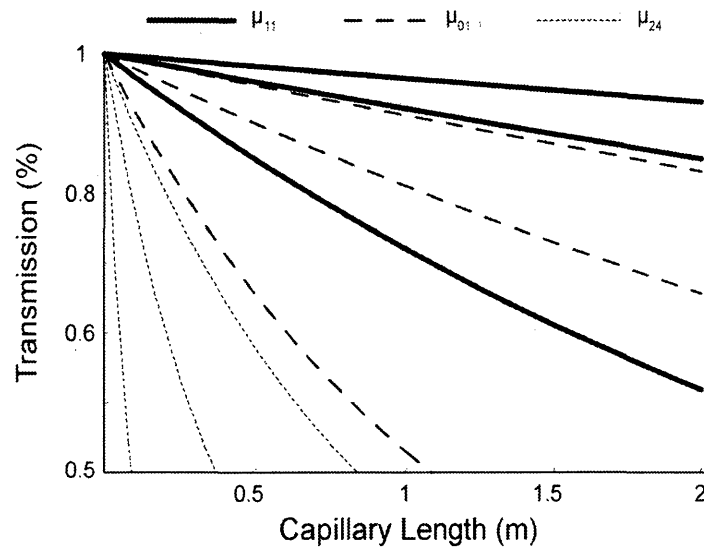


Figure 4.3 Transmission efficiencies through a 150- μm capillary for the first three guided modes for 266 (top), 400, (mid) and 800 nm (bottom).

Because the capillary acts to counteract the normal diffractive spreading of the wave, the waveguide adds a geometrical component to the wave vector. The longitudinal wavenumber is then given by $k^2 = n^2 k_0^2 - k_t^2$, where n is the index of refraction for the

capillary contents and k_0 is the vacuum wavenumber. The full form of the propagation factor is given by

$$k = \frac{2\pi n(\lambda)}{\lambda} \left[1 - \frac{1}{2} \left(\frac{\mu_{nm}}{2\pi} \frac{\lambda}{a} \right) \left[1 + \text{Im} \left[\frac{v_{EH} \lambda}{\pi a} \right] \right] \right]. \quad (4.5)$$

The last term is the absorption of the wave by the capillary walls. Physically this term is small because the wave is nearly zero at the walls of the capillary. This term can be neglected because $\lambda \ll a$. The expression for the index of refraction of a partially ionized gas is given by

$$n(\lambda) = 1 + N_a \delta(\lambda) - \frac{N_e r_e \lambda^2}{2\pi}. \quad (4.6)$$

Where N_a and N_e is the atomic and electron density, r_e is the classical electron radius, and $\delta(\lambda)$ contains the gas dispersion information. Using this expression for the refractive index in equation (4.6) and expanding and neglecting terms much less than $1/\lambda$ the propagation factor takes the form

$$k(\lambda) \approx \frac{2\pi}{\lambda} + \frac{2\pi N_a \delta(\lambda)}{\lambda} - N_e r_e \lambda - \frac{\mu_{nm}^2 \lambda}{4\pi a^2}. \quad (4.7)$$

The four terms in equation (4.7) are the vacuum, gas, free-electron, and waveguide sources of dispersion.

4.6 Phase Matched Ultraviolet Pulse Generation

Typically for the wavelength ranges in these experiments, noble gases are used in the normally dispersive regime as the gas in the capillaries. There are two regimes for phase matching in the hollow fiber setup, direct harmonic conversion ($\omega_{\text{signal}} = 3\omega_{\text{fundamental}}$) and parametric amplification ($\omega_{\text{signal}} = 2\omega_{\text{pump}} - \omega_{\text{idler}}$). In direct harmonic conversion the phase matching is controlled by the higher harmonics generated in higher modes to phase match the process [29]. In q^{th} harmonic generation a beam at frequency ω_1 propagates in a waveguide and generates light at the q^{th} harmonic, $\omega_q = q\omega_1$. Then to first order the phase mismatch is

$$\begin{aligned} \Delta k &= \Delta k_{\text{mat}} + \Delta k_{\text{mode}} \\ &= \frac{2\pi N_a}{\lambda_q} (\delta(\lambda_q) - \delta(\lambda_1)) - \frac{\lambda_q}{4\pi a^2} (\mu_q^2 - q^2 \mu_1). \end{aligned} \quad (4.8)$$

μ_1 and μ_q are the modal constants for the fundamental and second harmonic beam.

Because the noble gases are normally dispersive over the typical wavelength ranges, $\Delta k_{\text{mat}} > 0$. In an unguided geometry the phase velocity of the generated shorter wavelength light is slower than the fundamental. However, in a capillary if the generated light is produced in a higher order mode the phase velocity is increased. Thus the process can be phase matched. When $\mu_q > q\mu_1$ (second term in equation (4.8)), the pressure of the gas (thus N_a) can be adjusted to phase match the process ($\Delta k = 0$). However, the

generated light is placed in a higher order mode. This decreases the effective overlap of the two beams and decreases the efficiency of the process. Lengthening the interaction length will not increase the efficiency, because the phase matching bandwidth decreases with the interaction length and the propagation loss (equation(4.3)) is greater in a longer capillary.

Mixing through the parametric process ($\omega_{\text{signal}} = 2\omega_{\text{pump}} - \omega_{\text{idler}}$) makes it possible to obtain phase matched conversion with all wavelengths in the same waveguide mode. The better overlap between the three modes will greatly improve the conversion efficiency. In the general case of mixing with the two frequencies ω_1 and ω_2 , with the difference frequency $\omega_3 = N\omega_2 - M\omega_1$, and the phase mismatch

$$\begin{aligned} \Delta k &= k_3 + Mk_1 - Nk_2 \\ &= 2\pi N_a \left(\frac{\delta_3}{\lambda_3} + \frac{M\delta_1}{\lambda_1} - \frac{N\delta_2}{\lambda_2} \right) - \frac{1}{4\pi a^2} (\lambda_3\mu_3 + M\lambda_1\mu_1 - N\lambda_2\mu_2). \end{aligned} \quad (4.9)$$

Now the order M and the wavelength λ_1 can be chosen so that $\Delta k_{\text{mode}} > 0$, with all beams in the lowest order mode (μ_{11}). When $\lambda_1 = 2\lambda_2$ and $\mu_1 = \mu_2$, $\Delta k > 0$ for all λ_3 modes. In many previous experiments two photons of the second harmonic of Ti:sapphire (400 nm) is used as the short wavelength pump, and the fundamental (800 nm) as the signal to produce idler light in the ultraviolet (266 nm). The 800-nm light can be replaced by light from a conventional crystal based optical parametric amplifier to produce tunable light throughout the ultraviolet spectrum. For example, in the previous demonstration of

this technique an optical parametric based amplifier with a tuning range of 590-2600 nm was used with the 400 nm pump pulses to produce ultraviolet output in the range of 217-305 nm [29].

4.7 Optical Parametric Chirped Pulse Amplification

A method to circumvent these restrictions is to make use of the optical parametric chirped pulse amplification (OP-CPA) technique that has been demonstrated in crystal nonlinear optics [56, 57]. Similar to chirped pulse amplifiers, more energy can be used by making use of longer pulses while maintaining the optimal intensity in the gas (10^{12} - 10^{13} W/cm²).

While the concept shares similarities with what has been done in crystals, there are several important differences. Although crystal OP-CPA has recently been demonstrated down to 400 nm [25], hollow fiber OP-CPA does not have the same phase matching and transmission limitations and will be able to be scaled to much shorter wavelengths, well into the vacuum ultraviolet. In crystal OP-CPA, an injected, chirped pulse is amplified with very high gain ($\sim 10^3$ /pass). Without special tailoring of the temporal and spatial profiles of the pump, this high gain can lead to strong narrowing of the amplified spectrum and constriction of the spatial profile. In contrast, hollow fiber OP-CPA is a frequency conversion process. Since the injected, chirped infrared pulse has an intensity

of the same order as that of the pump, it experiences low gain. The majority of the pump energy is transferred to the ultraviolet pulse.

4.8 Simulations

To predict the effects of different pulse and waveguide parameters on the ultraviolet generation, a Fourier split-step routine developed in past references was used to model the process [58]. This model includes simultaneous equations for the first five harmonics of the fundamental. The code uses the Fourier split-step method to solve the five coupled nonlinear propagation equations as a function of capillary position, waveguide dimension, gas type and pressure. The dispersion and waveguide losses are calculated at each step in the frequency domain using the full refractive index expressions for the gas and waveguide. The nonlinear terms such as the nonlinear source terms and the self and cross-phase modulation are calculated in the time domain.

The code assumes that all harmonics propagate in the lowest order waveguide mode. The Runge-Kutta algorithm is used to solve the five coupled nonlinear expressions for the harmonic fields. Spectral broadening due to self and cross phase modulation are included in the nonlinear equations. The code accounts for back-conversion from higher harmonics into the lower harmonics and also for the phase mismatch for the different fields. Arbitrary fields are specified as the starting points for the first and second harmonic and this allows the testing of different chirps on the input pulses. At each step

the code calculates the shape of the pulse in both the spectral and time domain. The chirps are carried through to all the generated fields and the output field can be tested for compressibility. Some different parameter sets will be considered in the following sections.

4.8.1 High Energy Chirped Pulse

Figure 4.4 shows a contour plot of the ultraviolet intensity versus pressure and capillary length. The contour intervals are at 10% of the total energy in the ultraviolet pulse, with the higher energies darker. In this example calculation, a Gaussian pump pulse (400 nm), 1.2 ps FWHM duration (transform limited) and 1.7 mJ in energy is injected in a 150–mm core capillary along with a 1 ps FWHM stretched seed pulse (800 nm, initially 30 fs) with energy of 150 μJ . Under these conditions and at the optimum pressure of 66 torr there is 790 μJ of ultraviolet light produced corresponding to 46% conversion to ultraviolet from the pump.

Figure 4.5 shows the transfer of energy from the pump (thin) to both the seed (dashed) and generated ultraviolet light (thick) at the optimal pressure. The pump is depleted as both the ultraviolet and infrared seed pulses are amplified.

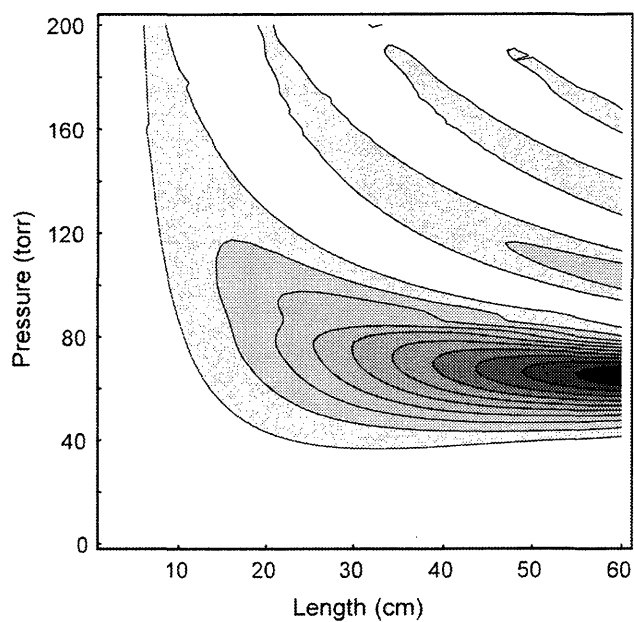


Figure 4.4 Normalized ultraviolet output versus capillary length and gas pressure.

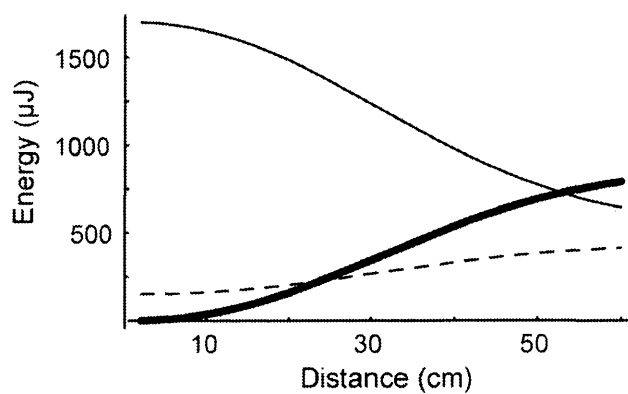


Figure 4.5 Energy transfer from pump (thin) to seed (dashed) and ultraviolet (dashed).

Figure 4.6 shows the temporal profile of the pump (thin), seed (thick), and generated third harmonic light (dashed) at the same parameters as above, and illustrates the process

is in saturation. The ultraviolet pulse shown here has a spectral width of 3 nm FWHM. With more careful control of the initial infrared duration, even wider ultraviolet spectrums can be produced as seen in the next section.

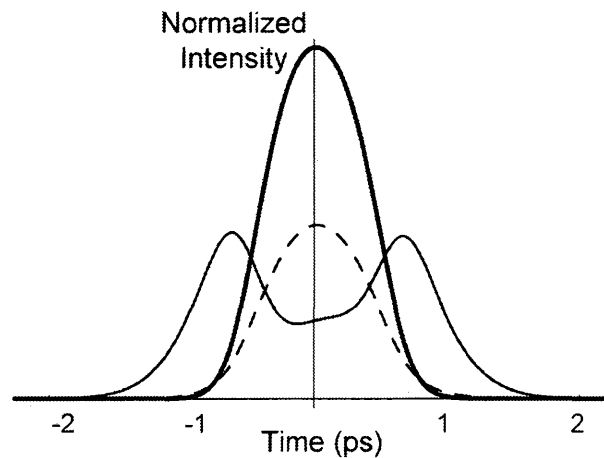


Figure 4.6 Temporal profile of output pulses from capillary.

4.8.2 Optimum Seed Duration

From an energy perspective, the pump and seed pulses should be of similar durations. Figure 4.7 shows the depleted pump pulse at the capillary exit with three different seed durations. In the simulation, a 1-ps pump pulse with 500 μJ of energy is used as a pump pulse with a 500 μJ seed pulse of durations: 250 fs (thin line), 500 fs (medium line), 800 fs (thick line). The amount of signal light for each case was 140 μJ , 210 μJ , and 240 μJ respectively. The plot shows the location and amount of residual pump energy. In

the shortest pulse case, some back conversion is present as indicated by the small modulation in the larger dip. This is an undesirable side effect of using too high intensities in the process. This modulation is also present in both the temporal and spectral profile of the ultraviolet pulse.

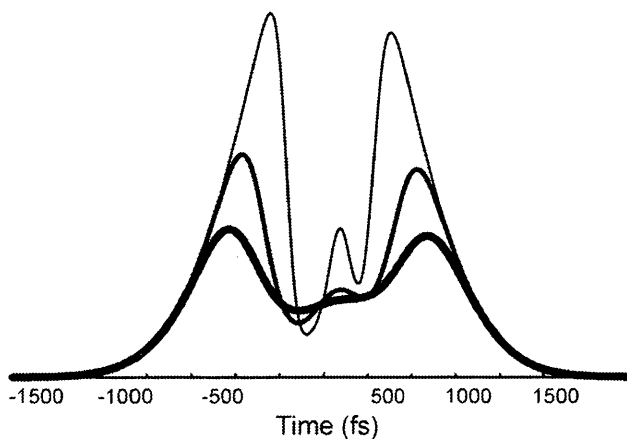


Figure 4.7 Depleted pump profiles for different seed durations.

Figure 4.8a shows the resultant ultraviolet pulse spectra of both an ultraviolet pulse generated with the same parameters as the previous section and another with the same parameters except the IR seed is only chirped to a duration of ~ 430 fs FWHM. This shows that in both cases, despite the fact that the ultraviolet pulse is created out of nothing, there is very little spectral gain narrowing. The input pulses are shown in Figure 4.8b. These pulses produce a wider bandwidth (~ 5 fs) in the ultraviolet, because the entire infrared pulse is contained in the peak of the blue pump pulse. This wider

bandwidth allows compression down to the 30 fs level. By using a wider bandwidth seed pulse it is possible to generate even shorter pulses in the ultraviolet.

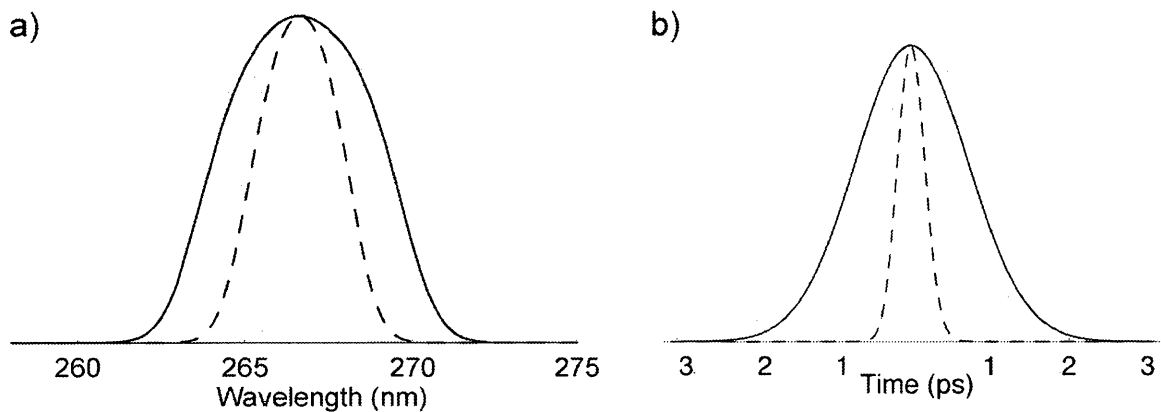


Figure 4.8 a) Comparison of output UV spectrum with different IR seed durations. b) Optimal input pump (solid) and seed (dashed) pulse durations for wide ultraviolet bandwidth.

4.8.3 Ultraviolet Pulse Compression

It is important to discuss the issue of ultraviolet pulse compression because it has bearing on the ultimate scalability of this approach. First, it is straightforward to see that for a narrow band pump (blue) and positively chirped seed (IR), the generated ultraviolet will be negatively chirped. Thus, first order compression is possible with normally dispersive fused silica. Calculations indicate that the third order dispersion (TOD) must also be corrected to achieve pulses at the 25-fs level.

Since

$$E_3 e^{i\phi_3(\omega_3)} \propto E_2^2 E_1^* e^{-i\phi_1(\omega_1)} \quad (4.10)$$

phase matching condition implies $\phi_3(\omega_3) = -\phi_1(\omega_1)$. Upon Taylor expansion we find

$$\phi_3(\omega_3)\Big|_{\omega_{03}} = \phi_3(\omega_{03}) + \Delta\omega_3 \phi_3'(\omega_{03}) + \frac{1}{2} \Delta\omega_3^2 \phi_3''(\omega_{03}) + \dots \quad (4.11)$$

then using the relation $\omega_1 = 2\omega_2 - \omega_3$ and the phase matching condition to change variables

$$\phi_3(\omega_3)\Big|_{\omega_{03}} = -\phi_1(\omega_{03}) + \Delta\omega_3 \left(-\frac{\partial\phi_1}{\partial\omega_1} \frac{\partial\omega_1}{\partial\omega_3} \right)\Big|_{\omega_{03}} + \dots \quad (4.12)$$

and then

$$\phi_3(\omega_3)\Big|_{\omega_{03}} = -\phi_1(\omega_{03}) + \Delta\omega_3 \phi_1'(\omega_{03}) - \frac{1}{2} \Delta\omega_3^2 \phi_1''(\omega_{03}) + \dots \quad (4.13)$$

The odd orders of phase change sign while the even orders do not. Unfortunately the third order dispersion of glass is the wrong sign and adds to the TOD of the seed. While some compression would be possible with simple material, the residual third order may limit the compression of the pulses. However, a prism pair set for positive dispersion has the opposite third order dispersion sign than material (see Table 2.1) [40]. This will allow compensation of the produced ultraviolet up to residual fourth order. Simulations indicate that transform limited compression down to ~ 30 fs should be possible with simple material, while for shorter pulses a prism pair should be used to compensate for the higher order dispersion.

Figure 4.9 shows the output ultraviolet pulse (Section 4.8.2) compressed with a prism pair set for positive dispersion. The tip-to-tip prism separation is 28 cm and the reference wavelength is 205 nm. The FWHM of the compressed pulse is 27 fs, which corresponds to a compression factor of ~ 30 from the output ultraviolet. The thin line represents the transform limit of the output ultraviolet pulse shape. The good agreement between the transform limit and the simulation of the pulse compressed with prisms shows that the prism pair adequately compresses the pulse without excessive higher order dispersion buildup.

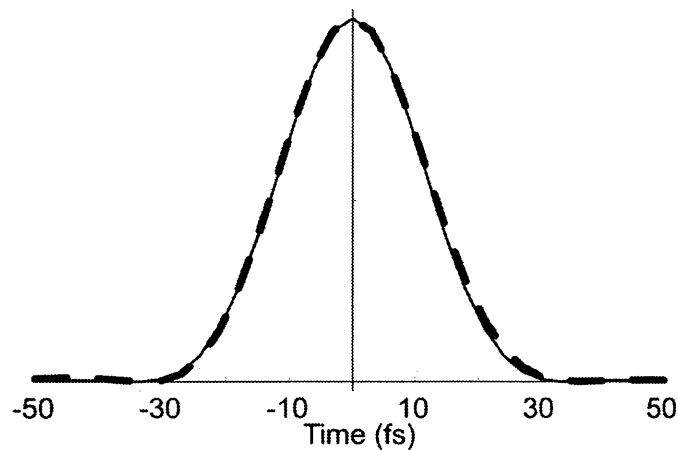


Figure 4.9 Generated ultraviolet pulse compressed with prism pair (thick dashed) compared to Fourier transform limit (thin).

4.9 Summary

This chapter provided a survey of the processes that are involved in hollow-fiber chirped pulse optical parametric amplification. Hollow fiber mixing offers advantages over parametric mixing in crystals such as: longer interaction length without group velocity walkoff and the ability to be scaled to much shorter wavelengths without the absorption issues present in mixing processes in solid media. By using parametric mixing ($3\omega = 2 \cdot 2\omega - \omega$) instead of direct mixing (3ω), the generated ultraviolet light can be phase matched and generated in the lowest order capillary mode, providing excellent mixing efficiency and beam quality. By using different pump light or replacing the seed pulse with light from a conventional optical parametric amplifier, tunable light throughout the ultraviolet spectrum can be generated.

The simulation results show that it is possible to use chirped pulses to extract more energy from the capillary. Also the resultant ultraviolet pulses can be compressed with simple material or a simple prism pair set for positive dispersion. This will allow completely scalable output in the tunable in the ultraviolet spectrum. With this approach, ultraviolet energies in the millijoule range should be attainable.

CHAPTER 5 INITIAL UV-OPCPA EXPERIMENTS

5.1 Introduction

This chapter describes the initial experiments in producing ultraviolet light through frequency mixing in gas-filled capillary waveguides. The main goal of these experiments was to show an improvement in ultraviolet yield and efficiency by using longer duration input pulses. This chapter also describes the construction of a mixing setup similar to the previous experiments in frequency mixing in hollow fibers [15, 28]. The experiments in this chapter use the three-mirror amplifier described in Section 2.4.2, so the energy available was moderate (1.6 mJ, 25 fs). Because the energies available for the process were moderate, the required pulse stretch factors were small. Because of this, the pulse durations of the input pulses were controlled by inserting variable amounts of glass in the beam paths. The results show that even with moderate energies there are advantages to using longer duration pulses to maintain the proper intensities in the interaction, thus maximizing the overall efficiency of the conversion process. In addition, the mixing process is highly dependent on having a high energy, focusable pump source, and methods for generating this pump were explored.

5.2 Producing Pump Light

The pump pulses for all of the experiments presented in this thesis are frequency-doubled Ti:sapphire light at 400 nm. Thus, scaling the energy output of the frequency conversion in the capillary is closely linked with the problem of efficiently doubling a wide bandwidth infrared pulse while maintaining good spatial beam quality and temporal pulse shape in the doubled light. The original plan was to use a thick (5-mm) KDP crystal to achieve high conversion efficiency to the blue light while also creating a longer duration pump pulse through the material dispersion. Although the conversion efficiency was high (~50%), the doubled pulse was distorted in both the temporal and spatial domains. The spatial distortions reduced the coupling efficiency to the lowest order mode of the capillary. It is possible that the spatial distortions arise from back-conversion from the doubled beam to the fundamental wavelength with a phase shift. This phase shift acts like a $\chi^{(3)}$ self-focusing effect, which will change the spatial mode of the doubled light [59].

In the temporal domain, most of the doubling occurs in the first part of the crystal before the onset of the narrower phase matching bandwidth. The pulse profile was examined through measurements with an all-reflective, self-diffraction, frequency-resolved optical-gating setup (SD-FROG, Figure 5.1a) [28]. The output pulse consisted of a narrow peak with a sloping tail on the leading edge (the blue lags the infrared during propagation through the crystal) resulting in an effectively short pulse. This pulse would

have still required more dispersion to achieve the proper pulse duration. The temporal pulse shape from the SD-FROG measurement is shown in Figure 5.1b.

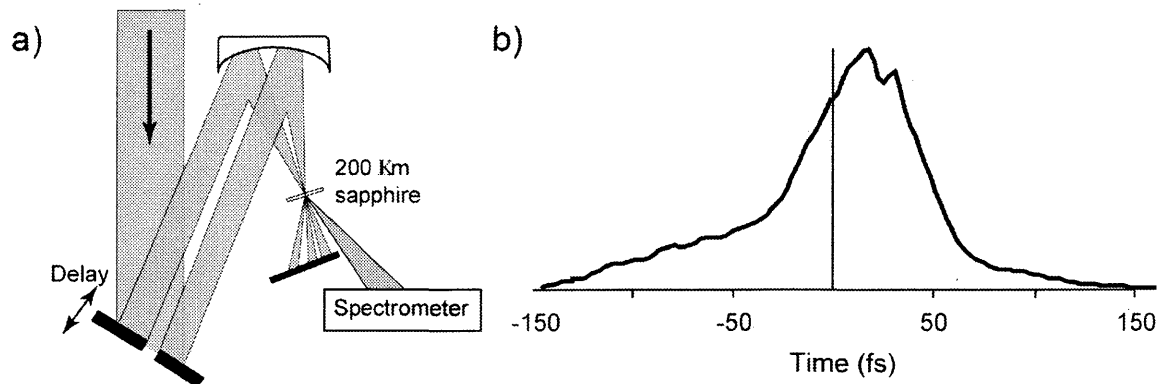


Figure 5.1 a) Dispersion-free self-diffraction FROG. b) Reconstructed blue pulse.

The dispersion-free self diffraction FROG works as follows. A large diameter beam is centered on two square mirrors separated by ~ 1 mm. This creates two beams that propagate collinearly. One of the mirrors is placed on a delay stage, and this provides the time delay present in all FROG and autocorrelation setups. The two beams are then reflected by a spherical mirror that simultaneously crosses and focuses the beams. An interaction plate is placed at the focus of the spherical mirror. When both pulses are present in the interaction plate, an interference pattern is formed. Because of the dependence of the index of refraction of most materials on the intensity of the light at high intensities, a diffraction grating is formed. A portion of one of the pulses is

diffracted by the generated grating, and by simultaneously recording the time delay and the spectral information of the diffracted light, a FROG trace can be constructed.

Because of the difficulties with efficiently generating long duration pump pulses, a temporary solution was devised to serve as a proof of concept. A short infrared pulse was used to generate the blue light efficiently. Then, optical windows (BK7 glass) were inserted into the blue beam to stretch it slightly. This was able to yield moderate chirp rates before nonlinear effects inhibited coupling to the lowest order mode of the capillary.

5.3 Preliminary UV-OPCPA Results

For the experiments in this section, the laser system described in Section 2.4 was used. The laser system produced 1.8 mJ pulses compressed to 30 fs. The experimental setup for the hollow fiber mixing is shown in Figure 5.2. A window was used in front of the BBO crystal to create a short infrared pulse at the capillary entrance at the same compressor setting that gave a short pulse at the doubling crystal. To minimize the problem of temporal and spatial distortion seen in the first experiment, a thin (0.5 mm) BBO crystal was used to generate the blue pulse from the fundamental. After conversion a 1/4" BK7 window stretched the blue pump pulse to 110 fs. A half-wave plate in the fundamental beam aligned its polarization with the doubled beam's polarization, because the doubling process generated the doubled light at 90° to the fundamental light. The duration of the infrared pulse was controlled with additional 1/4" BK7 windows. Both the

blue and infrared beams were synchronized and focused into the capillary (ID: 150 μm , length: 30 cm). The beams were separately focused into the capillary. Since both beams were approximately the same size (~ 3 mm), they were focused with different focal length lenses (500 mm for infrared and 750 mm for blue) for optimal coupling to the capillary. The optimum focal length for each beam was calculated by assuming that the focal spot should be 60% of the capillary inner diameter. However, this value was used as a starting point and the best focal length was found experimentally by trying a few lenses around the optimum value and choosing the lens that maximized the capillary transmission. Both beams' lenses were mounted in XYZ-translation mounts to provide the degrees of freedom to overlap both the blue and infrared focal points at the entrance to the capillary.

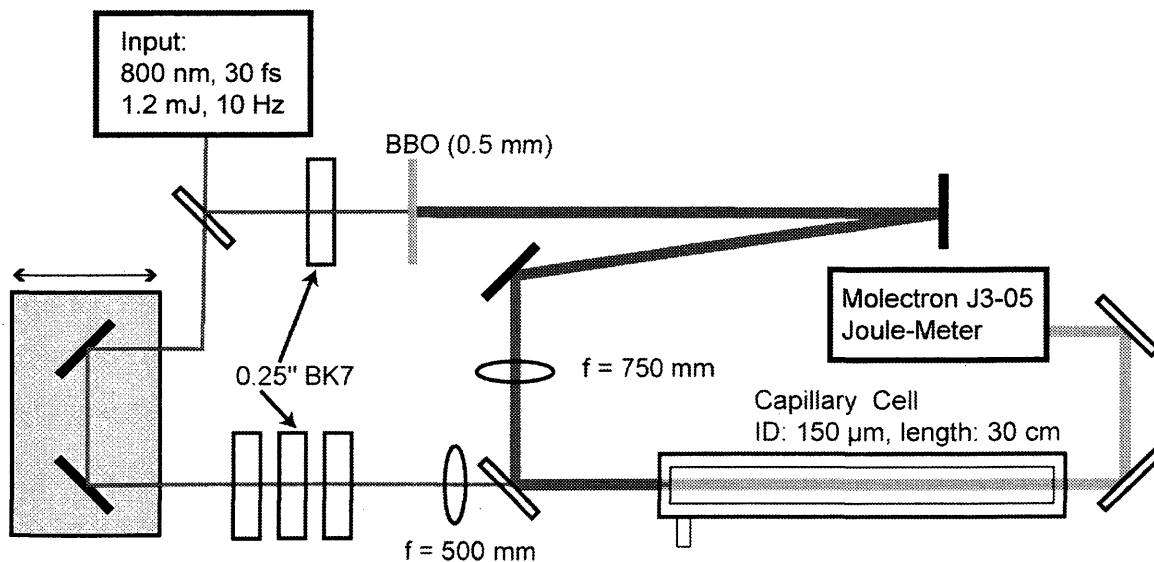


Figure 5.2 Initial OP-CPA setup.

The capillary tube was mounted in a gas cell with uncoated fused silica entrance and exit windows. To measure the energy produced in the ultraviolet, two ultraviolet coated, dielectric mirrors (CVI-Y4) isolated the ultraviolet light from the 800- and 400-nm light. With the timing off of the zero point, less than 1 μJ of 800- and 400-nm light reached the energy meter (Molelectron J3-05).

Argon was chosen for the gas in the cell because the optimum phase matching pressure is ~ 100 torr, and it is low cost, safe, and easily obtainable. Other noble gases have been shown to work, but the efficiency was roughly the same for all gases. As a rule of thumb, heavier gases have a larger nonlinear index, n_2 , but create larger dispersion, so the optimum phase matching pressure is lower [58]. A low gas pressure in the capillary is desirable to minimize absorption losses in the generated ultraviolet. However, argon does not have a two-photon absorption band in the ultraviolet region of the spectrum, so even at higher pressures argon does not attenuate the ultraviolet.

The argon pressure in the cell was adjusted to maximize the phase matched ultraviolet signal. In these very first experiments the optimum pressure was found to be 550 torr with a smaller peak at 470 torr. This did not coincide with the predicted value of ~ 75 torr. This is most likely due to coupling the seed and pump beams to higher order modes instead of the lowest order mode. Once more experience was gained in coupling the beams to the lowest order capillary mode, the low-pressure peak was more pronounced, as will be seen in the experiments presented later. Nevertheless, the energy considerations are the same at the low and high-pressure peaks. The transmitted energies at the exit of

the capillary cell for the blue and infrared were 40 μJ and 35 μJ out of 115 μJ and 153 μJ respectively. As the duration of the infrared pulse was increased by adding more BK7 plates and then resynchronizing the pulses, the ultraviolet energy increased, from 4 μJ to 11 μJ as shown in Figure 5.3. This is a clear indication that the conversion process was in saturation. The infrared durations were 45 fs, 51 fs, 57 fs, and 63 fs for zero to three BK7 plates respectively.

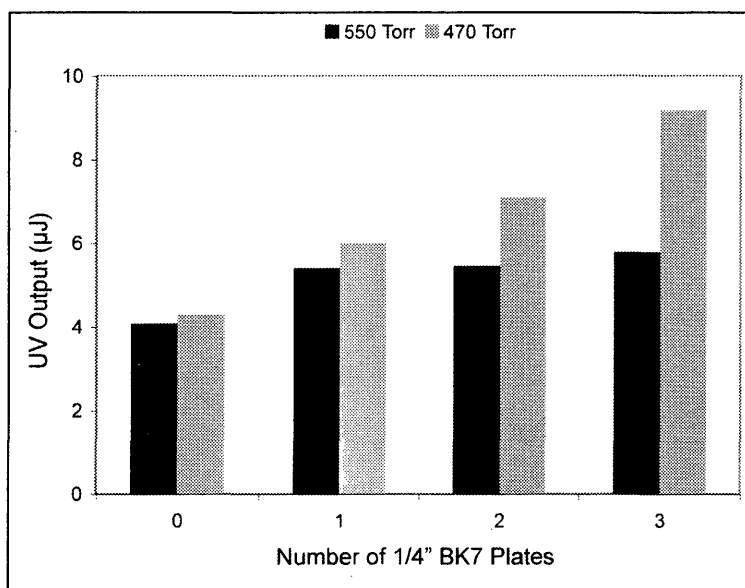


Figure 5.3 UV output versus IR pulse duration.

In the absence of saturation, and for constant energy input, the yield would go down with an increase in the duration (thus a decrease in intensity) of the fundamental.

Eventually the process becomes saturated, where the seed beam can deplete a portion of

the pump energy. If the seed pulse is shorter than the pump pulse, there is pump energy that is not utilized in the process. If this is the case, increasing the seed duration increases the ultraviolet yield, because the seed pulse can sweep out more of the pump energy.

Additionally, there is a reduced degree of self and cross phase modulation (SPM and XPM), both of which can reduce the saturated conversion efficiency. SPM is a result of the intensity dependence of the index of refraction. The rising edge of the pulse causes the index of refraction to rise, and the falling edge causes the index to fall. This can result in spectral changes to the input pulses. Even the low intensity ultraviolet signal pulse sees these index distortions because the pulses are temporally overlapped; this is known as cross phase modulation (XPM). It is important to note that even when the input intensity (which determines the conversion efficiency) is held constant, as the pulse durations are increased, the frequency shifting that results from SPM and XPM is reduced, because these effects depend on the temporal derivative of the intensity.

This initial approach, while useful to demonstrate the desired principles, is not easily scaled to much higher energy, because it is difficult to produce high blue energies with a thin doubling crystal. To further scale to higher energies in the ultraviolet, another method had to be found to produce high energy in focusable, long duration blue pulses.

5.4 Scalable UV-OPCA Experiment

Because the energies available for the mixing process were modest, short pulses had to be used to achieve high conversion efficiencies to the blue, thus the intensity in the doubling crystal must be high. A key requirement for the following experiments was to generate high blue energy pulses with long durations. Using a short pulse to generate high blue energies and material to stretch the pulse is possible, but this results in degradation of the spatial mode because of the high intensities in the crystal. Another method that has been used in the nanosecond regime to efficiently double pulses with thick crystals is to cross two oppositely chirped pulses in a doubling crystal. By crossing the two chirped pulses inside a BBO crystal, the sum frequency mixing can be phase matched across the entire bandwidth, resulting in a longer, narrowband output pulse with thicker crystals [60, 61]. The benefit to this method is that the intensity in the doubling crystal is reduced by using the longer (~ 1 ps), chirped pulses instead of the short (~ 30 fs) pulses.

In the previous demonstration of this technique, the two oppositely chirped pulses were produced with two separate grating compressors, because the required pulse durations were on the order of nanoseconds. In this setup, only one grating compressor was used as shown in Figure 5.4. The beam was split before the compressor, and one beam was passed through a 10-cm block of BK7. Both beams (side by side) were sent

through the same grating-compressor set to give equal but opposite chirps. This single-grating approach is possible here because the required chirps are moderate.

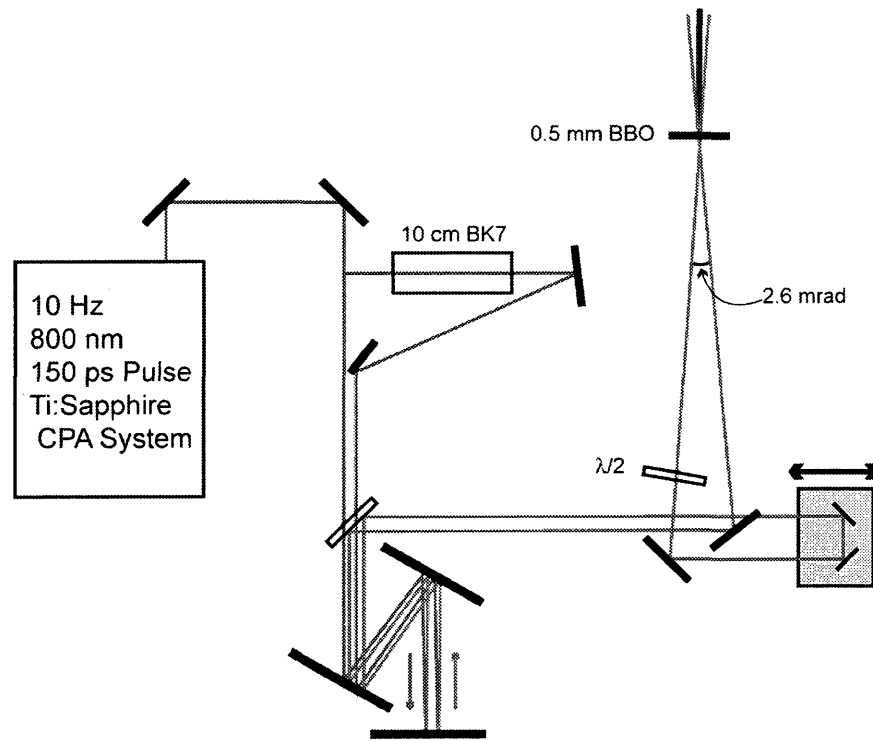


Figure 5.4 Setup for scalable blue production.

Both beams were vertically offset, and then crossed at a shallow (2.6-mrad) angle in a BBO crystal (0.5-mm). The phase matching angle was controlled by rotating the crystal around the horizontal axis. Because of conservation of momentum, the sum frequency beam exited between the two crossed beams. Several factors had to be considered when choosing the optimum crossing

angle would result in the best efficiency because the spatial overlap would be maximized. To achieve such small angles, the distance over which the beam travels is on the order of 3 m or more. Secondly, if the angle is small, the crystal is very close to the phase matching angle for all three beams. This results in more blue energy being produced in the directly doubled beams, which decreases the amount of energy in the mixing beam. At a smaller crossing angle, less energy is lost to the directly doubled beams because of the larger phase matching angle difference.

A feature seen here that was not reported in the previous work involving long pulse durations, was that at high intensities some self-diffraction was observed. The two crossed beams interfered, and their interference pattern created a grating because of the intensity dependent index of refraction. Similarly to the SD-FROG, a portion of the beam saw the grating and was diffracted. This resulted in a line of beams, because of the higher orders of diffraction. The most intense mixed beam was in the center with the lower intensity beams at the edges. It is desirable to minimize this effect to maximize the energy in the mixed beam. If the intensity is too high, up to six or seven orders of diffraction were observed, and the mixed beam energy was lower. By increasing the crossed beam sizes, thus reducing the intensity, only the first few diffracted orders were observed, and the center beam energy was optimized.

It is best to use a systematic procedure to quickly converge on the optimum mixing parameters. For example, if the phase matching angle for the mixed beam is off, it is still possible to reach a locally maximized signal by adjusting the timing. The procedure for

aligning the mixing setup was to maximize the direct mixing for each pulse individually. This procedure was used at low energy to avoid damage to the crystal because short pulses were present at the crystal. For the pulse with no material, the compressor distance was set to give a short pulse at the BBO crystal, and the crystal phase-matching angle was adjusted to maximize the conversion efficiency. The procedure was repeated for the beam that passed through the BK7 block. This beam required a longer compressor length to compensate for the material. Then the compressor and crystal phase matching angle were both set between their respective maximum positions. The beams were then synchronized to peak the mixing signal. With proper alignment, this setup produced conversion efficiencies of up to 40% from the fundamental, similar to direct frequency doubling.

A half-wave plate was inserted in the positively chirped beam before the BBO crystal, which left a small amount of infrared in the beam that did not convert to the blue. This infrared pulse was used to seed the mixing process in the capillary. Both the blue and infrared beams were synchronized and separately focused into the capillary setup as illustrated in Figure 5.5. For this experiment the measured throughputs for the 800- and 400-nm beams were 71 and 83 μJ , corresponding to transmission efficiencies of 38% and 40% respectively. For the dimensions of this capillary (ID: 120 μm , Length: 63 cm), much higher transmission of the lowest order mode is possible (52% and 88% respectively).

The optimum pressure was experimentally found to be 86 torr, by monitoring the ultraviolet energy while the pressure was reduced from atmosphere down to the 1 torr level. In this experiment approximately 13.7 μJ of ultraviolet energy was measured, corresponding to 14% conversion efficiency from the pump (blue).

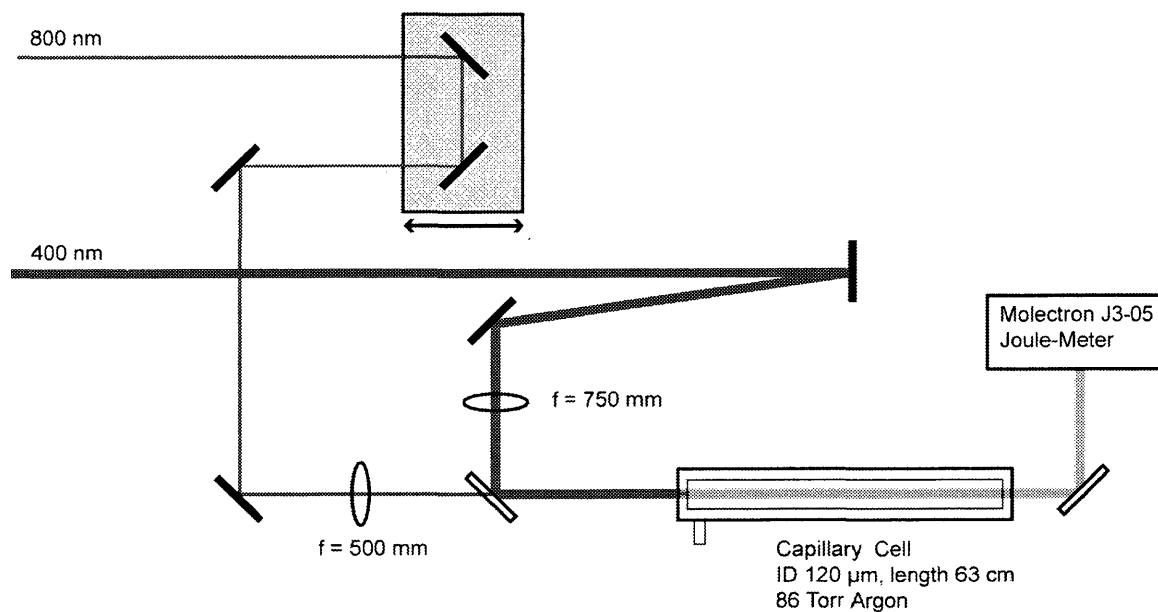


Figure 5.5 Experimental setup for final OP-CPA experiment.

5.5 Summary

These initial experiments demonstrate higher energy output in the hollow fiber frequency conversion process by using longer duration, higher energy input pulses, and a method for generating narrow-band frequency-doubled pulses with a single compressor

grating. While the increases in energy output over previous work were modest, these results show that similar energies can be achieved with longer pulses. This suggests that even at low energy there is benefit to using chirped pulses in the mixing process. It is probable that even in the previous demonstrations of this technique, chirped pulses were used. In the publications the pulse durations were not carefully controlled and monitored; only the shortest achievable duration of the Ti:sapphire laser system was documented [15, 28]. Nevertheless, to scale the mixing method to the hundred-microjoule level or more, chirped pulses will definitely be required.

The ultraviolet energy in the experiments was limited by the pump energy in the capillary. Mixing the oppositely chirped infrared pulses in the doubling crystal generates the blue light efficiently while maintaining moderate intensity in the crystal preserving the spatial beam quality. However, the fundamental beam quality still limits the ultimate beam quality in the doubled pulse. By increasing the stretch factor in the infrared, higher energies can be used to produce blue light in the millijoule range.

CHAPTER 6 HIGH-POWER ULTRAVIOLET

OP-CPA

6.1 Introduction

With the new multipass amplifier design, much more energy was available to use in the optical parametric system. However, with more energy in the beams some small changes to the system were necessary to utilize all of the available energy. The goal was to achieve similar conversion efficiencies to the ultraviolet from the pump as in the previous experiments. This would not be possible without increasing the pulse durations, because the intensity in the input pulses would be too high. This results in damage to the optics, lower coupling efficiencies to the capillary, and distortions in the produced ultraviolet spectrum. This chapter describes experiments that use a high energy amplifier and dispersed pulses to produce hundred microjoule levels of ultraviolet light with efficiencies of $>20\%$ from the pump.

The overall goal of the experiments in this chapter is to find the proper pulse durations to maximize conversion efficiency to the ultraviolet from the pump. Figure 6.1 was generated using the code described in Section 4.8 to illustrate the increase in the energy of the ultraviolet pulse with longer durations. The graph illustrates that at longer pulse durations and lower pump energies where the process is away from saturation, the

curves behave similarly. In this regime the shorter duration pump generates the most ultraviolet. However, the shorter duration pulses reach saturation at a lower energy level than longer pulses, resulting in reduced levels of generated ultraviolet light. The goal is to find the correct pulse duration for a given pump energy to operate on the flat part of the curve. At higher pump energies than what is shown in Figure 6.1, back conversion of the ultraviolet light into the seed beam causes the spectrum of the generated ultraviolet light to degrade. Figure 6.1 shows that at pump input energies on the hundred microjoule level, even a 50 fs increase in the pulse duration can give a 33% increase in the output ultraviolet energy.

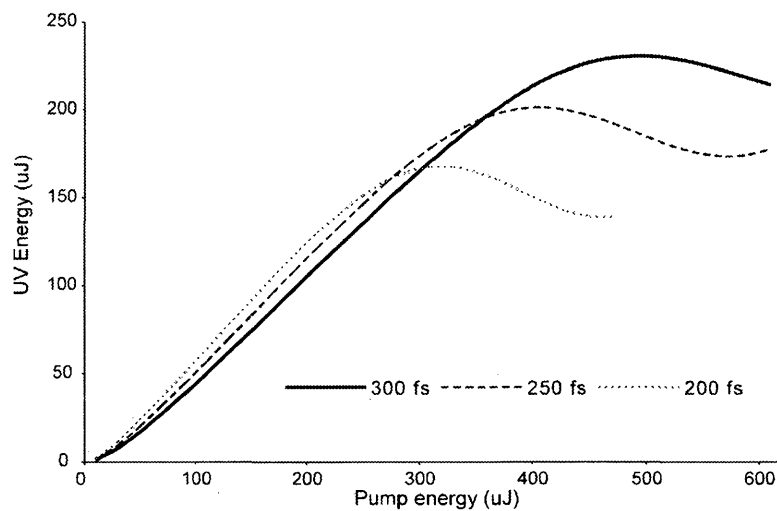


Figure 6.1 Simulated ultraviolet output versus pump energy for three different pump durations.

6.2 System Layout

The amplifier system presented in Chapter 3 produced up to 12 mJ of energy per pulse before compression. Before compression the beam was split with a 80/20% beam splitter and the low energy beam passed through 10 cm of BK7, as in Section 5.4, so that after compression there were oppositely chirped pulses. After compression the pulses have a total energy of ~ 6 mJ. Before the doubling crystal the two beams were down collimated with a negative and positive spherical mirror pair (500 mm and -300 mm). The oppositely chirped pulses were synchronized and crossed at a 5 mrad angle in a thin (0.5 mm) BBO crystal to give a blue beam with ~ 1.2 mJ of energy. This setup is roughly the same as the one presented previously in Figure 5.4, although with the increased energy it is necessary to use only reflective optics to eliminate self phase modulation and the resulting spectral degradation.

Figure 6.2 illustrates the system after the BBO crystal. The infrared seed beam for the mixing process was derived from the residual light in the positively chirped beam that passes through the blue dielectric mirror. A half-wave plate was used in the infrared beam to match the polarization of the generated blue light. The main difference between this setup and the one illustrated previously in Figure 5.5 is that a spherical mirror was used to focus the beam into the capillary instead of a lens. The intensity of the blue beam was high enough that any material in the beam resulted in self-focusing that inhibited the coupling of the beam into the lowest order capillary mode.

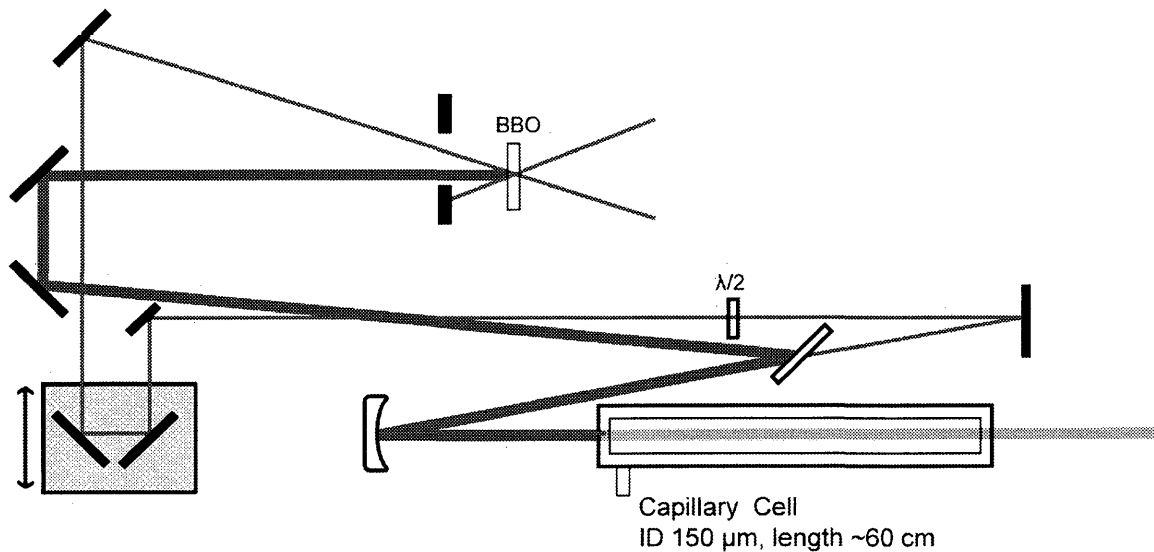


Figure 6.2 High energy OP-CPA mixing setup.

By simultaneously monitoring the ultraviolet and blue pulse energies, while varying the argon pressure, a more complete picture of the process was recorded. This data is shown in Figure 6.3. The pulse durations in this run were ~ 220 fs for the blue pump and ~ 195 fs for the infrared seed pulse. It was later found that these pulse durations were still too short, and this limited both the infrared and blue coupling efficiencies to the lowest order capillary mode. This will be explored further in the remainder of this section. However, the plot is shown here to illustrate two features that were not immediately obvious in these initial experiments. First, a large peak in the ultraviolet output is seen at the optimum pressure of ~ 60 torr, however the highest peak is at ~ 400 torr. This pressure phase matches the generated ultraviolet pulse not to the lowest order mode, but the

second order mode. This mode overlaps well with the pump and seed beams in the lowest order mode so the energy transfer is still high. The increase in yield is likely due to the presence of more atoms for interactions at the higher pressure. In the past this peak was not seen because very short (~ 20 fs) pulses were used [15]. Because of the short pulses, the group velocity walkoff between the pulses at this higher pressure was enough to reduce the temporal overlap of the three pulses. At the longer pulse durations used here, the walkoff is less than the duration of the beams. The simulations predict no difference in temporally compressing ultraviolet light generated in a higher order mode. This high order mode is analyzed in more detail in section 6.4.2.

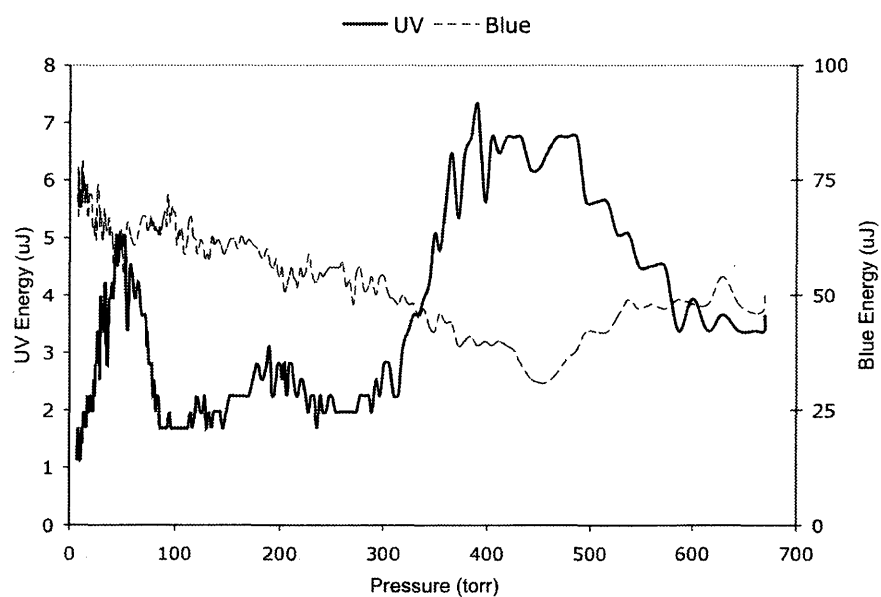


Figure 6.3 Output ultraviolet and blue energy versus pressure.

Secondly, at the large, high pressure peak the depletion of the blue is noticeable. At 450 torr the blue depletion is $\sim 28 \mu\text{J}$, corresponding to more than $18 \mu\text{J}$ of ultraviolet light produced, but the ultraviolet energy measured is only $7 \mu\text{J}$. By the conservation of energy, and the relation $1/\lambda_3 = 2/\lambda_2 - 1/\lambda_1$, the generated ultraviolet should be 75% of the depleted pump energy, not the 25% measured here. Initially, the hypothesis was that the ultraviolet light was indeed generated but was lost through guiding losses, but even at the higher order mode observed here the transmission efficiency should be $>90\%$. It was found that even at these ultraviolet energy levels the 6-mm fused silica exit windows absorb a large fraction of the ultraviolet energy through two-photon absorption. The total number of free electrons, N_q , produced by two-photon absorption in the fused silica windows is given by the relation [62],

$$N_q = \frac{\beta ALF^2}{4W_{ph}\tau_p}, \quad (6.1)$$

where $\beta = 0.045 \text{ cm/GW}$ is the two-photon coefficient for fused silica [63], A is the cross sectional area of the beam, and L is the length of the fused silica window. The fluence of the ultraviolet pulse is given by F , and W_{ph} and τ_p are the photon energy and the pulse duration respectively. For the 6-mm fused silica window used here, with a 25- μJ , 100-fs, 1-mm diameter beam $\sim 11 \mu\text{J}$ of ultraviolet energy is lost to two-photon absorption. Thus choosing the proper material for the exit window material is definitely important in the cell design. The cell exit windows were switched from fused silica to

magnesium fluoride (MgF_2), which has a negligible 266-nm, TPA coefficient. MgF_2 transmits down to 120 nm, which corresponds to a photon energy more than twice that of the 266 nm light used here. The following results will show a much better correlation between the ultraviolet energy measured at the output of the cell and the depleted pump energy after installing the MgF_2 exit window. It would also be possible to lengthen the distance from the end of the capillary to the exit window to lower the intensity, but switching to MgF_2 keeps the cell dimensions reasonable.

6.3 High Energy Ultraviolet Generation

The method used to produce the blue light is inefficient, because there are many extra optics required to split the beam and synchronize and cross the beams in the doubling crystal. With the new amplifier, more energy was available in a cleaner blue beam than the one used originally, a chirped pulse with high energy was directly doubled by a thin BBO crystal. The pulse duration was set to give ~15% conversion to the blue. This resulted in nearly millijoule levels of blue light without the distortions caused by high intensities in the crystal. It was found that at these conversion levels the generated blue beam was of similar spatial quality to light generated from the opposite chirp mixing. It was possible to achieve 40% transmission of the blue light through the 150- μm , 60-cm long capillary at moderate energy. At input energies above ~200 μJ , the efficiency fell to

~20% or less. This was likely due to intensity effects in the MgF_2 entrance windows, which degrades the quality of the focus.

To better illustrate the benefit of using longer pulses in the mixing process, the output ultraviolet energy was measured for different blue input energies. For all the following experiments, a 150- μm capillary filled with argon at a pressure of 78 torr was used. Figure 6.4 shows the results of these measurements. For these experiments, the blue and infrared pulses were characterized with an all-reflective TG-FROG setup based on the SD-FROG illustrated in Figure 5.1a. A mask was inserted in the beam to obtain the three beams necessary for the TG-FROG arrangement, and one beam was delayed to obtain a FROG trace that can be deconvolved with PG-FROG routines (setup described in Reference [64]). For the shorter 305-fs pulse, the conversion began to saturate at under 600 μJ of input pump energy. At the longer 395-fs pulses, the process did not peak until ~625 μJ . For the shorter blue pulse the infrared parameters were 400 fs duration and 130 μJ infrared through the capillary out of 980 μJ at the entrance. For the longer blue pulses the infrared duration was 660 fs with 200 μJ of infrared out of 1 mJ at the entrance. Thus, using longer pump pulses increased the efficiency of the process. By trying a range of compressor settings, the blue pulse duration of 395 fs was experimentally found to be the optimum duration for these experiments.

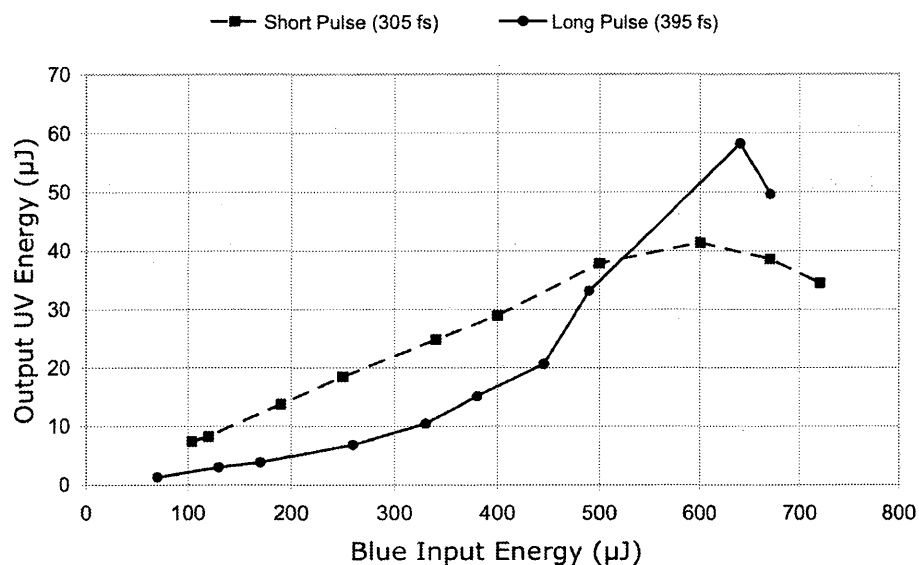


Figure 6.4 Output ultraviolet energy for different pump input energies.

A reason for the increase in output ultraviolet energy not directly related to the parametric process is that the efficiency of the transmission of the blue and infrared pulses through the capillary degrades at high intensity. Figure 6.5 shows the coupling efficiency of the blue light through the capillary at both the long and short pulse durations used above. The argon pressure in the capillary was 75 torr, which is the optimum pressure for the mixing process with these parameters. In the long pulse case the coupling efficiency remains ~38% for all blue input energies. In the short pulse case the coupling efficiency is ~40% at low blue energies, but as the energy is increased the coupling efficiency falls to ~20%. The infrared transmission was 23% for the longer pulse and only 13% for the short pulse. The reduction in transmission efficiency for both beams is

most likely due to either nonlinear effects in the input window or more likely ionization and defocus in the gas at the capillary entrance. This reduction in transmission efficiency is responsible for a large fraction of the observed overall efficiency decrease in the mixing process. It is worth noting that at the shorter pulse durations the blue beam was beginning to cause optical damage on the mirrors. Thus, it was not possible to use shorter pulses without using larger beam diameters on the optics, which is not possible while keeping the capillary cell within reasonable dimensions.

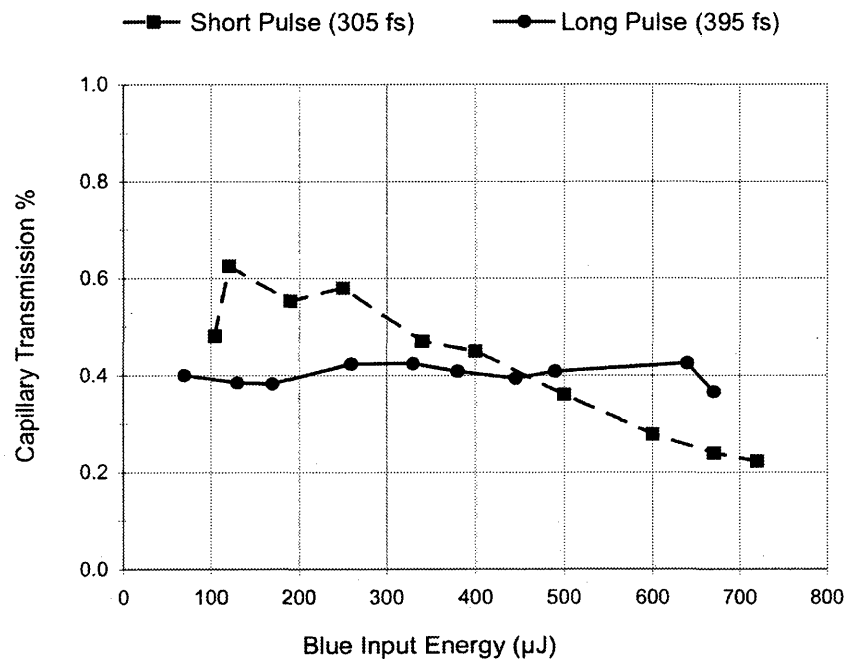


Figure 6.5 Coupling efficiency for different pump durations.

Figure 6.6 shows the recorded ultraviolet and blue energy at the exit of the cell. The ultraviolet was measured directly with an energy meter, and a portion of the blue light leaking through the first ultraviolet dielectric mirror was measured with a power meter and scaled to give an approximate energy. At the low-pressure peak of 78 torr, 60 μJ of ultraviolet light was produced, giving a conversion efficiency of 24% from the pump light. The infrared pulse parameters for this experiment were 660 fs duration, with 200 μJ of infrared out of 1 mJ at the entrance. The blue depletion at the peak was directly measured to be 31% of the 260 μJ of blue transmitted at the peak pressure of 78 torr. The blue depletion predicts that 73 μJ of ultraviolet light should be produced. This agrees reasonably well with the amount of ultraviolet light produced, which suggests that nearly all of the ultraviolet light was produced in the lowest order mode and exited the cell.

The linear slope of the transmitted blue energy versus pressure was likely due to multiphoton ionization at the entrance to the capillary. This ionization caused the beam to defocus and limited the amount of blue energy that coupled to the waveguide. It may be possible to flow the gas through the capillary to have a lower pressure at the entrance to minimize this effect.

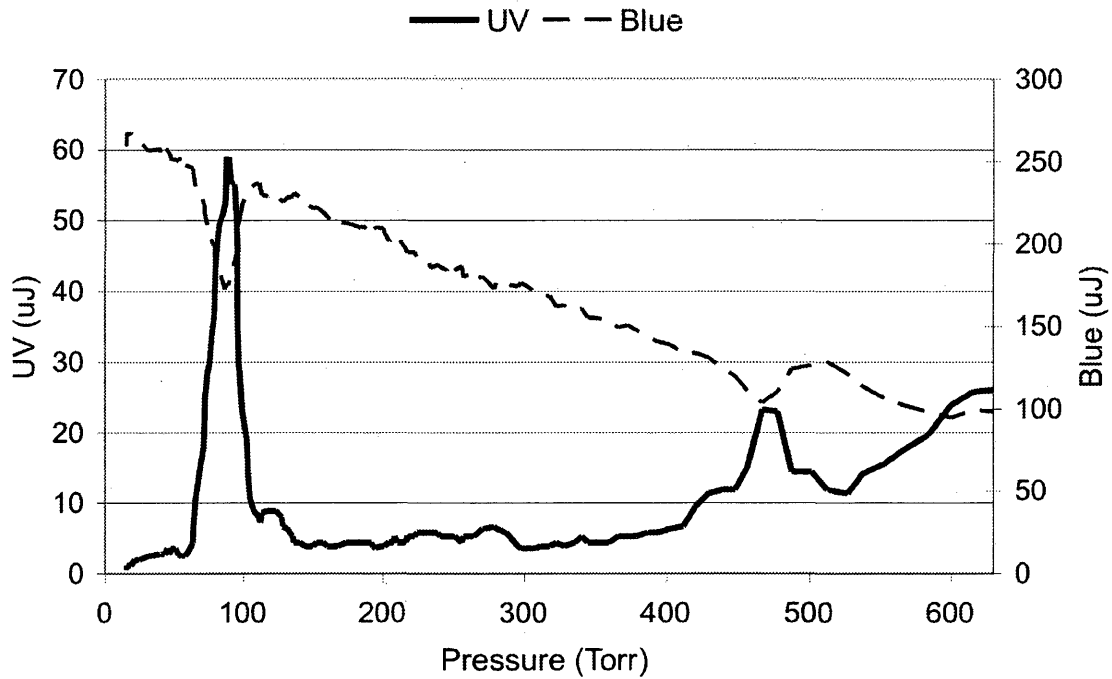


Figure 6.6 Ultraviolet and blue measured versus pressure at the exit of the cell.

6.4 Ultraviolet Beam Quality

Since the phase matching of the parametric mixing process is controlled by balancing the pressure dependence and the radial mode the ultraviolet light is generated into, there is some control over the ultimate beam quality of the ultraviolet light. In the previous demonstrations of the mixing technique with short pulses, group velocity walkoff limited the process to only the low pressure peak.

6.4.1 Lowest Order Mode

For applications where beam quality and high energy are required, it is best to run at the lowest pressure peak where the light is generated into the lowest order mode. In this mode the transmission of all the beams is maximized, and by having all the beams in the lowest order mode, the overlap between all the pulses is also maximized. Another benefit to using a lower pressure is the group velocity walkoff is minimized at the lower pressure; this maintains the temporal overlap of the pulses, increasing the efficiency of the process.

An image of the generated ultraviolet is shown in Figure 6.7a. The image was obtained by illuminating a fluorescent index card with the ultraviolet output of the capillary and imaging the surface of the card to a CCD camera. The beam was not collimated after the capillary exit and was approximately 5 cm in diameter after propagating 2 m. To ensure the card was at the source plane of the imaging system, the camera was focused so that the lines on the card were well-resolved. Then the card was flipped to the blank side, and an image recorded. The small spots in the beam profile are from imperfections in the surface of the card, and not present on the beam itself. The best fit to a lineout of the beam is shown in Figure 6.7b. It shows a good fit to the data, illustrating the high beam quality achievable with this hollow-fiber mixing technique. The small flattop on the beam is likely due to saturation on the fluorescent card and not an artifact of the beam itself.

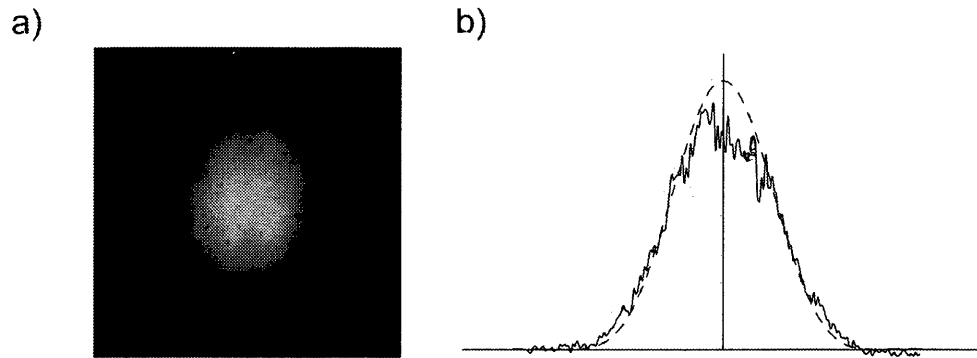


Figure 6.7 Lowest ultraviolet propagation mode and lineout with best fit.

6.4.2 Second Order Mode

To illustrate why the high pressure peak was not seen in the previous work, the relative group delays for the three pulses of interest are illustrated in Figure 6.8. Each curve represents the relative times with which the two pulses exit a 1-m capillary versus pressure. For example, at a pressure of 450 torr there is ~ 125 fs of group velocity walkoff between the infrared and ultraviolet pulse. This effectively shortens the interaction length between the three pulses. Longer pulses cause the process to be less sensitive to this walkoff.

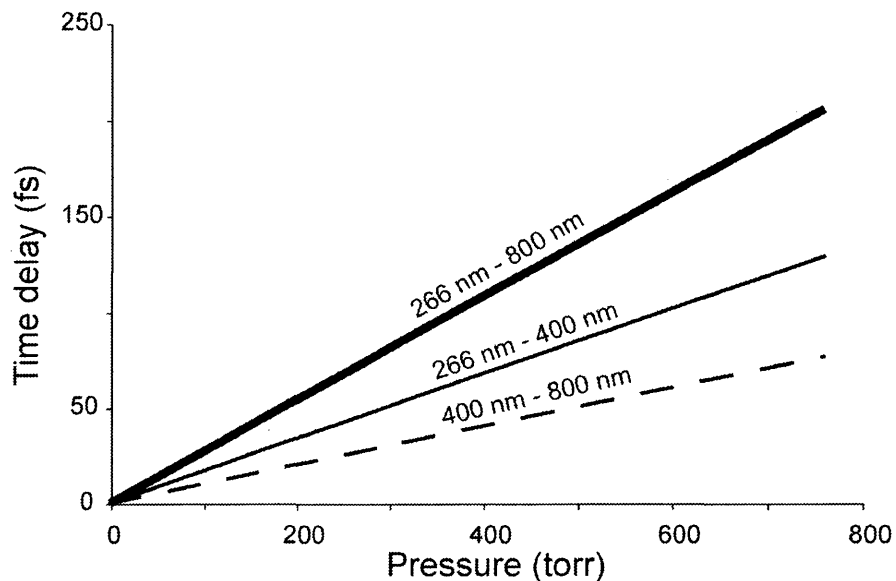


Figure 6.8 Relative group delay for pulses in the mixing process.

For some applications it may be desirable to use the higher order radial mode of the capillary. For example, in micromachining it is routine to generate feature sizes of less than 200 nm with the 800 nm light from a typical Ti:sapphire based ultrashort pulse laser [9]. Even though the ultimate focus size is limited by the wavelength of the light, only the highest intensity portion of the mode actually ablates the material. The two lowest order radial modes in the capillary are shown in Figure 6.9. The second order mode may be more beneficial for micromachining purposes, because even at 20% of the maximum intensity (dashed line) the second order mode is smaller.

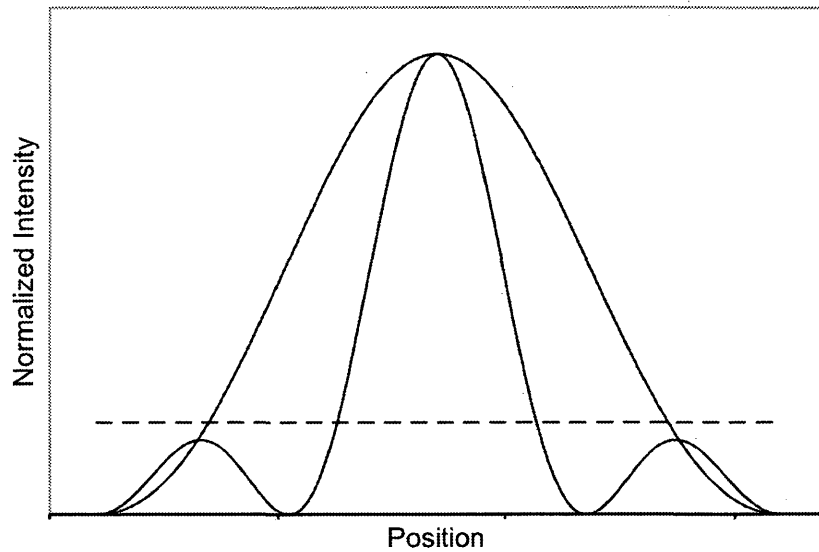


Figure 6.9 First and second order radial capillary modes.

Figure 6.10a shows an image of the far-field, second order mode of the ultraviolet light. The image was recorded in the same way as the previous image. The argon pressure in the cell was set to 390 torr, which was found to be the highest energy position for the second order radial mode. While monitoring the image of the beam, the capillary was adjusted to give the cleanest possible mode. The mode is highly dependent on the coupling parameters, but the mode is stable once it is optimized. Figure 6.10b shows a fit to the near-field profile of the second order capillary mode. The far-field mode is obtained by taking the Fourier transform of the near-field mode (Figure 6.9). The mode at the image plane is a donut-mode with an equal intensity spot in the middle. To recover

the mode illustrated in Figure 6.9, an image of the capillary exit would have to be carefully made, taking care to capture all the light from the exit of the capillary.

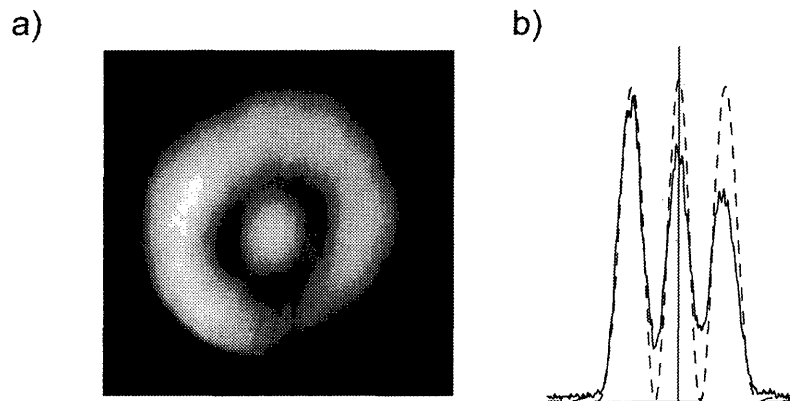


Figure 6.10 Higher capillary mode image and lineout with best fit.

6.5 Spectral and Temporal Characteristics

The measured spectra for the input and output pulses are shown in Figure 6.11. The input infrared seed (Figure 6.11a) and the blue pump light spectra (Figure 6.11b) were estimated and used with the measured pulse durations to simulate the production of the ultraviolet signal light. The spectra of the simulated (dashed) and measured (solid) ultraviolet light are shown in Figure 6.11c. The measured FWHM of the ultraviolet spectrum is 1.1 nm, centered at 265 nm. The value of 265 nm agrees well with the predicted spectra for the values of the fundamental and doubled pulses

$$\left(\frac{2}{398} - \frac{1}{800} = \frac{1}{265}\right).$$

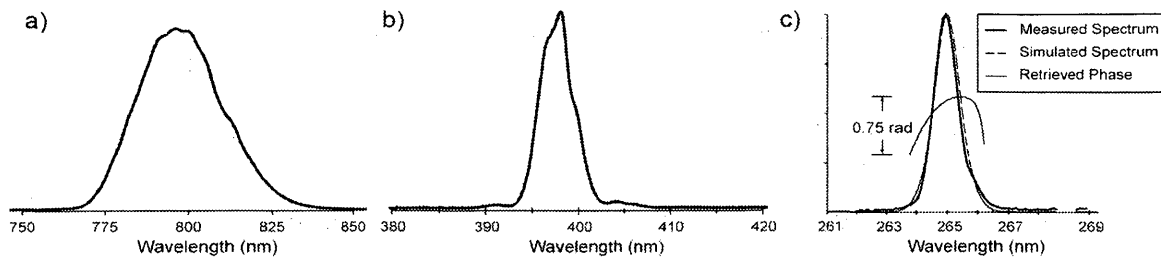


Figure 6.11 Spectra of seed (a), pump (b), and produced ultraviolet (c) with simulated spectra (dashed).

Figure 6.12a shows the simulated output temporal profiles of the output infrared seed (dashed), blue pump, (thin) and ultraviolet (thick) pulses. The simulations predict that at the measured pulse durations and energies of the input pulses, there is 150 μJ of generated ultraviolet and 72% depletion of the blue pump pulse. The modulation in the blue profile is due to back-conversion from the generated ultraviolet, and was not seen in the experiments. While these levels of depletion were not seen in the experiments, it does show that with these input parameters the process is operating near saturation.

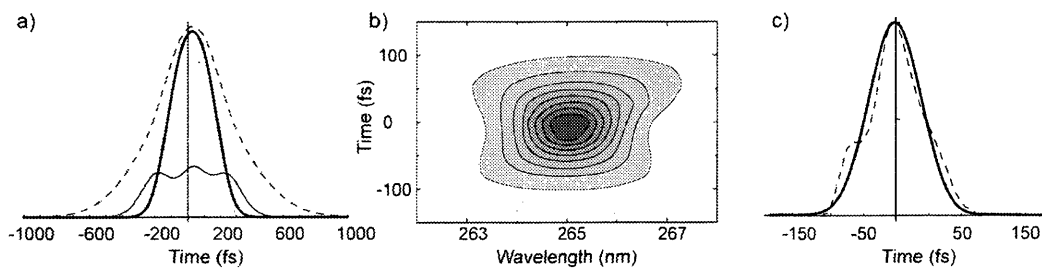


Figure 6.12 a) Simulated output seed (dashed), pump (thin) and signal (thick) pulses. b) Retrieved PG-FROG trace for shortest output pulse. c) Compressed ultraviolet output (dashed) and simulated transform-limited pulse (solid).

The ultraviolet pulse from the output of the cell was compressed with 5 mm of fused silica and 3.5 m of air before being measured with an all-reflective TG-FROG as in section 6.3. The retrieved compressed ultraviolet PG-FROG trace is shown in Figure 6.12b. The contour lines are at 2%, 5%, 10%, 20%, 30%, 40%, 50%, 60%, 70%, and 80% of the maximum value. The compressed output ultraviolet temporal profile is shown in Figure 6.12c. The simulated, uncompressed output is shown by the thin, solid line, and the simulated Fourier transform limit is shown by the thicker solid line. The retrieved, compressed pulse duration was 82 fs and shows good agreement with the simulated transform limit (Figure 6.12c). The phase across the bandwidth is shown in Figure 6.11c (thin, solid line) and shows the pulse is compressed to within less than 1 radian of phase.

6.6 Improving Spectral Width

Since both the input seed and pump pulses were negatively chirped using the same grating compressor, the frequency-doubled pump pulse will be shorter than the fundamental. This does not affect the energy output of the mixing process but does limit the spectrum of the produced ultraviolet light. Since the infrared seed pulse is chirped, the different wavelengths in the pulse are spread throughout the entire pulse duration. Since the pump pulse is shorter than the seed pulse, it selects a subset of the frequencies in the seed pulse. This was the main factor that limited the pulse durations in these experiments.

To further increase the spectral width of the ultraviolet, the chirps of the input pulses can be chosen to take advantage of the frequency spread in chirped pulses. Figure 6.13 illustrates the benefit of choosing the relative sign of the dispersion of the seed and pump pulse. At each point in time, the ultraviolet light is computed by using the relation

$$\omega_{uv} = 2\omega_{blue} - \omega_{ir}.$$

Figure 6.13a shows the case of mixing with both the seed (thin) and pump (dashed) positively chirped. In this case the generated ultraviolet has the same range of photon energies (frequencies) in the pulse. Figure 6.13b illustrates the effect of mixing a positively chirped pump pulse with a negatively chirped seed beam. In this case the generated ultraviolet is still positively chirped, but the pulse consists of a larger range of frequencies. Thus, the spectrum of the pulse is broadened. The range of chirps in the plots is exaggerated to better illustrate the process. Note that if all the chirps are reversed the spectral broadening effect is still the same. However, to achieve opposite chirps would require two separate grating compressors, which adds considerably to the cost and complexity of the system, and is not necessary from an energy perspective.

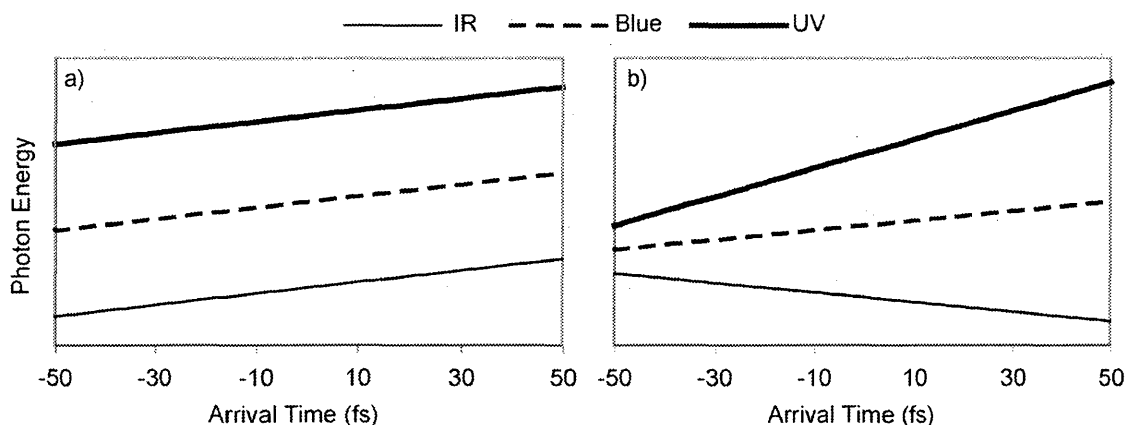


Figure 6.13 a) Mixing with same (positively) chirped pulses. b) Mixing with oppositely chirped pulses.

6.7 Summary

This chapter reported using chirped input pulses with the hollow-fiber parametric mixing setup described in earlier chapters to increase the ultimate yield in the process. With high energy beams, all-reflective optics must be used to minimize non-linear effects that inhibit the coupling of the pump and seed beams into the capillary. It was shown that to keep the cell within reasonable dimensions, both the entrance and exit windows should be MgF_2 to minimize nonlinear effects and to increase the output ultraviolet energy by minimizing two-photon absorption of the ultraviolet light by fused silica windows.

Chirped pulses are required to generate ultraviolet pulses with energies greater than $\sim 10 \mu\text{J}$. Chirped pulses were used to generate ultraviolet pulses with $60 \mu\text{J}$ of energy with conversion efficiencies of 24% from the pump. These values are the highest reported to date. The ultraviolet pulses were compressed to near-transform limited 82 fs pulses.

The beam quality of the generated ultraviolet is excellent, because it is generated in the lowest order capillary mode. A side effect of using longer pulses is that the parametric mixing process is less sensitive to group velocity walkoff. This allows generating substantial amounts of ultraviolet light in the second order, radial capillary mode. This may have benefits in nonlinear processes such as micromachining, because the middle of the mode is actually smaller than the lowest order mode.

The chirped input pulses were generated from a single grating compressor, which simplifies the system but limits the spectrum of the output ultraviolet light. By adding a second grating compressor to independently control the duration of the seed and pump pulses, the spectral width of the ultraviolet could be increased, allowing compression to the 30 fs level.

CHAPTER 7 ULTRAVIOLET X-RAY GENERATION

7.1 Introduction

The construction of an ultrafast x-ray source has important applications for ultrafast x-ray diffraction measurements, which can study the fastest elementary steps of chemical reactions and aid in the understanding of basic dynamics in physics, chemistry, materials science and biology. A laser-based x-ray source allows the studying of these processes through x-ray diffraction with high temporal and spatial resolution [11]. Absorption experiments through extended x-ray absorption fine structure (EXAFS) [65] have recently been studied with ultrafast laser-based x-ray sources [66]. For these experiments there is still a drive for an increased x-ray yield and smaller x-ray source sizes.

A high temperature plasma is created when a very intense ($\sim 10^{17}$ W/cm) laser pulse is focused onto the surface of a solid. The energy is absorbed in a thin layer of material (on the order of the skin depth), which is heated, melted, and vaporized, thus generating an expanding plasma above the surface. At laser pulse durations greater than about 10 ps, the timescale of this expansion is shorter than the duration of the laser pulse, and plasma hydrodynamic effects become important. A gradient in plasma density develops, and the laser energy can be absorbed by this plasma until it reaches the critical surface where the laser frequency equals the plasma frequency. At this point the pulse is then reflected.

These laser-produced plasmas are good radiators and produce both visible and x-ray photons due to line transitions, radiative recombination, and bremsstrahlung radiation [30].

Plasmas produced by short, subpicosecond pulses exhibit different properties than plasmas produced by longer pulses. For a laser pulse of about 100 fs there is little hydrodynamic expansion of the plasma during the absorption time of the laser energy. Under these conditions, the laser energy is absorbed in the high-density solid target material instead of the lower density plasma plume as in the long pulse case. The near solid density of the plasma is responsible for the production of x-rays with timescales comparable to that of the laser pulse, because of the higher collision frequency in the high density plasma. Typically, ultrafast x-ray plasma generation has been studied with the fundamental 800 nm light from a Ti:sapphire laser system. The energetic ultraviolet pulse system described in Chapter 6 opens the door to studying this process with ultraviolet light.

There are several advantages to using ultraviolet light to create the plasma. First, the optimal intensity for x-ray generation from plasmas is $\sim 10^{17}$ W/cm². At higher intensities the x-rays are generated over a larger energy range, and the higher energy x-rays are generally not desired [67] [68]. It has also been shown that the ideal intensity for copper k- α generation is $\sim 6 \times 10^{16}$ W/cm² [68]. At higher intensities the generated x-rays are driven deeper into the target and absorbed and remitted over a larger time scale. Thus, to generate x-rays with durations comparable to the laser pulse, the intensity on target

should be $\sim 10^{17}$, but not higher. Since these intensities can now be achieved with a single stage of amplification and the optical parametric chirped pulse amplification system presented in Chapter 6, there is not much added complexity to the system.

Since the heated-electron temperature scales with the ponderomotive potential scales on the order of $(I\lambda^2)^{1/3}$, shorter wavelength light will require a higher intensity. Because the ultraviolet energy focuses to a smaller spot than the fundamental infrared light, the energy requirements will be about the same. Thus given a desired x-ray yield, with a given pulse energy, the ultraviolet light will generate the x-rays with a smaller source size.

The ultraviolet light is generated by a third-order process and the contrast between the main pulse and any prepulses or prelasing in the system is reduced by approximately three orders of magnitude. It has been shown that any prepulses or prelasing can increase the total yield of x-rays, but at the expense of the duration of the x-ray pulse [12, 31]. Clean pulses can be used to study the x-ray absorption process in greater detail by using a known prepulse, or they can be used directly to generate the shortest duration x-rays possible. By preshaping the input infrared seed pulse in the hollow fiber mixing process, it is possible to control the pulse shape of the ultraviolet pulses. This would allow experiments studying the change in the x-ray parameters with different input pulse shapes.

Because of the wavelength dependence of the spot size in the focus, by using ultraviolet light, more of the energy can be directed to a smaller area. Since the ultraviolet light is generated in the lowest order capillary mode, the smallest possible focus can be achieved on target. Having the x-rays generated from a smaller spot gives the resulting x-rays more spatial coherence, thus they can produce higher resolution x-ray images.

7.2 X-Ray Cell Design Considerations

The x-ray cell used in the experiments is illustrated in Figure 7.1. The cell consists of a small (~1' square) vacuum chamber built around a breadboard. The beam enters through a large 2" fused silica entrance window. In this case fused silica is acceptable as the window material because the intensity is reduced as the result of a larger beam size.

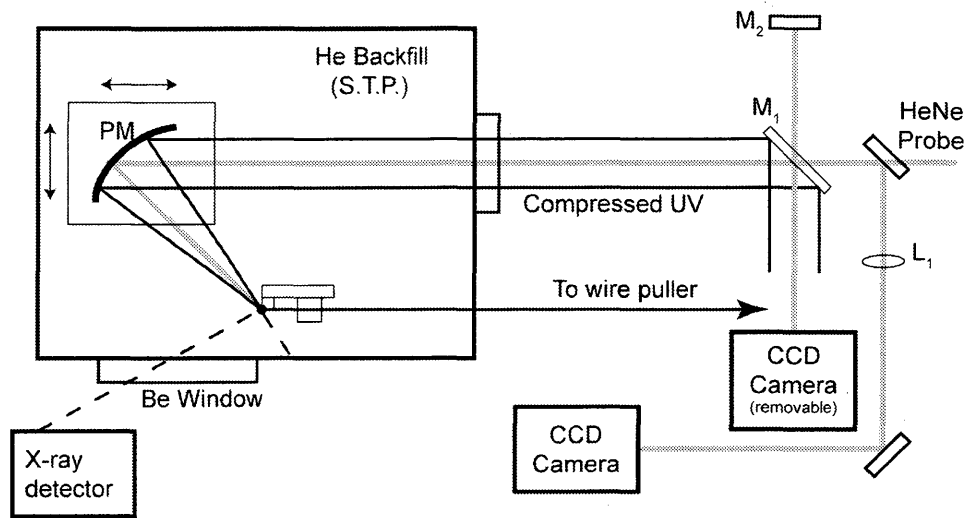


Figure 7.1 X-ray cell schematic.

7.2.1 Focusing Considerations

A large entrance beam also gives the smallest beam in the focus by decreasing the f -number of the focusing system. To achieve the smallest possible focus size, an off-axis parabolic mirror is used to focus the laser beam instead of a lens or spherical mirror, because a properly aligned parabola will focus a beam with no aberrations. To illustrate the need for using a parabola for focusing the beam, the ratio of the geometric spot size to the Gaussian limit for the spot size versus f -number is shown in Figure 7.2. When the geometric spot size is larger than the Gaussian spot size, the spot size is limited by the aberrations in the focusing optic. At small f -numbers a spherical mirror focuses the beam better than a lens, but if the mirror is tilted even as little as 2° , the plano-convex lens gives a smaller spot size. For a properly manufactured and aligned parabolic reflector the

geometric spot size is exactly zero. There are four degrees of freedom for aligning a parabola. The two angle adjustments are necessary to focus the beam with no aberrations, and the mirror can be translated in two dimensions to place the focus on the target. The parabolic mirror is mounted in a standard optical mount for angular adjustment and on a translation stage to position the focus. The stage and mirror adjustments are New Focus Picomotor piezoelectric adjusters, which allow adjustment from outside the sealed cell.

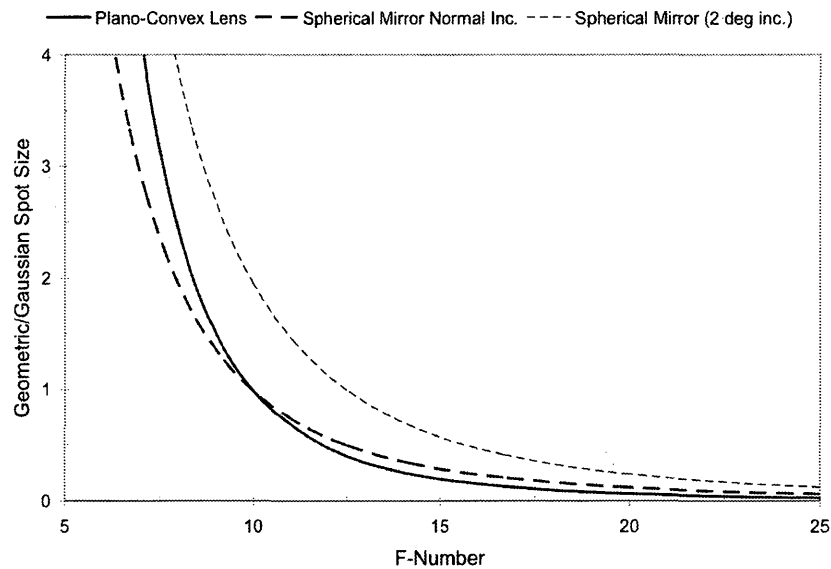


Figure 7.2 Focus quality for a plano-convex lens and a spherical mirror at different angles of incidence.

7.2.2 Debris Control

A problem with all laser pulse based x-ray systems is that the high intensity of the beam causes ionization of the air before the beam reaches the target. This results in energy loss in the beam directly due to the ionization, and the ionization causes the beam to defocus reducing the intensity on the target. Finally, nitrogen strongly attenuates the generated x-rays.

One approach is to evacuate the cell to minimize these negative effects. However, without a gas backfill the debris from the target will travel farther and deposit on the inside of the cell. This deposited copper coating reduces the effectiveness of the focusing optics and the beryllium window. One method to minimize the debris deposition on the optics at low pressure is to install a mylar film between the target and the focusing optic [11]. This film must be cycled at low speed because of the debris buildup. The thin film is very fragile, and if it breaks the optics will quickly become damaged. While this technique has been used successfully at longer wavelengths, there are several difficulties in implementing it for ultraviolet beams. Most materials strongly absorb in the ultraviolet region of the spectrum, making this approach difficult to implement. There are a few materials such as Teflon AF and Honeywell Aclar that are transparent in the ultraviolet region of the spectrum. However, they are very expensive and not readily available in the form required for a disposable shield. Because of the short focal lengths required to achieve the proper intensity on target with a low energy beam, the light would have to

take two passes through the film resulting in more losses. These losses are not desirable for the relatively low energy ultraviolet beam. The mylar film can still be used to protect the beryllium window and other things not in the beam path.

Another technique used to protect the optics in the x-ray cell is to fill the x-ray cell with helium at atmospheric pressure. Helium has a higher threshold for ionization, thus less energy is lost before the target. Also the smaller ionization area in the gas results in less defocus before the target. The helium atmosphere provides enough resistance to the debris particles so they do not reach the optics. Helium gas at atmospheric pressure has a very high transmission for the generated x-rays (>99%). This technique has successfully been used at similar intensities and at a 2-kHz repetition rate [12, 31, 67], so it is more than adequate at the low 10 Hz repetition rate used in this system. Furthermore, using a gas at atmospheric pressure greatly simplifies construction of the x-ray cell. At higher repetition rates, the helium in the cell must be filtered in the area of the target to remove the metal debris. Typically the air is also flowed across the target to immediately sweep the debris from the area of the optics. In the cell used here a small fan is used to help blow the debris away from the parabolic mirror. This seems to be sufficient at the low repetition rate used here.

7.2.3 Alignment Issues

To aid in initial alignment and provide continuous diagnostics, a HeNe laser is used to both set up an interferometer and image the focus on the wire. The ultraviolet dielectric mirror, M_1 , is used as a beamsplitter for the HeNe light. For rough alignment the target is replaced with a flat mirror, and the interferogram on the CCD camera is used to align the parabolic mirror by removing all curvature from the fringes. With the input beam normal to the parabolic mirror, the target is reinserted in the cell and the parabolic mirror is translated to put the focus on the surface of the target.

Since the target is at the focus of the parabolic mirror, it projects an image at infinity. By using a second long focal length lens after the ultraviolet mirror, M_1 , the focal spot can be imaged onto a CCD camera with a magnification equal to the ratio of the focal lengths of the parabolic mirror and the imaging lens. This arrangement allows the monitoring of the wire position because the spot size will change if the wire moves in the focal plane. The movement of the target can be characterized by measuring the movement required to put the image back in focus. This imaging system is extremely sensitive to the input angle of the beam because the parabolic mirror is only optimized for a normal incident beam. Although the interferometer is useful when learning how to align the parabola, fine-tuning the alignment is more easily achieved by using the imaging system alone. This is accomplished by aligning the angle of the parabolic mirror such that the beam stays round when the mirror is translated through the focus. The magnification

—of the imaging optics was calibrated by using a 675 groove/mm grating as a mirror at the target position. The grooves could be measured at the image plane on the CCD camera and the magnification was found to be ~ 77 with a 2000 mm lens used as the imaging optic with a 25.4 mm focal length parabolic mirror.

7.2.4 Target Stability

The target used in this experiment is 0.5-mm, 99% pure copper wire. The wire enters and exits the cell through two ~ 20 -cm long, steel capillary tubes (McMaster-Carr #5560K59) with an inside diameter only 30-50 μm larger than the wire diameter. This is a tight enough fit to the wire so that the cell maintains a pure helium environment for hours at a time. This wire target technique is currently in use and reported to achieve maintenance free operation for more than 100 continuous hours [11, 69].

Current wire guide designs are typically used with high energy, longer wavelength lasers, and thus the focusing conditions are relaxed. These systems typically have a focus size in the tens of microns [11, 12, 31]. One goal of using shorter wavelength pulses is to reduce the source size of the x-rays. Because the Rayleigh range of a 266-nm, 1- μm spot size is only ~ 10 μm , the wire needs to be stable to within that range or better. Current wire guide designs are only stable to within tens of micrometers and tend to jump randomly with movements of up to 100 μm [11, 70]. These movements were observed with the imaging system and a new wire guide was designed with higher stability.

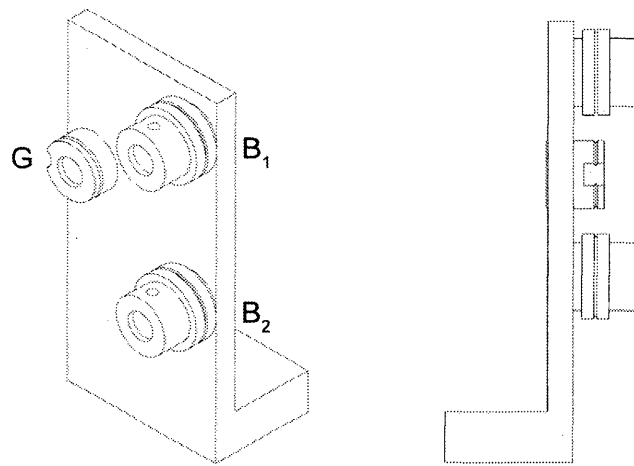


Figure 7.3 X-ray wire target guide design.

The new wire guide design is illustrated in Figure 7.3. The upright is 3/16" thick aluminum with a bracket for clamping it in the cell at the proper position. The wire enters over a grooved shielded bearing, B_1 . The guide, G, is a custom made assembly that consists of a 1/2" stainless steel rod with a 60° groove milled ~0.025" deep. This allows approximately half of the copper wire to sit in the groove. To allow unhindered access to the wire, a ~1 cm relief was cut perpendicularly to the wire groove in the region of the focus. This wire guide is mounted to the upright and not allowed to rotate. The wire then travels around another shielded bearing, B_2 and out of the cell. Both bearings are installed on hardened steel shafts held into the upright by a setscrew. A nylon washer next to the upright and a steel collet on the other side allow the bearings to rotate freely on the shaft. This setup was monitored over the course of a day of use, and the wire seldom moved more than 5 μm around the focus. No large jumps were noticed and if they occurred the

wire always returned to the optimum position. To achieve stable operation the wire was routed around large (~2") precision v-groove pulleys between the cell and both the wire source spool and the wire pickup reel mounted on an electric motor. The wire was kept at as high a tension as possible to seat properly in the grooves on the target guide.

The wire remained stable up to the maximum velocity of the motor used in this cell (~10 mm/s). This velocity was enough to run at repetition rates of up to 2 kHz or more. This wire guide is at least twice as stable and much more simple to construct than the currently published designs [11, 70]. This stability is critical to using short focal length focusing optics to achieve the smallest possible x-ray source size.

7.3 Results

To provide a basis for comparison and to check the operation of the cell, 1.2 mJ of blue light was used to generate the x-rays. The duration of the pulses used in the initial experiment was ~150 fs. The parabolic mirror used in this experiment was a 25.4 mm focal length (1" diameter), with $\lambda/4$ surface quality (Janis Optics). With the parabolic mirror aligned with the HeNe laser, the blue light was aligned to the HeNe laser. The cell was then evacuated and filled to atmospheric pressure with helium gas.

A Geiger counter was placed near the beryllium window and used to monitor the emitted x-ray flux as the parabolic mirror was translated to focus the beam on the surface of the wire target. When the x-ray flux was maximized, an x-ray CCD camera was used

to capture a spectrum of the generated x-rays. The signal on each CCD pixel is proportional to the x-ray photon energy. Each photon was tabulated and plotted in a histogram to show the spectrum of the emitted x-rays. The total x-ray flux was calculated by assuming the x-rays are emitted equally over the entire sphere around the plasma.

Figure 7.4 shows the x-ray spectra generated with the blue light. There is a background of brehmstrahlung radiation generated from the low energy electrons in the plasma. This radiation is useful for x-ray absorption spectroscopy experiments. The copper $k\alpha$ line radiation is visible at 8 keV. There is very little radiation generated above this line, which makes this a clean source of copper $k\alpha$ line radiation. The flux is divided by 2000 shots for comparison with current sources in the kilohertz regime.

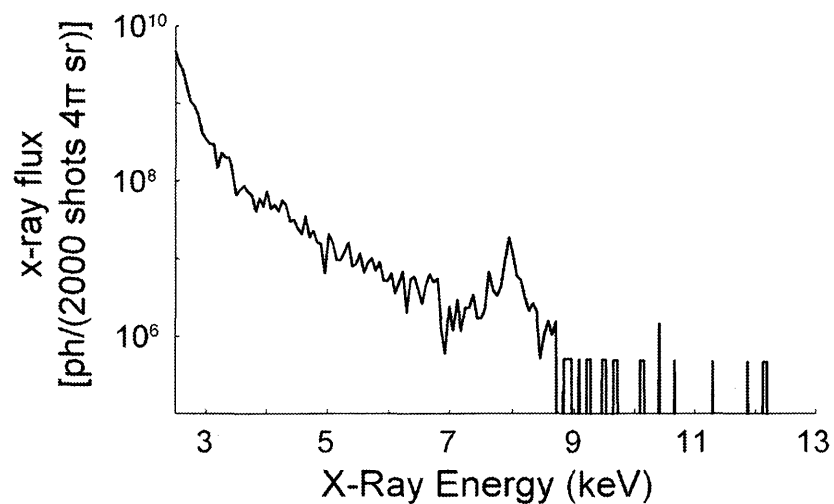


Figure 7.4 Initial x-ray spectra generated with blue light.

Unfortunately the CCD camera used in this experiment has a lower resolution than those used in other experiments. The camera can only be stably cooled to -10°C so the background quickly reaches levels where it will broaden the appearance of the line radiation. To counteract this, hundreds of short, two second, exposures were taken and binned and then the histograms were summed to produce a histogram of the total measured x-ray flux. Figure 7.4 was corrected for the attenuation of the x-ray flux from the helium, air, mylar, and beryllium in the path of the x-rays. The nitrogen in the air is the biggest attenuator of the x-rays in this energy region.

If the cell is operated with air instead of a helium backfill the generated x-ray flux is reduced by a factor of at least 10. This is due to a combination of energy loss to the ionization of the nitrogen, the defocus of the beam in the nitrogen plasma, and the absorption of the generated x-rays by the air. The defocus of the beam in the air-plasma before the target is most likely responsible for the largest loss. Without the wire present in the holder, no x-rays in the keV range are detected. This indicates the wire guide does not affect the x-ray generation process.

These results provide the data which can be used to estimate the energy requirements to generate x-rays with ultraviolet pulses. The blue spot on the wire was imaged with the calibrated imaging system described in Section 7.2.3 and the best focus was found to be $5.28\ \mu\text{m (H)} \times 3.06\ \mu\text{m (V)}$. Using this value, the measured value of 0.9 mJ of blue energy, and a measured 130 fs pulse duration, the intensity on target was found to be

1.3×10^{16} W/cm². This agrees well with the published values for observing copper k- α lines [12, 31]. The ultraviolet pulses should be able to be focused twice as well as the blue pulses, both because of the wavelength scaling and the fact that the ultraviolet light is generated in the lowest order capillary mode which should allow near transform limited focusing. Assuming this and being able to compress the ultraviolet light to 30 fs, the energy required for x-ray generation with ultraviolet pulse is ~ 200 μ J. This would give an intensity on target of 5×10^{16} W/cm². This assumes lossless compression, which may not be feasible. This is not out of the question with the current hollow fiber mixing setup. However, the pulse dispersions would need to be more carefully controlled with the addition of a second grating pair on the input pulses, to allow compression to the 30 fs level.

7.4 Summary

As of yet the energy in the ultraviolet pulse generated from the ultraviolet OP-CPA experiment is not high enough to be used to generate x-rays. However, this cell will provide a simple testing ground for x-ray generation for moderate energy beams. Using a helium backfill at atmospheric pressure eliminates the need for masking of the optics with protective films. This minimizes the reflective losses, and also the absorption issues with ultraviolet pulses. The ultrastable wire guide maintains the wire stability on the micrometer level, an order of magnitude greater than the stability of currently published

wire targets. The stability of the target is important for moderate energy beams that must be focused with short focal length optics to reach the intensities needed for x-ray generation.

CHAPTER 8 SUMMARY AND CONCLUSIONS

8.1 High Energy, Double Confocal Multipass Amplifier

One of the major accomplishments presented in this thesis is the single-stage, compact Ti:sapphire based amplifier described in Chapter 3. The amplifier is capable of generating pulses with 10 mJ of energy (compressed to 7 mJ) at a 10 Hz repetition rate. The amplifier has a unique four mirror multipass design with good contrast, beam quality, and stability. The amplifier uses a new concept of taking a set of passes with a focused beam in the gain medium to maximize the single pass gain. The beam is then extracted and the prelasers reduced. Then the beam is reinjected into the same amplifier with a collimated beam in the gain medium to maximize the energy extraction. This was not possible with previously used amplifier designs because the layout of the rings was such that the beam would be focused on the surface of a coated optic, causing damage.

This amplifier design is directly applicable to higher repetition rate systems, with the addition of some cooling capability on the crystal. The high energy and temporal contrast makes this amplifier system directly useful for x-ray generation and other applications requiring temporally clean pulses. The excellent beam quality is ideally suited for coupling to the hollow waveguides used in the other experiments presented in this work.

The amplifier currently has the highest published energy output from a single stage of amplification.

8.2 Ultraviolet Parametric Mixing in Hollow Fibers

Hollow fiber mixing offers several advantages over parametric mixing in crystals: longer interaction length without group velocity walkoff and the ability to be scaled to much shorter wavelengths without the absorption issues present in mixing processes in solid media. By using parametric mixing ($3\omega = 2 \cdot 2\omega - \omega$) instead of direct mixing (3ω), the ultraviolet light can be phase matched and generated in the lowest order capillary mode, providing excellent mixing efficiency and beam quality. By using different pump light or replacing the seed pulse with light from a conventional optical parametric amplifier, tunable light throughout the ultraviolet spectrum can be generated.

8.2.1 Low Energy Ultraviolet Generation

The initial experiments with hollow fiber parametric amplification presented in Chapter 5 demonstrate higher energy output in the hollow fiber frequency conversion process by using longer duration, higher energy input pulses. These experiments were performed with the initial, low energy, multipass amplifier presented in Chapter 2. The results suggest that even at low energy there is benefit to using chirped pulses in the

mixing process. It is probable that in the initial demonstrations of this technique, chirped pulses were used. In the previous publications the pulse durations were not carefully controlled and monitored; only the shortest achievable duration of the Ti:sapphire laser system was documented. The results conclusively show that chirped pulses will definitely be required to scale the ultraviolet mixing output to the hundred microjoule level or more.

Chapter 5 also presented the application of mixing oppositely chirped pulses in a BBO crystal to generate narrow-band blue light. Mixing the oppositely chirped infrared pulses in the doubling crystal generates the blue light efficiently while maintaining moderate intensity in the crystal. The reduction of intensity in the doubling crystal preserves the spatial beam quality. This method applied a technique previously used in the nanosecond regime, to shorter (~ 1 ps) pulses. Because the chirps were modest, a novel way of generating the oppositely chirped pulses with material and a single grating compressor was used.

8.2.2 High Energy Ultraviolet Generation

By using the newly developed high-energy amplifier presented in Chapter 4, the overall goal is to scale the energy of the mixing process by the same factor as the improvement in the amplifier. By dispersing the input pulses to ~ 500 fs duration, the intensity of the guided beams were held at the optimum value. Ultraviolet pulses with $60 \mu\text{J}$ of energy were produced, with conversion efficiencies of 24% from the pump. Both

the overall ultraviolet energy and the conversion efficiency are the highest reported to date. The ultraviolet pulses were compressed to near-transform limited 82 fs pulses. The beam quality of the generated ultraviolet is excellent, because it is generated in the lowest order capillary mode.

A side effect of using longer pulses is that the parametric mixing process is less sensitive to group velocity walkoff. This generates substantial amounts of ultraviolet light in the second order, radial capillary mode. This may have benefits in nonlinear processes such as micromachining, because the middle of the mode is actually smaller than the lowest order mode. With careful focusing this may reduce the achievable feature size in micromachining because a smaller region would be above the ablation threshold.

The chirped input pulses were generated from a single grating compressor, which simplifies the system but limits the spectrum of the output ultraviolet light. By adding a second grating compressor to independently control the duration of the seed and pump pulses, the spectral width of the ultraviolet could be increased, allowing compression to the 30 fs level.

8.3 X-ray Cell Construction

As of yet the energy in the ultraviolet pulse generated from the ultraviolet OP-CPA experiment is not high enough to be used to generate x-rays, this cell will provide a simple testing ground for x-ray generation for moderate energy beams. Special

consideration has to be given to creating a cell to provide a testing ground for x-ray generation with moderate energy beams. Chapter 7 detailed the construction and testing of an x-ray cell constructed specifically for use with moderate energy beams. The cell used a helium backfill at atmospheric pressure to eliminate the need for masking the optics with protective films. This minimizes the reflective losses, and also the absorption issues with ultraviolet pulses.

A new wire guide was developed that maintains the wire stability on the micrometer level, an order of magnitude greater than the stability of currently published wire targets. The stability of the target is important for moderate energy beams that must be focused with short focal length optics to reach the intensities needed for x-ray generation.

8.4 Directions for Future Exploration

While the work presented in this thesis describes both a complete high energy amplifier system and an energetic ultraviolet source, there are avenues for further exploration and applications to different systems.

8.4.1 Double Confocal, Multipass Amplifier

Because the amplifier system described in Chapter 3 used a compact configuration, some intracavity corrective optics were needed to correct the aberrations that arise from

the short cavity configuration. By increasing the cavity length, simulations predict that the correction optics would not be necessary. This would result in a more simple cavity configuration, with less material than the current design. This would give a small improvement in the pulse duration, because the intracavity material currently limits the compression to ~ 30 fs. A long cavity version of the amplifier was used shortly in another system in the lab, and preliminary results showed the correction optics were not necessary. It may also be possible to use custom optics in the current short cavity configuration to reduce or eliminate the current corrective optics.

The amplifier was designed specifically for 10 Hz operation, so thermal lensing effects were not considered. At the pump levels required to produce ~ 10 mJ pulses, the thermal lens in the Ti:sapphire crystal will be short enough to disrupt the cavity stability. Since the beam is collimated in the last set of passes, it is very sensitive to thermal lensing effects in the crystal. However, because the Ti:sapphire crystal is pumped from both sides, heat removal from the system should be more efficient. With the addition of a heat removal mechanism on the crystal, the amplifier would be directly usable with higher repetition rate systems.

8.4.2 Hollow Fiber, Chirped Pulse Optical Parametric Mixing

The main focus of this thesis was to demonstrate an increase in the ultraviolet yield by using longer duration pulses in the hollow fiber mixing process. A single grating compressor was used to generate both the seed and pump pulse without the expense of a second grating compressor. This resulted in the infrared seed pulse having a longer duration than the pump pulse, so the resultant ultraviolet spectrum was narrowed slightly. This limited the recompression to the ~ 80 fs level. By using a second grating compressor, the chirp of both the seed and pump pulse can be more precisely controlled over a larger range. This would not increase the energy yield of the generated ultraviolet, but it would give a broader ultraviolet spectrum. This should improve the compressed ultraviolet duration by a factor of two or more.

It is possible to scale the hollow fiber mixing process to even shorter wavelengths. By replacing the 800 nm seed light with tunable light from a conventional crystal-based, optical parametric amplifier, tunable output in the ultraviolet could be produced. As an ultimate test of the chirped pulse mixing process, narrowband 266 nm light directly from a frequency tripled Nd:YAG or Nd:YLF laser could be used as the two-photon pump pulse. This would provide millijoule levels of ultraviolet light at ~ 10 ns duration. Then the uncompressed infrared light directly from a Ti:sapphire chirped pulse amplifier could be used as the seed. Even with a moderate energy amplifier, this would give a very large seed energy, because 100% amplifier output could be used for the seed pulse. This would

generate intense extreme ultraviolet light at ~ 160 nm through the same parametric mixing process described in this thesis. With proper compression the ultraviolet light should be compressible to the same order of the light from the Ti:sapphire oscillator.

8.4.3 Towards X-Ray Generation with Ultraviolet Light

The constructed x-ray cell is useful in its current form to those needing a stable wire target for generating x-rays with a very small source size. The energy from the ultraviolet generation process is not yet high enough to initiate the process. Blue light was used to reach intensities on the order of 10^{16} , which was enough to produce x-rays above the copper k- α line. With some improvements to the capillary mixing process, producing the required 200 μ J, 30 fs ultraviolet pulses should be enough to reach the intensity required to generate x-rays. The development of the chirped pulse optical parametric amplification in gas-filled capillary waveguides has created the possibility of studying x-ray generation with a tabletop, Ti:sapphire based, ultrafast laser system.

APPENDIX A LASER SYSTEM ALIGNMENT

This appendix describes the alignment procedure for the laser system described in Chapter 4. This information will be most useful for someone who is maintaining this amplifier or constructing a similar system.

A.1 Daily Alignment

First, bring both the oscillator and amplifier pump lasers online. The flash-lamps on the Continuum laser require about 30-45 minutes to stabilize. Depending on the ambient temperature of the laboratory, the oscillator can take 30 minutes to begin to lase. Ideally, the oscillator should modelock with only a slight “jog” of the second prism. If the oscillator will not modelock or lase, a cavity realignment is necessary. Typically, maximizing the laser power by iteratively adjusting both the output coupler and high reflector will restore lasing and modelocking. If a more complete tune-up is required, refer to the KMLabs oscillator manual.

When the pump laser is first started, the energy can vary by as much as $\pm 20\%$. If the pump light is allowed to reach the crystal, optical damage could occur. It is best to block the beams until the power stabilizes. The pump typically returns to the previous day's power if it has enough time to warm up. Be careful about increasing the pump power without allowing enough time for the warm up, because the pump power could continue

to rise. Typically, when the pump power is applied to the crystal, the amplifier pointing and energy should be restored from the previous day. The pointing to the second set of passes can be adjusted to optimize the energy output. Small adjustments to the pump pointing can also be used to recover the output energy. A photodiode in the amplifier enclosure should show ~35-40% depletion in the fluorescence at the optimum energy output. The two irises after the amplifier define the path into the grating compressor. If the beam is not centered on the irises, align it to them using the turning mirrors after the ring.

Throughout the day check the output energy periodically. Depending on the ambient room temperature, the pump laser output can vary and should be adjusted to the proper value. Occasionally, the Pockels cell window can shift and affect the seeding of the amplifier. With some experience, this can be diagnosed with the diode inside the enclosure. To remedy this problem, put the input to the amplifier on a diode and check that a single clean pulse is seeding the amplifier.

A.2 Complete Alignment

If the amplifier output cannot be restored with small tweaks, a complete realignment may be required. First, align the first pass through the middle of the crystal, and monitor it with a high-speed photodiode. Then apply the pump beams and tune them to maximize the single pass gain. The single pass gain should be ~4.5. Much of the remaining alignment can be done with the oscillator beam. Block the pump laser, and place a half-wave plate between the crossed polarizers near the Pockels Cell. This transmits a

low energy train of pulses to the amplifier. The alignment is most easily accomplished by imaging the crystal surface to a CCD camera. Place an ~25 mm lens should be placed about 4-6" away from the Brewster cut Ti:sapphire crystal. Place the CCD camera at the image plane of the lens. The source plane should be at the crystal surface; this is best checked by placing a sheet of paper on the crystal face and looking for a sharp edge on the image.

Align the ring to overlap all eight passes with the first pass on the crystal surface. If it seems impossible to overlap the beams at the crystal, the ring mirror spacing may be wrong. Move one of the spherical mirrors in or out slightly and check the overlap. This should only be necessary if the amplifier ring was disassembled. Then without the saturable absorber, extract the beam and send it back into the ring. If necessary adjust the telescope to give a collimated beam slightly larger than the last pass in the first set. Overlap this beam with the same spots on the crystal. With an infrared viewer check the spots on the spherical mirrors. They should be directly above or below (depending on which spherical mirror) the previous set of passes. If they are not, the input to the second set is not collinear with the input to the first set. Iterate on the two mirrors between the sets to optimize this.

Remove the half-wave plate near the Pockels cell and insert the saturable absorber near the focus between the lenses, tilted slightly. Apply the pump light, and measure the output power. If more tuning is required, first maximize the energy after the first set of passes by tuning one of the ring mirrors. Then maximize the energy after the second set

by adjusting the pointing into the second set of passes. This should complete the alignment of the ring.

REFERENCES

1. D. Strickland and G. Mourou, *Compression of amplified chirped optical pulses*. Opt. Commun., 1985. **56**(3): p. 219-221.
2. J. Squier, F. Salin, G. Mourou, and D. Harter, *100-fs pulse generation and amplification in Ti:Al₂O₃*. Opt. Lett., 1991. **16**(5): p. 324-326.
3. S. Backus, C. G. Durfee, M. M. Murnane, and H. C. Kapteyn, *High power ultrafast lasers*. Rev. Sci. Instrum., 1998. **69**(3): p. 1207-1223.
4. *The Nobel Prize in Chemistry*. 1999, Royal Swedish Academy of Sciences.
5. A. H. Zewail, *Femtochemistry. Past, present and future*. Pure App. Chem., 2000. **72**(12): p. 2219-2231.
6. M. J. Rosker, M. Dantus, and A. H. Zewail, *Femtosecond real-time probing of reactions. I. The technique*. J. Chem. Phys., 1988. **89**(10).
7. M. Gruebele and A. H. Zewail, *Ultrafast reaction dynamics*. Physics Today, 1990. **43**(5): p. 24-33.
8. K. A. Nelson and A. H. Zewail, *Ultrafast Spectroscopy of Chemical and Biological Processes: Introduction*. J. Opt. Soc. Am. B, 1990. **7**(8): p. 1508.
9. F. Korte, S. Adams, A. Egbert, C. Fallnich, A. Ostendorf, S. Nolte, M. Will, J. P. Ruske, B. Chichkov, and A. Tuennermann, *Sub-diffraction limited structuring of solid targets with femtosecond laser pulses*. Opt. Exp., 2000. **7**(2): p. 41-49.
10. A. Thoss, M. Richardson, G. Korn, M. Faubel, H. Stiel, U. Vogt, and T. Elsaesser, *Kilohertz sources of hard x-rays and fast ions with femtosecond laser plasmas*. J. Opt. Soc. Am. B, 2003. **20**(2): p. 224-228.
11. T. Guo, C. Spielmann, B. C. Walker, and C. P. J. Barty, *Generation of hard x rays by ultrafast terawatt lasers*. Rev. Sci. Instrum., 2001. **72**(1): p. 41-47.
12. Y. Jiang, T. Lee, and C. G. Rose-Petrucci, *Generation of ultrashort hard-x-ray pulses with tabletop laser systems at a 2-kHz repetition rate*. J. Opt. Soc. Am. B, 2003. **20**(1): p. 229-237.

13. C. G. Durfee, S. Backus, M. M. Murnane, and H. C. Kapteyn, *Design and implementation of a TW-class kilohertz amplifier system*. IEEE J. Sel. Top. Quantum Electron., 1998. **4**(2): p. 395-406.
14. G. Cerullo and S. D. Silvestri, *Ultrafast optical parametric amplifiers*. Rev. Sci. Instrum., 2003. **74**(1): p. 1-18.
15. C. G. I. Durfee, S. Backus, M. M. Murnane, and H. C. Kapteyn, *Ultrabroadband phase-matched optical parametric generation in the ultraviolet by use of guided waves*. Opt. Lett., 1997. **22**(20): p. 1565-1567.
16. J. Ringling, O. Kittelmann, F. Noack, G. Korn, and J. Squier, *Tunable femtosecond pulses in the near vacuum ultraviolet generated by frequency conversion of amplified Ti:sapphire laser pulses*. Opt. Lett., 1993. **18**(23): p. 2035-2037.
17. S. Chelkowski and A. D. Bandrauk, *Measuring molecular wave functions using laser Coulomb explosion imaging with ultraviolet lasers*. Appl. Phys. B: Lasers Opt., 2002. **74**(9): p. s113-s120.
18. N. A. Anderson, C. G. Durfee, and R. J. Sension, *The Internal conversions of trans- and cis-1,3,5-hexatriene in cyclohexane solution studied with sub-50 fs UV pulses*. Chem. Phys. Lett., 2000. **323**(3/4): p. 365-371.
19. S. Lochbrunner, T. Schultz, M. Schmitt, J. P. Shaffer, M. Z. Zgierski, and A. Stolow, *Dynamics of excited-state proton transfer systems via time-resolved photoelectron spectroscopy*. J. Chem. Phys., 2001. **114**(6): p. 2519-2522.
20. M. Bargheer, J. Pietzner, P. Dietrich, and N. Schwentner, *Ultrafast laser control of ionic-bond formation: ClF in argon solids*. J. Chem. Phys., 2001. **115**(21): p. 9827-9834.
21. A. N. Tarnovsky, M. Wall, M. Gustafsson, N. Lascoux, V. Sundström, and E. Åkesson, *Ultrafast Study of the Photodissociation of Bromiodomethane in Acetonitrile upon 266 nm Excitation*. J. Phys. Chem. A, 2002. **106**(25): p. 5999-6005.
22. K. Beck, A. Joly, and W. Hess, *Time-resolved femtosecond laser-induced desorption from magnesium oxide and lithium fluoride single crystals*. Surf. Sci., 2000. **451**(1): p. 166-173.
23. C. A. Buehler, U. Graf, and R. A. Hochstrasser, *Multidimensional fluorescence spectroscopy using a streak camera based pulse fluorometer*. Rev. Sci. Instrum., 1998. **69**(3): p. 1512-1518.

24. S. Lejnine, C. G. Durfee, M. M. Murnane, H. C. Kapteyn, V. L. Makarov, and J. P. Langmore, *Crosslinking of proteins to DNA in human nuclei using a 60 femtosecond 266 nm laser*. *Nucleic Acids Research*, 1999. **27**(18): p. 3676-3684.
25. K. Osvay, G. Kurdi, J. Klebniczki, M. Csatari, I. N. Ross, E. J. Divall, C. J. Hooker, and A. J. Langley, *Broadband amplification of ultraviolet laser pulses*. *Appl. Phys. B: Lasers Opt.*, 2002. **74**(9): p. s163-s169.
26. K. Osvay, G. Kurdi, J. Klebniczki, and M. Csatari, *Demonstration of high gain amplification of femtosecond ultraviolet laser pulses*. *Appl. Phys. Lett.*, 2002. **80**(10): p. 1704-1706.
27. M. Marsi, M. Trovò, R. P. Walker, L. Giannessi, G. Dattoli, A. Gatto, N. Kaiser, S. Günster, D. Ristau, M. E. Couprie, D. Garzella, J. A. Clarke, and M. W. Poole, *Operation and performance of a free electron laser oscillator down to 190 nm*. *Appl. Phys. Lett.*, 2002. **80**(16): p. 2851-2853.
28. C. G. Durfee, S. Backus, H. C. Kapteyn, and M. M. Murnane, *Intense 8 fs pulse generation in the deep-ultraviolet*. *Opt. Lett.*, 1999. **24**: p. 697-699.
29. C. G. Durfee, A. Rundquist, S. Backus, Z. Chang, C. Herne, H. C. Kapteyn, and M. M. Murnane, *Guided-wave phase-matching of ultrashort-pulse light*. *J. Nonlinear Opt. Phys. Mat.*, 1999. **8**(2): p. 211-234.
30. M. M. Murnane, H. C. Kapteyn, M. D. Rosen, and R. W. Falcone, *Ultrafast x-ray pulses from laser-produced plasmas*. *Science*, 1991. **251**: p. 531-536.
31. Y. Jiang, T. Lee, W. Li, G. Ketwaroo, and C. G. Rose-Petruck, *High-average-power 2-kHz laser for generation of ultrashort x-ray pulses*. *Opt. Lett.*, 2002. **27**(11): p. 963-965.
32. M. Borghesi, A. Mackinnon, R. Gaillard, O. Willi, and D. Riley, *Absorption of subpicosecond uv laser pulses during interaction with solid targets*. *Phys. Rev. E*, 1999. **60**(6): p. 7374-7381.
33. O. E. Martinez, *Design of high-power ultrashort pulse amplifiers by expansion and recompression*. *IEEE J. Quantum Electron.*, 1987. **23**(8): p. 1385-1387.
34. I. Walmsley, L. Waxler, and C. Dorrer, *The role of dispersion in ultrafast optics*. *Rev. Sci. Instrum.*, 2001. **72**(1): p. 1-29.

35. D. N. Fittinghoff, B. C. Walker, J. A. Squier, C. S. Toth, C. Rose-Petruck, and C. P. J. Barty, *Dispersion considerations in ultrafast CPA systems*. IEEE J. Sel. Top. Quantum Electron., 1998. **4**(2): p. 430-440.
36. M. Bass, ed. *Handbook of Optics, Vol II*. 2nd ed., ed. O.S.o. America. 1994, McGraw- Hill, Inc.: New York.
37. O. E. Martinez, *3000 times grating compressor with positive group velocity dispersion: Application to fiber compensation in 1.3-1.6 μm region*. IEEE J. Quantum Electron., 1987. **23**(1): p. 59-64.
38. J. V. Rudd, G. Korn, S. Kane, J. Squier, G. Mourou, and P. Bado, *Chirped-pulse amplification of 55-fs pulses at a 1-kHz repetition rate in a Ti:Al₂O₃ regenerative amplifier*. Opt. Lett., 1993. **18**(23): p. 2044-2046.
39. J. Zhou, C. P. Huang, C. Shi, M. M. Murnane, and H. C. Kapteyn, *Generation of 21-fs millijoule-energy pulses by use of Ti:sapphire*. Opt. Lett., 1994. **19**(2): p. 126-128.
40. R. L. Fork, O. E. Martinez, and J. P. Gordon, *Negative dispersion using pairs of prisms*. Opt. Lett., 1984. **9**(5): p. 150-152.
41. M. T. Asaki, C. P. Huang, D. Garvey, J. Zhou, H. C. Kapteyn, and M. M. Murnane, *Generation of 11-fs pulses from a modelocked Ti:sapphire laser*. Opt. Lett., 1993. **18**: p. 977.
42. J. P. Zhou, C. P. Huang, M. M. Murnane, and H. C. Kapteyn, *Amplification of 26 fs, 2 TW pulses near the gain-narrowing limit in Ti:sapphire*. Opt. Lett., 1995. **20**(1): p. 64.
43. S. Backus, J. Peatross, C. P. Huang, H. C. Kapteyn, and M. M. Murnane, *Ti:Sapphire Amplifier Producing Millijoule-Level, 21 fs Pulses at 1 kHz*. Opt. Lett., 1995. **20**(19): p. 2000.
44. A. Rousse, C. Rishel, and J.-C. Gauthier, *Colloquium: Femtosecond x-ray crystallography*. Rev. Mod. Phys., 2001. **73**: p. 17-31.
45. M. Roth, T. E. Cowan, C. Brown, M. Christl, W. Fountain, S. Hatchett, J. Johnson, M. H. Key, D. M. Pennington, M. D. Perry, T. W. Phillips, and T. C. Sangster, *Intense ion beams accelerated by petawatt-class lasers*. Nuclear Instruments & Methods in Physics Research A, 2000. **464**: p. 201-205.
46. J. Wojtkiewicz and C. G. Durfee, *High-Energy, high-contrast, double-confocal multipass amplifier*. Opt. Exp., 2004. **12**(7): p. 1383-1388.

47. W. Koechner, *Solid-state laser engineering*. 1996, Heidelberg: Springer-Verlag.
48. A. Sullivan, H. Hamster, H. C. Kapteyn, S. Gordon, W. White, H. Nathel, R. J. Blair, and R. W. Falcone, *Multi-Terawatt 100 Femtosecond Laser*. *Opt. Lett.*, 1991. **16**(18): p. 1406-1408.
49. R. Trebino, K. W. DeLong, D. N. Fittinghoff, J. N. Sweetser, and D. J. Kane, *Measuring ultrashort laser pulses in the time-frequency domain using frequency-resolved optical gating*. *Rev. Sci. Instrum.*, 1997. **68**(9): p. 3277-3295.
50. C. Barty, G. Korn, F. Raksi, C. Rose-Petruck, J. Squier, A. Tian, K. Wilson, V. Yakovlev, and K. Yamakawa, *Regenerative pulse shaping and amplification of ultrabroadband optical pulses*. *Opt. Lett.*, 1996. **21**(3): p. 219-221.
51. T. F. Johnston, *Beam propagation (M^2) measurement made as easy as it gets: the four-cuts method*. *Appl. Opt.*, 1998. **37**(21): p. 4840-4850.
52. S. Backus, J. Peatross, Z. Zeek, A. Rundquist, G. Taft, M. M. Murnane, and H. C. Kapteyn, *16-fs, 1-mJ ultraviolet pulses generated by third-harmonic conversion in air*. *Opt. Lett.*, 1996. **21**(9): p. 665-667.
53. G. P. Agrawal, *Nonlinear Fiber Optics*. 1989, New York: Academic Press.
54. E. A. J. Marcatili and R. A. Schmelzter, *Hollow metallic and dielectric waveguides for long distance optical transmission and lasers*. *Bell Sys. Tech. J.*, 1964. **43**: p. 1783-1809.
55. J. R. Davies and J. T. Mendonca, *Basic physics of laser propagation in hollow waveguides*. *Phys. Rev. E*, 2000. **62**(5): p. 7168-7180.
56. A. Dubietis, G. Jonusauskas, and A. Piskarskas, *Powerful femtosecond pulse generation by chirped and stretched pulse parametric amplification in BBO crystals*. *Opt. Commun.*, 1992. **88**: p. 437-440.
57. I. N. Ross, P. Matousek, M. Towire, A. J. Langley, and J. L. Collier, *The prospects for ultrashort pulse duration and ultrahigh intensity using optical parametric chirped pulse amplification*. *Opt. Commun.*, 1997. **144**: p. 125-133.
58. C. G. Durfee, L. Misoguti, S. Backus, H. C. Kapteyn, and M. M. Murnane, *Phase matching in cascaded third-order processes*. *J. Opt. Soc. Am. B*, 2002. **19**(4): p. 822-831.

59. R. DeSalvo, D. J. Hagan, M. Sheik-Bahae, G. I. Stegeman, E. W. V. Stryland, and H. Vanherzeele, *Self-focusing and self-defocusing by cascaded second-order effects in KTP*. Opt. Lett., 1992. **17**(1): p. 28-30.
60. F. Raoult, A. C. L. Boscheron, D. Husson, C. Rouyer, C. Sauteret, and A. Migus, *Ultrashort, intense ultraviolet pulse generation by efficient frequency tripling and adapted phase matching*. Opt. Lett., 1999. **24**(5): p. 354-356.
61. F. Raoult, A. C. L. Boscheron, D. Husson, C. Sauteret, A. Modena, V. Malka, F. Dorchies, and A. Migus, *Efficient generation of narrow-bandwidth picosecond pulses by frequency doubling of femtosecond chirped pulses*. Opt. Lett., 1998. **23**(14): p. 1117-1119.
62. A. M. Streltsov, J. K. Ranka, and A. L. Gaeta, *Femtosecond ultraviolet autocorrelation measurements based on two-photon conductivity in fused silica*. Opt. Lett., 1998. **23**(10): p. 798-800.
63. P. Liu, W. L. Smith, H. Lotem, J. H. Bechtel, N. Bloembergen, and R. S. Adhav, *Absolute two-photon absorption coefficients at 355 and 266 nm*. Phys. Rev. B, 1978. **17**(12): p. 4620-4632.
64. R. Trebino, *Frequency-Resolved Optical Gating: The Measurement of Ultrashort Laser Pulses*. 1 ed. Vol. 1. 2002: Kluwer Academic Publishers. 456.
65. P. A. Lee, P. H. Citrin, P. Eisenberger, and B. M. Kincaid, *Extended x-ray absorption fine structure-its strengths and limitations as a structural tool*. Rev. Mod. Phys., 1981. **53**(4): p. 769-806.
66. F. Raksi, K. R. Wilson, Z. Jiang, A. Ikhlef, C. Y. Cote, and J.-C. Kieffer, *Ultrafast x-ray absorption probing of a chemical reaction*. J. Chem. Phys., 1996. **104**(15): p. 6066-6069.
67. F. Benesch, T. Lee, Y. Jiang, and C. G. Rose-Petruck, *Ultrafast laser-driven x-ray spectrometer for x-ray absorption spectroscopy of transition metal complexes*. Opt. Lett., 2004. **29**(9): p. 1028-1030.
68. C. Reich, P. Gibbon, I. Uschmann, and E. Forster, *Yield Optimization and Time Structure of Femtosecond Laser Plasma Ka Sources*. Phys. Rev. Lett., 2000. **84**(21): p. 4846-4849.

69. C. Rose-Petruck, R. Jimenez, T. Guo, A. Cavalleri, C. W. Siders, F. Raksi, J. A. Squier, B. C. Walker, K. R. Wilson, and C. P. J. Barty, *Picosecond-milliångstrom lattice dynamics measured by ultrafast X-ray diffraction*. *Nature*, 1999. **398**: p. 310-312.
70. C. Rose-Petruck, *Personal Communication*. 2004.